Diversity of Disk-Planet Interaction

Takayuki Muto

ABSTRACT

Disk-planet interaction is one of the main ingredients of the theory of planetary system formation, which is yet to be understood, although standard scenario of planet formation does not take into account. The timescale of planet migration, which occurs as a result of disk-planet interaction, is very likely to be shorter than disk lifetime. If planets migrate inward in a short timescale, planetary systems, including our Solar System, are not able to be formed. It is only recently that we are aware that the direction and timescale of the planet migration can be very sensitive to the disk state. Different disks can result in different planet migration, and therefore, planet migration can be a clue to understand the diversity of the currently observed extrasolar planet systems. In this thesis, in order to understand how disk state can affect the properties of disk-planet interaction, we explore the effects of magnetic field and viscosity on disk-planet migration, using mainly linear perturbation theory. Then, we also investigate how non-linear effects come into play in disk-planet interaction.

Acknowledgment

Contents

Chapter 1

Introduction

Ever since the discovery of 51 Peg b (Mayor and Quelotz 1995 [59]), more than 400 extrasolar planets have been found in our neighborhood (The Extrasolar Planets Encyclopedia [22]). One of the most surprising facts may be that the extrasolar planetary systems totally do not look like our Solar System. Some "jupiters" orbit very close to the central star. Some "eccentric" planets have very high eccentricity. We are now not very sure whether we are "typical" in our universe. Figure 1.1 shows the relationship between the mass and the semi-major axis of planets discovered, and Figure 1.2 shows the relationship between the orbital semi-major axis and the eccentricity of the planet.

Most of the planets are found by so-called "indirect" method, which does not observe the photons from the planets themselves. The most successful methods to date is the radial velocity method, which observes the wobbling motion of the central star due to the planet's orbital motion using high-resolution spectroscopy. Typically, radial velocity methods provide the information of the minimum mass of the planets, semi-major axis, and the eccentricity of the planets. Another successful indirect method is transit, which observes the eclipse of the central star by the planets. Although the number of the planets discovered by transit is small compared to the radial velocity methods since eclipse does not occur all the systems, this method provides us much more information than the radial velocity methods such as inclination, density of the planets and so forth.

"Direct" observations of the photons emitted by planets are far more challenging than the indirect methods because (1) very high spacial resolution is necessary, (2) the central star is very bright compared to the planet itself, and (3) very high sensitivity is required. It is only recently that the possible planetary-mass companions to main-sequence stars are discovered (Marois et al. 2008 [29], Kalas et al. 2008 [30], Thalmann et al. 2009 [32]). It is promising that more discoveries are to come in the near future. Figure 1.3
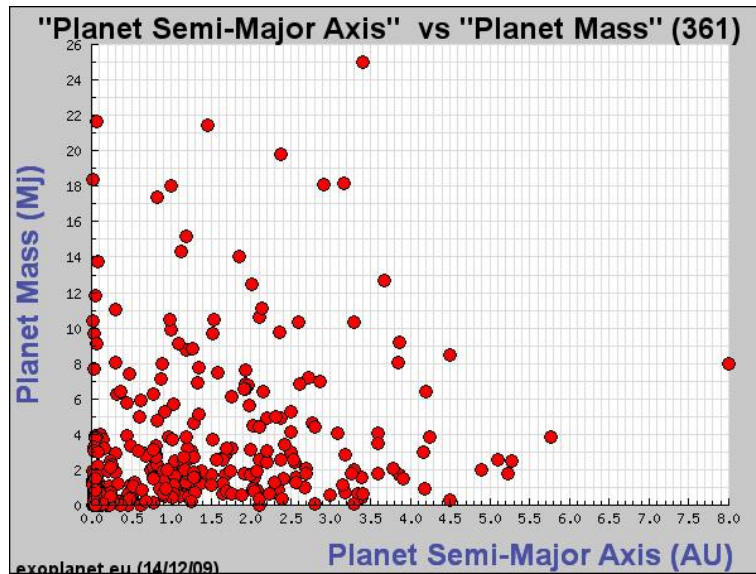
Figure 1.1: The correlation diagram between the (minimum) mass and the semi-major axis of the planets. The population with close orbit and high-mass is called "hot jupiters".
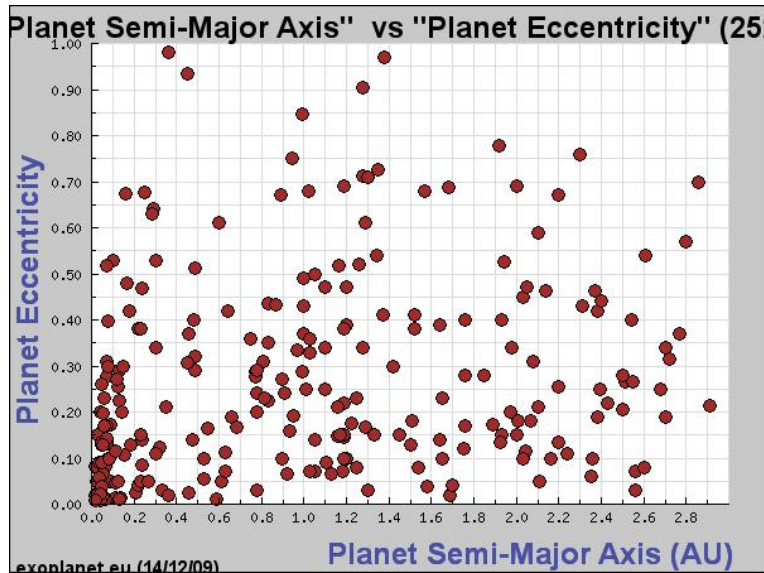

Figure 1.2: The correlation diagram between the semi-major axis and the eccentricity of the planets. The population with high-eccentricity is called "eccentric planets".
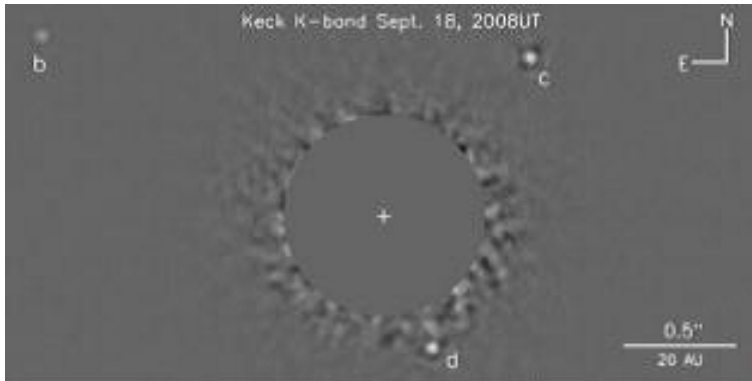
Figure 1.3: The image of three low-mass companions (denoted by b, c, and d) of A-type star HR8799. This image is taken from Marois et al. 2008 [29]

shows the image of three low-mass companions around HR8799.

Despite the great development of observational studies of extrasolar planets, theorists working on planet formation are now facing great challenges. We need to understand how such diverse planets are formed, whilst the "standard formation scenario" of *our solar system* yet contains many serious difficulties.

It is considered that the planets are formed from a protoplanetary disk that contains gas and dust particles surrounding young stars. There are two scenarios of planet formation. One is disk instability model (Cameron, 1978 [11]), and the other is core-accretion model (Hayashi et al. 1985 [44]). In the disk instability model, planets are formed through the gravitational instability of the massive protoplanetary disk. It is possible to form planets in a relatively short timescale in this model, although it is difficult to form rocky planets such as Earth. In the core-accretion scenario, dust particles coagulate each other to form massive objects. In this scenario, rocky planets are formed naturally, although it also contains some difficulties such as migration of dust and planets, or timescale problems of the coagulation of dust particles. It is considered that our solar system is formed by core accretion. Moreover, metallicity-planet correlation shown in Figure 1.4 indicates that the higher the metallicity of the central star, the more probable that the planets are found. This supports the core-accretion scenario because the circumstellar disk around a metal-rich star most likely contains larger amount of dust particles, from which planets are formed. In a gravitational instability scenario, planets are formed regardless of the stellar metallicity, since planets are assumed to be formed via gravitational instability of *gas* disk.

However, we note that gravitational instability scenario may be more
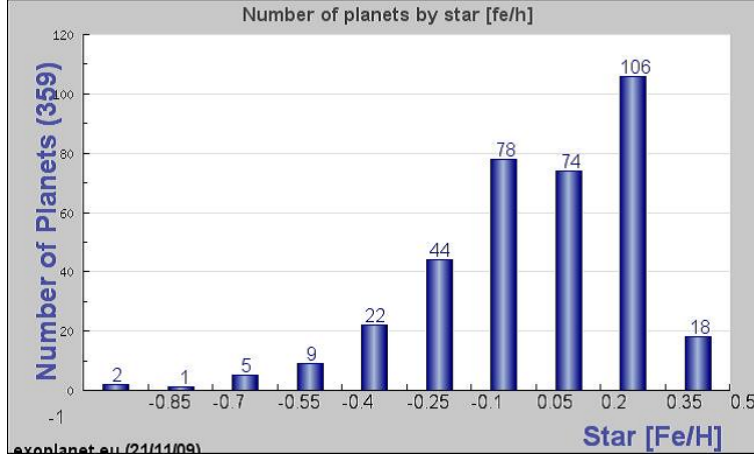
Figure 1.4: The number of planets as a function of host star metallicity. This figure is created using the data provided by The Extrasolar Planets Encyclopedia [22].

plausible in explaining recently discovered systems using direct imaging methods (Marois et al. 2008 [29], Kalas et al. 2008 [30]). These systems harbor planets far from the central star, and as shown in the subsequent chapter, planetary formation by core accretion simply takes too long time. It is not yet confirmed whether such systems are abundant. Whether (most) planetary systems are formed by core accretion or disk instability (or both) is under serious discussion.

In this thesis, we consider core-accretion scenario. One important physical process which may affect the "standard" core accretion scenario is the disk-planet interaction, which is the main focus of this thesis. Planets and disk interact through gravitational force. As a result, density wave is excited on the disk, and the backreaction from the density wave causes the change of the semi-major axis of the planets and they migrate in the disk. The timescale of the radial migration is relatively short compared to the disk dispersal timescale. Therefore, in order to construct "realistic" planet formation model, it is necessary to consider this effect, although the standard theory is based on the assumption of in-situ formation.

Probably the most serious problem on planetary migration is that the direction of the migration is not well understood. It has long been believed that the planets migrate inward (e.g., Ward 1997 [91], Tanaka et al. 2002 [83]). This result is derived using the disk models of standard core accretion scenario. However, inward migration may not be a very robust result. For example, when radiative effects are taken into account, it is possible that planets

migrate outward (Paardekooper and Mellema 2006 [67]). Such effects have not been taken into account in the standard core accretion scenario. It is now necessary to investigate how physical processes acting on the disk may affect disk-planet interaction qualitatively and quantitatively.

We first review the framework of standard core-accretion scenario in Chapter 2 and point out some theoretical problems involved in the model. We then review some classic works on disk-planet interaction and planetary migration in Chapter 3. We then consider how magnetic field exerted on the disk can alter the physics of disk-planet interaction in Chapter 4. In Chapter 5, we investigate the effects of viscosity on disk-planet interaction. Main focus on these two chapters are linear analyses of disk-planet interaction. In Chapter 6, we show results of numerical simulations on disk-planet interaction. We summarize our work in Chapter 7.

Chapter 2

Theory of Planet Formation

In this chapter, we review in detail the core accretion scenario of planetary formation. We show that core accretion scenario successfully explains some of the properties of the solar system. We also show that this scenario itself contains many theoretical difficulties.

2.1   Minimum Mass Solar Nebula

The very first step of the theory of planet formation is to provide its initial condition. In principle, the properties of protoplanetary disk are determined as a consequence of star formation. However, it is not possible to follow the collapse of the molecular cloud ($\sim$ 1pc scale) all the way down to proto-planetary disk resolving central star ($\sim 10^5$km scale). The highest resolution numerical study at present is done using nested-grid technique (e.g., Machida et al. 2005 [28]) and it is possible to resolve $\sim$ 10AU scale (first core) while the simulation box is approximately 10pc scale. It is yet required to resolve another five orders of magnitude in order to determine the initial condition of planetary system formation.

It is, however, natural to consider that the protostar is accompanied by protostellar disk. Theoretically, if the initial molecular cloud is rotating, it is a natural consequence of the conservation of angular momentum that disk is formed around the star. Observationally, the existence of disk is indicated by the infrared excess of spectral energy distribution (e.g., Lada 1987 [50]), and more recently, it is possible to image the disk-like structure around a star (e.g., Fukagawa et al. 2004 [25], Fujiwara et al. 2006 [24]).

In the original model of core accretion scenario, it is assumed that there is a protoplanetary disk associated with a protostar, and the disk property is reconstructed using the distribution of solid materials of Solar System

(e.g., Kusaka et al. 1970 [49], Hayashi et al. 1981 [43]). This disk is called Minimum Mass Solar Nebula (MMSN), because it contains the minimum amount of solid particles to make the solar system. The surface density of solid particles Σ_d in MMSN model is given by

$$\Sigma_d = \begin{cases} 7.1 \times \left(\frac{r}{1\text{AU}}\right)^{-\frac{3}{2}} \text{ g cm}^{-2} & 0.35\text{AU} < r < 2.7\text{AU} \\ 30 \times \left(\frac{r}{1\text{AU}}\right)^{-\frac{3}{2}} \text{ g cm}^{-2} & 2.7\text{AU} < r < 36\text{AU} \end{cases} \tag{2.1}$$

The jump of Σ_d at $r = 2.7$AU comes from the speculation that beyond this radius, the temperature of the disk is below the condensation temperature of ice, and the ice is added to the solid particle component. This line is called "snow line". The surface density of gas, Σ_g, is given by multiplying gas-dust ratio to Σ_d,

$$\Sigma_g = 1.7 \times 10^3 \left(\frac{r}{1\text{AU}}\right)^{-\frac{3}{2}} \text{ g cm}^{-3}. \tag{2.2}$$

We note that MMSN model is constructed using the distribution of solid materials in Solar System, recent observations of protoplanetary disks indicate that the mass of extrasolar planetary disks are close to that of MMSN model [3]. It is a coincidence, but it is possible to use the MMSN model as a reference model in considering the formation of extrasolar systems. However, different models of protoplanetary disks are also discussed (e.g., Desch 2007 [21]).

The temperature of the disk is given by assuming thermal equilibrium. The dust particles are heated by the irradiation from the central star, and cool by thermal radiation. Assuming the temperature of gas and dust are identical, we have

$$T = 2.8 \times 10^2 \left(\frac{r}{1\text{AU}}\right)^{-\frac{1}{2}} \left(\frac{L}{L_\odot}\right)^{\frac{1}{4}} \text{ K}. \tag{2.3}$$

Snow line is determined from this equation from the condition $T = 170$K. From this temperature distribution, the isothermal sound speed is given by

$$c = \left(\frac{kT}{\mu m_H}\right)^{\frac{1}{2}} = 9.9 \times 10^4 \left(\frac{2.34}{\mu}\right)^{\frac{1}{2}} \left(\frac{r}{1\text{AU}}\right)^{-\frac{1}{4}} \left(\frac{L}{L_\odot}\right)^{\frac{1}{8}} \text{ cm s}^{-1}. \tag{2.4}$$

In the original MMSN model, temperature distribution of the disk relies on the assumptions of optically thin disk. However, since protoplanetary disk's density is very thick, more careful treatment of the radiation transfer may be necessary. Chiang and Goldreich (1997) [15] proposed the model that takes into account two-dimensional radiation transfer. The location of snow line is sensitive to the temperature structure of the disk.

2.2 Structure of Minimum Mass Solar Nebula

In this section, we investigate the structure of the "classical" protoplanetary disk. In the original model of a protoplanetary disk, the assumptions are the following:

- Molecular viscosity is neglected

- The flow is laminar

- Magnetic field does not affect the dynamics

- Cooling timescale is shorter than the disk evolution timescale

- The disk is geometrically thin

- The mean flow of the disk is axisymmetric and azimuthal

- The physical quantities vary slowly in the radial direction compared to the vertical direction

We first present the dynamical structure of the disk, and then investigate to what extent these assumptions are valid.

2.2.1 Dynamical Structure of the Protoplanetary Disk

We first calculate the mean flow of the disk. The equations that govern the dynamics of the gas are fluid equations:

$$\frac{\partial \rho_g}{\partial t} + \nabla \cdot (\rho_g \mathbf{v}) = 0, \tag{2.5}$$

$$\rho \frac{d\mathbf{v}}{dt} = -\nabla p - \rho_g \nabla \Psi, \tag{2.6}$$

where d/dt denotes the Lagrangian time derivative, ρ_g is the gas density, $\mathbf{v}$ is the flow velocity. We denote the potential of the central star by Ψ, which is

$$\Psi = \frac{GM_*}{\sqrt{r^2 + z^2}} \tag{2.7}$$

in the cylindrical coordinate (r, ϕ, z).

We derive the stationary solution $\partial/\partial t = 0$ of the fluid equations. Neglecting higher order terms in z/r, radial component of Equation (2.6) is

$$\Omega(r)^2 = \frac{c^2}{r^2} \frac{d\ln p}{d\ln r} + \frac{GM_*}{r^3}, \tag{2.8}$$

where $\Omega(r)$ denotes the angular velocity,

$$v_\phi = r\Omega, \tag{2.9}$$

and c denotes the sound speed. We note that the gas flow velocity is slightly deviated from Keplerian rotation $\Omega_K^2 = GM_*/r^3$ because of the gas pressure effect. In MMSN, the gas pressure gradient is assumed to be negative and therefore the gas rotates at sub-Keplerian velocity.

The vertical component of the equation of motion is

$$\frac{c^2}{p}\frac{\partial p}{\partial z} = -\frac{GM_*}{r^2}\frac{z}{r}. \tag{2.10}$$

If we assume that the sound speed is constant in the vertical direction, we have

$$p(z) = \frac{c^2}{\sqrt{2\pi}}\frac{\Sigma_g}{H}e^{-\frac{1}{2}\frac{z^2}{H^2}}, \tag{2.11}$$

where Σ_g is the surface density defined by

$$\Sigma_g = \int_{-\infty}^{+\infty} dz\rho(r,z) \tag{2.12}$$

and we have defined vertical scale height H by

$$H = \frac{c}{\Omega_K}. \tag{2.13}$$

For MMSN, disk scale height is

$$H = 5.0 \times 10^{11} \left(\frac{2.34}{\mu}\right)^{\frac{1}{2}} \left(\frac{M_*}{M_\odot}\right)^{\frac{1}{2}} \left(\frac{r}{1\mathrm{AU}}\right)^{\frac{5}{4}} \mathrm{cm}. \tag{2.14}$$

It is clear that the disk scale height is much smaller than the disk's radial extent, $1\mathrm{AU} = 1.5 \times 10^{13}\mathrm{cm}$.

We note that the difference of the gas rotational velocity with respect to the Keplerian velocity is the order of the square of the disk aspect ratio H/r. We write the angular velocity of the gas by

$$\Omega \simeq \Omega_K(1-\eta), \tag{2.15}$$

where

$$\eta = -\frac{1}{2}\frac{H^2}{r^2}\frac{d\ln p}{d\ln r}. \tag{2.16}$$

2.2.2   Effects of Viscosity

We first investigate how viscosity affects the structure of the disk. We show that the molecular viscosity is safely neglected. The gas density at the equatorial plane of the disk is

$$\rho_g \sim \frac{\Sigma_g}{H} \sim 3 \times 10^{-9} \text{gcm}^{-3}. \tag{2.17}$$

Assuming that the collisional cross section between gas particles (Hydrogen molecules are the dominant component) is $\sigma \sim 10^{-20} \text{cm}^2$, mean free path of gas particles is l_{mfp}

$$l_{mfp} \sim 1 \text{cm} \tag{2.18}$$

and the mean free time τ at $T \sim 300 \text{K}$ is

$$\tau \sim 10^{-5} \text{sec}. \tag{2.19}$$

Therefore, the order of magnitude of kinetic viscosity ν arising from molecular viscosity is

$$\nu \sim \frac{l_{mfp}^2}{\tau} \sim 10^5 \text{cm}^2 \text{ s}^{-1}. \tag{2.20}$$

The characteristic scale of the flow may be $L \sim 1 \text{AU}$ and the velocity may be Kepler velocity $V \sim r\Omega$. Therefore, Reynolds number Re of the flow is estimated to be

$$Re = \frac{LV}{\nu} \sim 10^{14}. \tag{2.21}$$

Such high Reynolds number shows that the molecular viscosity can be neglected.

However, it is possible that the disk turbulence may act as an effective viscosity (Shakura and Sunyaev 1973 [79], Balbus and Papaloizou 1999 [8]). Turbulent viscosity is usually parameterized by α,

$$\nu = \alpha c H. \tag{2.22}$$

It is indicated that disk turbulence can be of the order of $\alpha \lesssim 10^{-1}$ as a consequence of magneto-rotational instability (MRI, Balbus and Hawley 1991 [6], Sano et al. 2004 [74]). Magnetic effects can be very important in considering the evolution of protoplanetary disks and we shall come back to this in Section 2.2.4. Although it is very difficult to measure the values of α, it is indicated that the turbulence with $\alpha \sim 10^{-2}$ on scales $r \sim 10 - 100 \text{AU}$ may exist (Hartmann et al. 1998 [42]).

If viscosity is exerted on a disk, the mass accretion onto the central star occurs. The radial velocity v_r is estimated by

$$v_r \sim \frac{\nu}{r} = \alpha \frac{H^2}{r^2} r\Omega, \tag{2.23}$$

and therefore mass accretion timescale is

$$t_{\mathrm{acc}} = \frac{r}{v_r} \sim 2.6 \times 10^5 \left(\frac{\alpha}{10^{-2}} \right)^{-1} \left(\frac{H/r}{0.1} \right)^{-2} \left(\frac{r}{30\mathrm{AU}} \right)^{3/2} [\mathrm{yr}]. \tag{2.24}$$

It is noted that the lifetime of the protoplanetary disks is of the order of 10^6yr (e.g., Haisch et al. 2001 [41]). If the dissipation of the disk occurs by accretion onto the central star, the values of α may be 10^{-3} or less. The strength of turbulence in a protoplanetary disks is very uncertain observationally.

2.2.3 Thermal Structure of Protoplanetary Disks

In protoplanetary disks, it is assumed that thermal timescale is shorter than disk evolution timescale so the disk is in thermally stationary state in considering the long-term evolution. The most important cooling process in a protoplanetary disk is the dust thermal radiation. Rosseland mean opacity κ of dust grains is of the order of $\kappa \sim 1\mathrm{cm}^2\mathrm{g}^{-1}$ (Pollack et al. 1985 [72]). If the disk is optically thin in vertical direction, the thermal radiation from dust particles radiates away from disk surface. [1] Thermal energy flux in the z-direction is estimated to be

$$F = -\frac{16\sigma_{SB}T^3}{3\kappa\rho} \frac{\partial T}{\partial z} \sim \frac{\sigma_{SB}T^4}{\kappa\Sigma}, \tag{2.25}$$

where σ_{SB} is the Stefan-Boltzmann constant. Thermal energy per unit area may be estimated by

$$E \sim \frac{\Sigma k_B T}{\mu m_H}. \tag{2.26}$$

Therefore, cooling timescale is

$$t_{cool} \sim \frac{E}{F} \sim 10^3 \left(\frac{\Sigma}{10^3 \mathrm{gcm}^{-2}} \right)^2 \left(\frac{\kappa}{1\mathrm{cm}^2\mathrm{g}^{-1}} \right) \left(\frac{T}{300\mathrm{K}} \right)^{-3} \mathrm{yr}. \tag{2.27}$$

We have shown that the timescale of the global evolution of the disk is of the order of 10^{5-6} years, which is longer than cooling timescale.

---

[1]Disk midplane is actually optically thick and therefore, thermal structure of the disk should be analyzed more carefully. However, since the density rapidly decreases as a function of height, the disk becomes optically thin somewhere around the disk scale height.

2.2.4   Effects of Magnetic Field

The most important role of magnetic field is that, as pointed out in Section 2.2.2, it can cause the angular momentum transport as a result of magneto-rotational instability (MRI, Balbus and Hawley 1991 [6]). We first derive the critical value of ionization degree at which the disk gas can couple with magnetic field. For flow with characteristic scale L and characteristic velocity V, if magnetic Reynolds number,

$$Re_M = \frac{LV}{\eta}, \tag{2.28}$$

exceeds unity, the flow couples with magnetic field well. Here, η denotes resistivity. Since magneto-rotational instability drives a turbulence with scale H as a result of the growth of slow wave (or Alfvén wave), the characterestic velocity may be of the order of Alfvén velocity v_A and the characteristic scale may be of the order of the scale height H. Therefore, magnetorotational instability may be suppressed if

$$Re_M = \frac{Hv_A}{\eta} \ll 1. \tag{2.29}$$

This result is more quantitatively shown by linear perturbation analysis including Ohmic dissipation (Sano and Miyama 1999 [75]).

If electrons are the main career of the electric current, the resistivity η may be determined by the collision between electrons and neutral molecular Hydrogen and is given by (Hayashi 1981 [43])

$$\eta = 6.5 \times 10^3 x^{-1} \text{cm}^2 \text{s}^{-1}, \tag{2.30}$$

where x is the ionization degree. Therefore, magnetic Reynolds number is estimated as

$$Re_M = 7.6 \times 10^{12} x \frac{1}{\beta^{\frac{1}{2}}} \left(\frac{2.34}{\mu} \right) \left(\frac{M_*}{M_\odot} \right)^{\frac{1}{2}} \left(\frac{r}{1\text{AU}} \right), \tag{2.31}$$

where $\beta = c^2/v_A^2$ is the plasma β parameter. Therefore, if ionization degree exceeds 10^{-13}, the effects of magnetic field cannot be neglected.

Ionization degree is determined by assuming ionazation equilibrium. Quantitative analyses are found in Umebayashi (1983) [88] or Sano et al. (2001) [76] and that the useful analytic formula for ionization degree is recently derived by Okuzumi(2009) [66].

Ionization occurs by collisions between molecules, cosmic rays, or decay of radioactive nuclei. Collisional ionization is important if disk temperature

exceeds 10^3K when ionization of pottasium occurs, and the ionization degree may reach 10^{-11}. Therefore, at the inner part of the disk, collisional ionization is important. At the locations distant away from the central star, cosmic ray ionization is the dominant process of ionization. However, cosmic ray can penetrate the gas with surface density of the order of ~ 100g/cm^2 (Umebayashi and Nakano 1981 [89]). At the midplane of the protoplanetary disk at $r \lesssim 1$AU, decay of radioactive nuclei is the only process of ionization. Typical values of ionization rate by radioactive nuclei is $\sim 10^{-23}$s^{-1}, which is six orders of magnitude smaller than typical interstellar cosmic ray ionization rate, $\sim 10^{-17}$s^{-1}.

The most important recombination process in a protoplanetary disk is the recombination on dust particles. This greatly reduces the number of ionized gas particles and keeps the ionization degree of the protoplanetary disk low. If dust-free disk is considered, recombination occurs in gas phase by dissociative recombination. Equating the cosmic ray ionization and dissociative recombination, we obtain the upper limit of ionization degree in protoplanetary disks,

$$x = 1.6 \times 10^{-12} \left(\frac{T}{500\text{K}} \right)^{\frac{1}{4}} \left(\frac{\zeta}{10^{-17}\text{s}^{-1}} \right)^{\frac{1}{2}} \left(\frac{n_H}{10^{13}\text{cm}^{-3}} \right)^{-\frac{1}{2}}. \qquad (2.32)$$

Therefore, it is actually possible that protoplanetary disks can couple well with magnetic field if small dust particles are depleted probably by the formation of plants. It is also noted that surfaces of the protoplanetary disks can couple with magnetic field, since cosmic rays can ionize gas particles effectively.

Following the qualitative estimate of ionization degree in protoplanetary disks, Gammie (1996) [35] proposed two-layered accretion disk model for protoplanetary disks (Figure 2.1). He proposed that the disk is magnetically active at the surfaces and at inner radii, although it is magnetically "dead" at the midplane. The region where the disk does not couple with magnetic field is called "dead zone".

It is not yet confirmed whether dead zone actually exists. Analyses including stellar X-rays (Glassgold et al. (1997) [36]) support the layered accretion model, while Inutsuka and Sano (2005) [45] suggested that dead zone may vanish if three percent of turbulent energy is used to reionize the gas. The disk model including realistic ionization state is yet to be constructed. Fromang et al. (2002) [33] used α-model to construct such models and more recently, Terquem (2008) [87] suggested a composite disk model.

In the subsequent Sections, we review the "standard" scenario of core accretion model without including magnetic or turbulent effects and discuss the problems in the models.
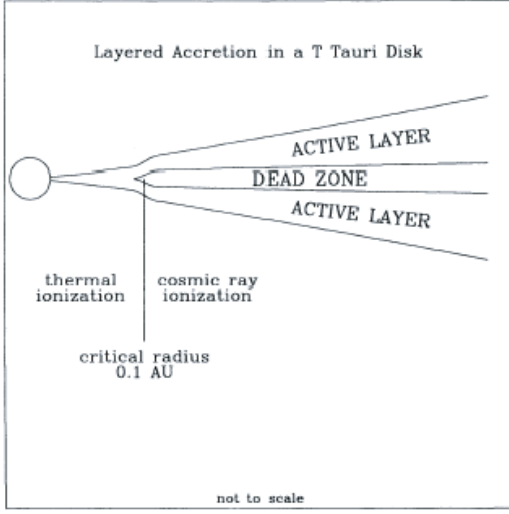
Figure 2.1: The ionization structure proposed by Gammie (1996) [35]. This figure is taken from Figure 1 of Gammie (1996).

2.3   Planetesimal Formation

In this section, we briefly review how dust particles ($\sim \mu$m in size) coagulate each other to form planetesimals ($\sim$ km size bodies).

There are two possible ways to form planetesimals. One is the mutual sticking between dust particles. The other is gravitational instability of gas disk. In MMSN model, Toomre's Q-parameter is

$$
\begin{aligned}
Q \;&=\; \frac{\kappa c}{\pi G \Sigma} \\
&\sim\; 56 \left(\frac{2.34}{\mu}\right)^{\frac{1}{2}} \left(\frac{r}{1\mathrm{AU}}\right)^{-\frac{1}{4}}
\end{aligned}
\tag{2.33}
$$

Therefore, it is more likely that mutual coagulation of dust particles plays important roles in the first stages of the growth of dust particles.

2.3.1   Gas Drag on Dust Particles

A protoplanetary disk contains gas and dust particles, and the dynamics of dust particles is important since planets are made from them. In considering the dynamics of dust particles in protoplanetary disks, it is important to consider the effects of gas, which exerts the drag force onto the dust particles.

Drag force exerted on dust particles depends on dust size. If dust size is smaller than the mean free path of gas, the drag force may be estimated

using kinetic argument. Let the velocity of dust particles v. The velocity dispersion of gas particles may be of the order of the sound velocity c. Let us consider the dust motion relative to the gas is small compared to the sound speed of the gas, $c \gg v$. For head-on collisions between gas and dust particles, momentum transfer is $\sim m_g(c + v)$, and the collision frequency is $\sim (\rho_g/m_g)D^2(c + v)$, where ρ_g, m_g, and D are gas density, mass of gas particle, and size of dust particle, respectively. Rear-on collision may be estimated in the same way. Therefore, the friction force, F_E, exerted on dust particles is

$$F_E \sim -\rho_g D^2 v_{th} v \qquad (2.34)$$

Thorough analyses are given by Epstein (1924) [23], and this drag law is called Epstein law.

If the size of dust particles exceeds the mean free path of gas, drag force may be estimated using fluid dynamics argument (Landau and Lifschitz 1959 [51]). The drag force exerted on dust particles is given by

$$F_S = 6\pi D \eta v, \qquad (2.35)$$

where η denotes the viscosity. This drag law is called Stokes law. It is to be noted that the order of magnitude of Stokes drag and Epstein drag are the same for particles with size comparable to the mean free path of gas.

The drag force is usually written, using parameter A, as

$$\mathbf{F} = -MA\rho_g\Delta\mathbf{v}, \qquad (2.36)$$

where $\Delta\mathbf{v}$ is the relative velocity between gas and dust. The value

$$t_{\mathrm{stop}} = \frac{1}{A\rho_g} \qquad (2.37)$$

is called stopping time. This is the timescale which dust particle's velocity becomes the same as the gas velocity. Stoping time relative to Kepler time for several gas densities is shown in Figure 2.2.

2.3.2   Dust Motion in Protoplanetary Disks

We now investigate the dust motion in a protoplanetary disk. For brevity, we treat the dust component as pressureless fluid and consider two-fluid model.

We write gas and dust velocity relative to Kepler motion by $\mathbf{v}_g$ and $\mathbf{v}_d$, and Keplerian angular velocity and velocity are denoted by Ω_K and v_K.

Equations of motion of gas is

$$\frac{\partial v_{g,r}}{\partial t} + v_{g,r}\frac{\partial v_{g,r}}{\partial r} + v_{g,z}\frac{\partial v_{g,r}}{\partial z} - \frac{v_{g,\phi}^2}{r} = -\rho_d A(v_{g,r} - v_{d,r}) + 2\Omega_K v_{g,\phi} + 2\eta\Omega_K v_K,$$
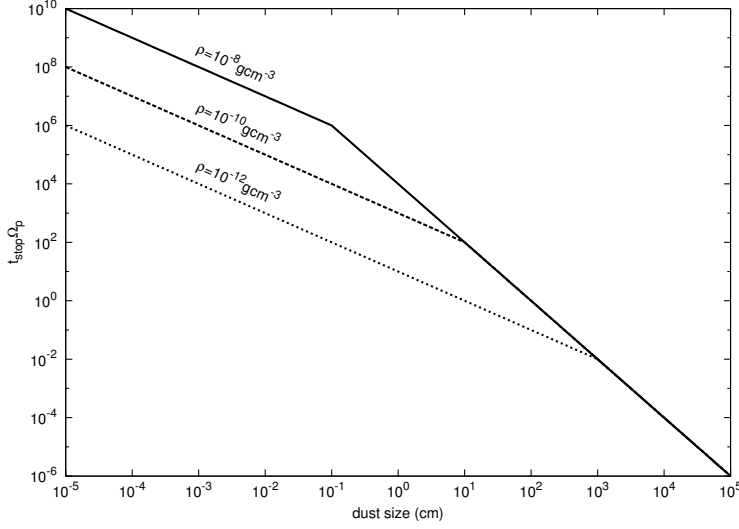$$(2.38)$$

Figure 2.2: Stopping time normalized by Kepler time for gas density with 10^{-8}gcm^{-3}, 10^{-10}gcm^{-3}, and 10^{-12}gcm^{-3}. Order of magnitude estimate used in Muto and Inutsuka (2009) [63] is plotted (Equation (6) of their paper).

$$\frac{\partial v_{g,\phi}}{\partial t} + v_{g,r}\frac{\partial v_{g,\phi}}{\partial r} + v_{g,z}\frac{\partial v_{g,\phi}}{\partial z} + \frac{v_{g,r}v_{g,\phi}}{r} = -\rho_d A(v_{g,\phi} - v_{d,\phi}) - \frac{1}{2}\Omega_K v_{g,r}, \quad (2.39)$$

$$\frac{\partial v_{g,z}}{\partial t} + v_{g,r}\frac{\partial v_{g,z}}{\partial r} + v_{g,z}\frac{\partial v_{g,z}}{\partial z} = -\rho_d A(v_{g,z} - v_{d,z}) - \Omega_K^2 z - \frac{1}{\rho_g}\frac{\partial p}{\partial z}, \quad (2.40)$$

where η is the parameter of radial pressure gradient introduced in Equation (2.15).

Equations of dust component is given by

$$\frac{\partial v_{d,r}}{\partial t} + v_{d,r}\frac{\partial v_{d,r}}{\partial r} + v_{d,z}\frac{\partial v_{d,r}}{\partial z} - \frac{v_{d,\phi}^2}{r} = -\rho_g A(v_{d,r} - v_{g,r}) + 2\Omega_K v_{d,\phi}, \quad (2.41)$$

$$\frac{\partial v_{d,\phi}}{\partial t} + v_{d,r}\frac{\partial v_{d,\phi}}{\partial r} + v_{d,z}\frac{\partial v_{d,\phi}}{\partial z} + \frac{v_{d,r}v_{d,\phi}}{r} = -\rho_g A(v_{d,\phi} - v_{g,\phi}) - \frac{1}{2}\Omega_K v_{g,r}, \quad (2.42)$$

$$\frac{\partial v_{d,z}}{\partial t} + v_{d,r}\frac{\partial v_{d,z}}{\partial r} + v_{d,z}\frac{\partial v_{d,z}}{\partial z} = -\rho_g A(v_{d,z} - v_{g,z}) - \Omega_K^2 z. \quad (2.43)$$

We consider stationary state $\partial/\partial t = 0$. We also assume that the deviation from Kepler velosity is small, $v_K \gg v_g, v_d$. At the lowest order, equations of motion become

$$0 = -\rho_d A(v_{g,r} - v_{d,r}) + 2\Omega_K v_{g,\phi} + 2\eta\Omega_K v_K, \quad (2.44)$$

$$0 = -\rho_d A(v_{g,\phi} - v_{d,\phi}) - \frac{1}{2}\Omega_K v_{g,r}, \quad (2.45)$$

$$0 = -\rho_d A(v_{g,z} - v_{d,z}) - \Omega_K^2 z - \frac{1}{\rho_g}\frac{\partial p}{\partial z}, \tag{2.46}$$

$$0 = -\rho_g A(v_{d,r} - v_{g,r}) + 2\Omega_K v_{d,\phi} + 2\eta\Omega_K v_K, \tag{2.47}$$

$$0 = -\rho_g A(v_{d,\phi} - v_{g,\phi}) - \frac{1}{2}\Omega_K v_{d,r}, \tag{2.48}$$

$$0 = -\rho_g A(v_{d,z} - v_{g,z}) - \Omega_K^2 z. \tag{2.49}$$

Therefore, radial and vertical velocity of dust particles are

$$v_{d,r} = -\frac{\Gamma}{1 + (\xi + 1)^2\Gamma^2} 2\eta v_K, \tag{2.50}$$

$$v_{g,z} - v_{d,z} = \frac{1}{\Gamma}\frac{z}{r} v_K, \tag{2.51}$$

where Γ denotes the ratio between Kepler time and stopping time

$$\Gamma = \frac{\rho_g A}{\Omega_K}, \tag{2.52}$$

and ξ is dust-to-gas ratio,

$$\xi = \frac{\rho_d}{\rho_g}. \tag{2.53}$$

Equation (2.50) shows that dust particles gradually fall onto the central star. This is because rotation velocity of gas is slightly slower than dust velocity owing to pressure gradient effect, and thereby dust particles feel negative torque due to gas drag.

2.3.3   Dust Growth and Infall

In the previous section, we have seen that dust particles fall onto the central star due to gas drag. We now question whether dust particles can grow before they fall onto the central star. In order to answer this question, it is necessary to estimate the timescale of dust growth.

The dust particles grow by mutual sticking. The growth of dust particles may be modeled by the following equation,

$$\frac{dM}{dt} = f_s \rho_d \pi D^2 \Delta v, \tag{2.54}$$

where M is the dust mass, f_s is the probability of sticking between dust particles, ρ_d is dust density, D is dust size, and Δv is the relative velocity of dust particles.

There are several ways to estimate the relative velocity. Small dust particles tend to move at the velocity of gas, while larger dust particles decouple from gas motion. Therefore, if we consider the collision between dust particles with different size, Δv may be estimated by the relative velocity between gas and the dust that does not couple with gas. If the disk is in turbulent state, relative velocity may be estimated by the root mean square of turbulent velocity. If the disk flow is laminar, the relative velocity may be estimated by sedimentation velocity of dust particles, equation (2.51). (We consider the model where dust particles grow as they sediment towards the disk midplane.)

If sedimentation velocity is used to estimate the relative velocity, the growth timescale of dust particles is

$$t_{grow} \sim \frac{\Sigma_f q}{f_s \rho_d} \frac{r}{H} \frac{1}{v_K}, \tag{2.55}$$

where q is defined by

$$\Gamma = \frac{\Sigma_g}{\rho_{mat} D} q, \tag{2.56}$$

and the order of magnitude of q is

$$q \sim \begin{cases} 1 & \text{Epstein} \\ \frac{l_{mfp}}{D} & \text{Stokes.} \end{cases} \tag{2.57}$$

In order for the dust to grow, t_{grow} must be smaller than infall time t_{infall}. From Equation (2.50), dust infall time is estimated as

$$t_{infall} \sim \frac{r}{v_{d,r}} \sim \frac{1 + \Gamma^2}{\Gamma} \frac{1}{\eta} \frac{r}{v_K}. \tag{2.58}$$

Therefore,

$$\frac{t_{infall}}{t_{grow}} \sim 1 \times \frac{1 + \Gamma^2}{\Gamma} \left(\frac{f_s}{0.1} \right) \left(\frac{\xi}{10^{-2}} \right) \left(\frac{\eta}{10^{-3}} \right)^{-1} \left(\frac{q}{1} \right)^{-1}. \tag{2.59}$$

This indicates that if $\Gamma \sim 1$, dust infall timescale is comparable to growth timescale. If $\Gamma \gg 1$, dust and gas couple well and dust particles' velocity is the same as gas velocity, preventing the infall, while if $\Gamma \ll 1$, dust particles do not feel drag force, and they do not fall onto the central star either.

For $\Gamma \sim 1$, dust size is given by

$$D \sim 10^3 \left(\frac{\Sigma_g}{10^3 \text{g cm}^{-2}} \right) \left(\frac{\rho_{mat}}{1 \text{g cm}^{-3}} \right)^{-1} \left(\frac{q}{1} \right) \text{cm.} \tag{2.60}$$

Therefore, it is now concluded that dust particles fall onto the central star if they grow to meter-size. More detailed analyses (Weidenschilling 1977 [92], Adachi et al. 1976 [2]) also support this order-of-magnitude estimate. This problem in core accretion scenario is usually referred as "meter-size barrier".

2.3.4 Planetesimal Formation by Gravitational Instability of Dust Layer

We have seen that simple dust coagulation suffers meter-size barrier. One possibility to overcome this dissiculty is the gravitational instability of dust layer. Since timescale of gravitational instability is the order of Kepler timescale, it may be possible to form planetesimals before dust particles fall onto the central star.

We have already seen that the minimum mass solar nebula is stable against gravitational collapse. However, as seen in equation (2.51), dust particles sediment towards the disk midplane, and therefore, it may be possible to form a thin dust layer, which is unstable against self-gravity. Let the velocity dispersion of dust particles v_s. The thickness of dust layer H_d is given by $H_d \sim v_s/\Omega$. Therefore, in order for the gravitational instability to occur, the thickness must be

$$H_d < \frac{\pi G \Sigma_g}{\Omega^2} \sim 3.7 \times 10^7 \left(\frac{\Sigma_g}{7.1 \text{g cm}^{-2}}\right) \left(\frac{\Omega}{2\pi/1\text{yr}}\right)^{-2} \text{ cm.} \qquad (2.61)$$

This scale is 10^{-3} times smaller than gas scale height.

We investigate to what size dust particles grow if gravitational instability occurs. The most unstable wave number of gravitational instability is

$$k \sim \frac{G \Sigma_d}{v_s^2} \sim \frac{G \Sigma_d}{H_d^2 \Omega^2}. \qquad (2.62)$$

When Toomre's Q-parameter is the order of unity, $k \sim 1/H_d$. If dust layer fragments to this size, the mass of planetesimal formed by gravitational instability is estimated as

$$m \sim \Sigma_d H^2 \sim 10^{16} \left(\frac{\Sigma_d}{7.1 \text{g cm}^{-2}}\right) \left(\frac{H}{3.7 \times 10^7 \text{cm}}\right) \text{ g.} \qquad (2.63)$$

Since the characteristic density of dust grain is 1gcm^{-3}, the size of this boulder is of the order of $\sim$ km size, which is large enough to overcome the meter-size barrier.

2.3.5 Instability of Thin Dust Layer

We have seen that gravitational instability may be one of the possible way to overcome the meter-size barrier. However, this model itself suffers another difficulty. The key physics is again the difference in velocity of dust particles and gas. Dust particles tend to rotate at Kepler velocity, while gas rotation velocity is slightly sub-Kepler because of pressure gradient effects.

As dust particles sediment towards the midplane to form a dust layer, velocity shear develops between the dust layer and gas. This shear causes Kelvin-Helmholtz instability. The condition for Kelvin-Helmholtz instability is given by Richardson number (Chandrasekhar 1981 [14]), which is defined by

$$J = -\frac{g}{\rho} \frac{\frac{\partial \rho}{\partial z}}{\left(\frac{\delta v}{\delta z}\right)^2},$$
(2.64)

where g is the gravitational acceleration. The stability condition is

$$J < \frac{1}{4}.$$
(2.65)

This condition may be derived by considering energy release when fluid elements in gas and dust layer is exchanged.

When dust layer becomes so thin that it is prone to gravitational instability, the thickness of dust layer is $\delta z \sim 10^7$cm and the dust density is $\rho_d \sim \Sigma_d/\delta z \sim 10^{-6}$gcm^{-3}. The density of gas is $\rho_g \sim 10^{-9}$g cm^{-3} so $\rho_g \ll \rho_d$. Therefore, in the definition of Richardson number, $\delta \rho \sim \delta \rho_d$. The relative velocity is $\delta v \sim \eta v_K$ and the gravitational acceleration may be estimated as $g \sim \delta z \Omega_K^2$. Therefore, Richardson number of dust-layer and gas system is

$$J \sim \frac{\delta z^2}{\delta v^2} \Omega_K^2 \sim \left(\frac{\delta z}{r} \frac{1}{\eta}\right)^2 \sim 10^{-8} \left(\frac{\delta z/r}{10^{-7}} \frac{10^{-3}}{\eta}\right)^2,$$
(2.66)

which is much smaller than 1/4. This indicates that the dust layer becomes unstable before the onset of gravitational instability, and the thickness of dust layer cannot be thin enough to become gravitationally unstable. Sekiya (1998) [78] modeled the fully saturated state of Kelvin-Helmholtz instability by calculating the quasi-stationary state with $J = 1/4$, and obtained that the dust layer is gravitationally stable.

2.3.6 Possible Scenario of Planetesimal Formation

We have seen that planetesimal formation by gravitational instability of dust layer suffers another difficulty. There have been many scenarios suggested for

planetesimal formation. For example, disk turbulence induced by magneto-rotational instability and streaming instability can concentrate meter-size dust effectively to cause the gravitational instability of dust particles (Johansen et al. 2007 [26]). Anti-cyclonic vorticies may be a preferred site of planetesimal formation (Klahr and Bodenheimer 2006 [46]). If there is a giant planet already formed in the disk, it can help solid materials to accumulate (Lyra et al. 2009 [55]). Although many mechanisms for planetesimal formation are suggested, this process is yet one of the main research topics in planet formation theory to date.

2.4   Formation of Protoplanets

We have seen that planetesimal formation process is a serious problem in planet formation theory. The process following the planetesimal formation - protoplanet formation - is a rather well-investigated process. In this section, we review this process. The key physics in this stage is the gravitational interaction between planetesimals.

2.4.1   Preliminaries

We first summarize some fundamental facts in considering planetesimal growth.

Collision Cross Section between Planetesimals

Collision cross section between two planetesimals with mass (m, m') and radius (r, r') is given by (Safronov 1969 [73])

$$\sigma = \pi(r + r')^2 \Theta, \tag{2.67}$$

where Θ is a gravitational focusing parameter defined by

$$\Theta = 1 + \frac{v_{esc}^2}{v^2}, \tag{2.68}$$

where

$$v_{esc}^2 = \frac{2G(m + m')}{r + r'}. \tag{2.69}$$

The cross section becomes larger than non-gravitating case, $\pi(r + r')$, because gravitational force tends to attract the bodies.

Two-body Relaxation Timescale

In considering the multi-body system interacting with gravitational force, an important timescale is the two-body relaxation timescale (e.g., Chandrasekhar 1960 [13]). This is the timescale of the energy equipartition is realized through the gravitational interaction between bodies and given by

$$t_{2body} \sim \frac{G^2 m^2 n}{v^3} \ln \Lambda, \qquad (2.70)$$

where m is the mass of the particles, n is the number density, and v is the velocity dispersion of the particles, and Λ is the Coulomb logarithm.

Timescale of Protoplanet Formation

The simplest picture of protoplanet formation by coagulation of planetesimals is orderly growth. Let us consider the situation where one planetesimal with mass M and radius R is embedded in a bunch of smaller planetesimals with number density n. We write the mass of small planetesimals by $m \ll M$ and the radius by $r \ll R$ Let us assume that the random velocity of planetesimals is v_r. Assuming perfect accretion, the growth of the large planetesimal is given by

$$\frac{dM}{dt} = mn\pi R^2 \Theta v_r. \qquad (2.71)$$

and the growth timescale is then

$$t_{grow} \sim \left(\frac{1}{M} \frac{dM}{dt} \right)^{-1} \qquad (2.72)$$

Naive estimate of random velocity is $v_r \sim v_{esc}$, which gives $\Theta \sim 2$ and

$$t_{grow} \sim \left(\frac{1}{M} \frac{dM}{dt} \right)^{-1} \qquad (2.73)$$

$$\sim \begin{cases} 4 \times 10^7 \left(\frac{\Sigma_d}{\Sigma_d^{MMSN}} \right)^{-1} \left(\frac{\rho_{mat}}{3\text{gcm}^{-3}} \right)^{\frac{2}{3}} \left(\frac{M}{M_\oplus} \right)^{\frac{1}{3}} \left(\frac{r}{1\text{AU}} \right)^3 \left(\frac{\Theta}{2} \right)^{-1} \left(\frac{M_*}{M_\odot} \right)^{-\frac{1}{2}} \text{yr} \\ 1 \times 10^9 \left(\frac{\Sigma_d}{\Sigma_d^{MMSN}} \right)^{-1} \left(\frac{\rho_{mat}}{1\text{gcm}^{-3}} \right)^{\frac{2}{3}} \left(\frac{M}{10M_\oplus} \right)^{\frac{1}{3}} \left(\frac{r}{5\text{AU}} \right)^3 \left(\frac{\Theta}{2} \right)^{-1} \left(\frac{M_*}{M_\odot} \right)^{-\frac{1}{2}} \text{yr} \end{cases} \qquad (2.74)$$

where upper lines is for inside the snow line and the lower line is for outside and Σ_d^{MMSN} is the surface density of dust particles of the Minimum Mass Solar Nebula.

Outside the snow line, the formation timescale of protoplanets is very long. It is longer than the age of the solar system at Neptune or Uranus locations. This is known as one of the difficulties of the standard core accretion scenario.

2.4.2 Runaway Growth of Planetesimals

Careful analyses of the gravitational interactions between planetesimals lead to more sophisticated picture of planetesimal growth: runaway and oligarchic growth. Detailed discussions of such processes are found in a number of articles such as Greenberg et al. (1978) [40], Weatherill and Stewart (1989) [93], or Kokubo and Ida (1998) [47]. Here, we briefly summarize the picture of planetesimal accumulation.

We first consider the evolution of the mass ratio between two planetesimals m_1 and m_2. This is given by

$$\frac{d}{dt}\left(\frac{m_1}{m_2}\right) = \frac{m_1}{m_2}\left(\frac{1}{m_1}\frac{dm_1}{dt} - \frac{1}{m_2}\frac{dm_2}{dt}\right). \tag{2.75}$$

Therefore, if $1/m(dm/dt)$ is the increasing function of m, the mass ratio m_1/m_2 increases, and the initially heavy planetesimals gain more and more weight. This is called runaway growth. On the other hand, if $1/m(dm/dt)$ decreases with m, all planetesimals grow in the same way. This is called orderly growth.

From Equation (2.71),

$$\frac{1}{M}\frac{dM}{dt} = \left[1 + \frac{v_{esc,M}^2}{v_{r,m}^2}\right]\frac{\Sigma_d\pi}{\rho_{mat}^{\frac{2}{3}}M^{\frac{1}{3}}}\Omega_K \tag{2.76}$$

where the mass of planetesimal in question (slightly heavier than ambient planetesimals) is denoted by M, the field planetesimals' mass is denoted by m, and ρ_{mat} is the density of the matter of the planetesimals, which is assumed to be independent of the planetesimal mass.

We now discuss the condition of runaway growth. If $v_{r,m} \gtrsim v_{esc,M}$, it is straightforward to show that

$$\frac{1}{M}\frac{dM}{dt} \propto M^{-\frac{1}{3}}, \tag{2.77}$$

and therefore, the growth is orderly. If $v_{r,m} \lesssim v_{esc,M}$, on the other hand,

$$1 + \frac{v_{esc,M}^2}{v_{r,m}^2} \sim \frac{v_{esc,M}^2}{v_{r,m}^2} \tag{2.78}$$

and therefore,

$$\frac{1}{M}\frac{dM}{dt} \propto v_{r,m}^{-2}M^{\frac{1}{3}}. \tag{2.79}$$

If $v_{r,m}$ is independent of the mass of the larger body M, the runaway growth occurs. In the early stage of the growth of larger bodies, random velocity of

the smaller bodies is determined by the balance between two-body scattering between small bodies (which increases the random velocity) and gas drag (which decreases the random velocity). Therefore, it is likely that the random velocity $v_{r,m}$ does not depend on the mass of larger bodies.

There is yet another condition for runaway growth to happen, which is $v_{r,m} > v_{r,M}$. If it is not the case, the random velocity in equation (2.76) must be the random velocity of the larger bodies, and the growth becomes always orderly. In the early stage of planetesimal growth, it is possible for the condition $v_{r,m} > v_{r,M}$ to be satisfied since dynamical friction of smaller bodies tend to suppress the random velocity of the larger bodies.

2.4.3 Oligarchic Growth and Mass of Protoplanets

During the stage of runaway growth, small number of large bodies grow very rapidly. This stage ends when the gravitational interaction between the grown bodies becomes important. We call the grown bodies which have experienced the runaway growth "protoplanet" hereafter.

The runaway stage ends when two-body relaxation time between protoplanets becomes shorter than that of planetesimals. This condition may be written

$$\frac{t_{2body,m}}{t_{2body,M}} \sim \frac{M^2 n_{S,M}}{m^2 n_{S,m}} \tag{2.80}$$

where n_S is the surface number density. Since mass density of protoplanets is $M n_{S,M}$ and that of planetesimals is $m n_{S,m}$, the gravitational interaction between protoplanets become important before they dominate the mass.

We now estimate the mass of protoplanets. Protoplanets grow by accumulating mass of small planetesimals within their Hill radii, while they repel each other by mutual gravitational scattering. Therfore, the orbital separation between protoplanets is of the order of their Hill's radius and the mass of protoplanets is given by

$$M \sim \Sigma_d 2\pi a f r_H, \tag{2.81}$$

where f is the quantity of the order of unity. Numerical simulation of planetesimal growth shows that $f \sim 10$ (Kokubo and Ida 1998 [47]). Note that Hill radius r_H also contains the mass of protoplanet M. Solving for the mass, we obtain

$$M \sim \begin{cases} 0.05 \left(\frac{\Sigma_d}{\Sigma_d^{MMSN}}\right)^{\frac{3}{2}} \left(\frac{a}{1\mathrm{AU}}\right)^{\frac{3}{4}} \left(\frac{f}{10}\right)^{\frac{3}{2}} M_\oplus \\ 2 \left(\frac{\Sigma_d}{\Sigma_d^{MMSN}}\right)^{\frac{3}{2}} \left(\frac{a}{10\mathrm{AU}}\right)^{\frac{3}{4}} \left(\frac{f}{10}\right)^{\frac{3}{2}} M_\oplus \end{cases} \tag{2.82}$$

where the upper line is for inside the ice line and the lower for outside. The orbital separation of protoplanets is given by

$$\Delta a \sim \begin{cases} 0.04 \left(\frac{\Sigma_d}{\Sigma_d^{MMSN}}\right)^{\frac{1}{2}} \left(\frac{a}{1\text{AU}}\right)^{\frac{5}{4}} \left(\frac{f}{10}\right)^{\frac{3}{2}} \ \text{AU} \\ 1.3 \left(\frac{\Sigma_d}{\Sigma_d^{MMSN}}\right)^{\frac{1}{2}} \left(\frac{a}{10\text{AU}}\right)^{\frac{5}{4}} \left(\frac{f}{10}\right)^{\frac{3}{2}} \ \text{AU.} \end{cases} \tag{2.83}$$

Therefore, at 1AU of Minimum-Mass Solar Nebula, several tens of protoplanets with mass of the order of one tenth of Earth are formed.

It is worth noted that at the onset of the oligarchic growth, the mass ratio of small bodies and large protoplanets may be given by

$$\frac{M}{m} \sim \frac{m n_{S,m}}{M n_{S,M}} \sim \frac{\Sigma_d}{M n_{S,M}} \tag{2.84}$$

$$\sim \begin{cases} 10 \left(\frac{M}{10^{25}\text{g}}\right)^{-\frac{2}{3}} \left(\frac{a}{1\text{AU}}\right)^{\frac{1}{2}} \left(\frac{\Sigma_d}{\Sigma_d^{MMSN}}\right) \left(\frac{f}{10}\right) \\ 30 \left(\frac{M}{10^{26}\text{g}}\right)^{-\frac{2}{3}} \left(\frac{a}{10\text{AU}}\right)^{\frac{1}{2}} \left(\frac{\Sigma_d}{\Sigma_d^{MMSN}}\right) \left(\frac{f}{10}\right) \end{cases} \tag{2.85}$$

where we have used the fact that the most of the mass is carried by planetesimals so $m n_{S,m} \sim \Sigma_d$. The mass of protoplanets is larger than that of planetesimals by approximately one order of magnitude. Therefore, gravitational enhancement factor Θ for collisions between protoplanets and planetesimals may be of the order of ten, which indicates that the timescale of protoplanet formation becomes smaller by one order of magnitude.

2.5 Gas Capture

Massive protoplanets capture gas to form Jupiter-like planets. If Bondi radius of the protoplanets $r_B = GM/c^2$ is larger than their physical radius, they can potentially have atmosphere. This condition may be written

$$M_p > 0.01 M_\oplus \left(\frac{\mu}{2.34}\right)^{-\frac{3}{2}} \left(\frac{T}{300\text{K}}\right)^{\frac{3}{2}} \left(\frac{\rho_{mat}}{1\text{g cm}^{-3}}\right)^{-\frac{1}{2}}. \tag{2.86}$$

Protoplanets satisfy this condition. However, this is not a sufficient condition for the formation of gas giant.

We investigate the equilibrium structure of atmosphere (Mizuno et al. 1978 [62]). We consider spherically symmetric structure. Density of the atmosphere is denoted by ρ, temperature T, and pressure p. Hydrostatic equilibrium is given by

$$\frac{dp}{dr} = -\frac{GM(r)}{r^2}\rho(r), \tag{2.87}$$

where $M(r)$ denotes the mass contained within the radius r. We also assume radiative equilibrium

$$\frac{16\sigma_{SB}T(r)^3}{3\kappa\rho(r)}\frac{dT}{dr} = -\frac{L(r)}{4\pi r^2}, \tag{2.88}$$

where κ is the opacity, $L(r)$ is the luminosity at radius r. If we consider the stage when the planets are bombarded by planetesimals, the heat source is the gravitational energy release of planetesimals. Assuming planetesimals always reach the core radius, $L(r)$ is independent of r and

$$L = \frac{GM_{core}\dot{M}_{core}}{r_{core}}, \tag{2.89}$$

where M_{core} denotes core mass, r_{core} is core radius, and $\dot{M}_{core}$ is the mass accretion rate onto the core. Assuming ideal gas, the equation of state is

$$p(r) = \frac{\rho k_B T}{\mu m_H} \tag{2.90}$$

We now look at the qualitative behavior of the atmosphere. From hydrostatic equilibrium and equation of state,

$$T(r) \sim \frac{\mu m_H}{k_B}\frac{GM}{r}. \tag{2.91}$$

Using radiative equilibrium, the density is given by

$$\rho(r) \sim \frac{\sigma_{SB}}{\kappa L}\left(\frac{\mu m_H}{k_B}GM\right)^4\frac{1}{r^3}. \tag{2.92}$$

Therefore, the mass of the atmosphere M_{atm} is

$$M_{atm} = \int_{r_{core}}^{r_H}dr 4\pi r^2 \rho(r) \tag{2.93}$$

$$\sim \frac{\sigma_{SB}}{\kappa L}\left(\frac{\mu m_H}{k_B}GM\right)\ln\frac{r_H}{r_{core}}, \tag{2.94}$$

where we have assumed $M = M_{atm} + M_{core} \sim M_{core}$ and M is taken outside the integral. Since $L \sim G\dot{M}_{core}\rho_{mat}^{1/3}M_{core}^{2/3}$, we have

$$M_{atm} \sim \beta(M_{atm} + M_{core})^4 M_{atm}^{-\frac{2}{3}}, \tag{2.95}$$

where

$$\beta = \frac{\sigma_{SB}}{\kappa\dot{M}_{core}\rho_{mat}^{\frac{1}{3}}}\left(\frac{\mu m_H}{k_B}\right)^4 G^3\ln\frac{r_H}{r_{core}}. \tag{2.96}$$

We now calculate how much mass is added to the atmosphere as core grows. From Equation (2.95),

$$\frac{dM_{atm}}{dM_{core}} = \frac{\frac{2}{3}\beta(M_{atm} + M_{core})^3 M_{core}^{-\frac{2}{3}}\left(5 - \frac{M_{atm}}{M_{core}}\right)}{1 - 4\beta(M_{atm} + M_{core})^3 M_{core}^{-\frac{2}{3}}} \tag{2.97}$$

The right hand side of this equation diverges when core mass becomes larger than the critical value,

$$M_{core,cr} \sim \beta^{-\frac{3}{7}} \sim 20 M_{\oplus} \left(\frac{t_{acc}}{10^6 \mathrm{yr}}\right)^{-\frac{3}{7}} \left(\frac{\kappa}{1\mathrm{cm}^2\mathrm{g}^{-1}}\right)^{\frac{3}{7}}. \tag{2.98}$$

Physically, equilibrium configuration is no longer possible because of the self-gravity of the atmosphere. If the core mass becomes larger than this critical core mass, the atmosphere starts to contract to form a compact gas atmosphere, leading to the formation of gas giant.

Very rough estimate of the mass of the gas giant may be given by estimating the mass of the planet when it swallows all of the gas within the ring whose width is given by its Hill radius. Such estimate gives the mass

$$M \sim 2 \times 10^{-4} M_{\odot} \left(\frac{\Sigma_g}{\Sigma_g^{MMSN}}\right) \left(\frac{a}{5\mathrm{AU}}\right)^{\frac{3}{4}}. \tag{2.99}$$

This mass is one order of magnitude smaller than the Jupiter mass. However, it is still possible for the planets to accrete the gas since when the gas is depleted inside the ring, the gas outside the ring can flow into the depleted ring due to the pressure effects or viscous diffusion. It is possible to form Jupiter within the timescale of the age of the solar system.

Chapter 3

Type I Planetary Migration: Review

We have summarized the overview of the core accretion scenario of planet formation in Chapter 2. One of the fundamental assumption in the scenario is that the planets are formed in-situ: they do not move in the disk in radial direction. This assumption is questioned if we consider the effects of gas disk, which is very likely to exist when protoplanets are formed. The gravitational interaction between the gas disk and the planets causes the change of the orbital semi-major axis of the planets. The change in the orbital semi-major axis of the planets are called planetary migration, and it causes the potentially very serious problems in the formation of planetary system. In this chapter, we review the fundamentals of disk-planet interaction and migration.

Planetary migration has several "types" depending on the mass of the planets and gas disk. The mode of disk-planet interaction that occurs when small mass planets are considered is called "type I". If the planet mass becomes large, the mode of planetary migration is called "type II". There is yet another mode called "type III", which occurs when intermediate mass planet and massive disk is considered. In this thesis, we mainly focus on Type I planetary migration.

3.1 Linear Calculation: Formulation

In order to investigate the gravitational interaction between the gas disk and planets, Goldreich and Tremaine (1978) [38] performed two-dimensional linear calculations. By two-dimensional, we mean we consider the values integrated over the disk-thickness. We call calculations "three-dimensional"

when we consider the full calculations including the vertical mode.

We consider cylindrical coordinate (r, ϕ, z), and integrate all the physical quantities in the z-direction. The basic equations that govern the dynamics of disk gas are given by the equation of continuity and the equation of motion

$$\frac{\partial \Sigma}{\partial t} + \nabla \cdot (\Sigma \mathbf{v}) = 0 \qquad (3.1)$$

$$\frac{\partial \mathbf{v}}{\partial t} + \mathbf{v} \cdot \nabla \mathbf{v} = -\nabla \eta - \nabla \psi + \mathbf{F}_{ext}, \qquad (3.2)$$

where Σ is the surface density of the gas, $\mathbf{v}$ is the velocity field of gas disk, η is enthalpy, and ψ_p is the gravitational potential of the protoplanet, which is treated as perturbation in the subsequent discussion. We denote other forces such as the gravitational force by the central star by $\mathbf{F}_{ext}$, which determines the profile of angular velocity $\Omega(r)$ of the gas disk.

We now consider linear perturbation. All the perturbed variables are denoted by δ, and the background quantities are written with subscript "0". The perturbation equations are

$$\frac{\partial \delta \Sigma}{\partial t} + \nabla \cdot (\Sigma_0 \delta \mathbf{v}) + \nabla \cdot (\delta \Sigma \mathbf{v}_0) = 0 \qquad (3.3)$$

$$\frac{\partial \delta \mathbf{v}}{\partial t} + (\mathbf{v}_0 \cdot \nabla) \delta \mathbf{v} + (\delta \mathbf{v} \cdot \nabla) \mathbf{v}_0 = -\nabla (\delta \eta + \psi). \qquad (3.4)$$

We consider isothermal disk for simplicity. The equation of state is then

$$\delta \eta = c^2 \frac{\delta \Sigma}{\Sigma_0}. \qquad (3.5)$$

We Fourier transform the perturbation in time and azimuthal directions, e.g.,

$$\delta \Sigma(t, r, \phi) = \Re \left[\sum \delta \Sigma(r) e^{-i(\omega t - m\phi)} \right] \qquad (3.6)$$

For brevity, we use the same notation for Fourier component and real space quantities from now on unless otherwise noted. We choose the phase of Fourier transform in such a way that Fourier component of ψ is real. As we shall see, the type I migration is a very slow process compared to Kepler timescale, so we assume that the perturbed pattern is stationary with respect to the planet. Therefore, we assume that the frequency of the perturbation is given by

$$\omega = m\Omega_p. \qquad (3.7)$$

The equation of motion (3.4) is now

$$i(m\Omega - \omega)\delta v_r - 2\Omega \delta v_\phi = -\frac{d}{dr}(\psi + \delta \eta), \qquad (3.8)$$

$$2B\delta v_r + i(m\Omega - \omega)\delta v_\phi = -\frac{im}{r}(\psi + \delta\eta), \tag{3.9}$$

where B denotes Oort B parameter,

$$B = \Omega - A = \Omega + \frac{r}{2}\frac{d\Omega}{dr} \tag{3.10}$$

and A is Oort A parameter

$$A = -\frac{r}{2}\frac{d\Omega}{dr}. \tag{3.11}$$

Solving Equations (3.8) and (3.9) for $\delta\mathbf{v}$,

$$\delta v_r = -\frac{i}{D}\left[(m\Omega - \omega)\frac{d}{dr} + \frac{2m\Omega}{r}\right](\psi + \delta\eta), \tag{3.12}$$

$$\delta v_\phi = \frac{1}{D}\left[2B\frac{d}{dr} + \frac{m}{r}(m\Omega - \omega)\right](\psi + \delta\eta), \tag{3.13}$$

where D is

$$D = \kappa^2 - (m\Omega - \omega)^2, \tag{3.14}$$

and κ is the epicyclic frequency

$$\kappa^2 = 4B\Omega. \tag{3.15}$$

Substituting equations (3.12) and (3.13) into the equation of continuity (3.3), we derive the second order ordinary differential equation for perturbed enthalpy,

$$\left[\frac{d^2}{dr^2} + \left(\frac{d}{dr}\ln\left(\frac{r\Sigma}{D}\right)\right)\frac{d}{dr} \right.$$
$$\left. + \frac{2m\Omega}{r(m\Omega - \omega)}\left(\frac{d}{dr}\ln\left(\frac{\Omega\Sigma}{D}\right)\right) - \frac{m^2}{r^2}\right](\psi + \delta\eta) = \frac{D}{c^2}\delta\eta. \tag{3.16}$$

From this equation, we have density perturbation. Once density fluctuation is obtained the torque exerted on the disk by the gravitational force of the planet is given by

$$T = -\pi m \int dr r\psi(r)\Im[\delta\Sigma(r)]. \tag{3.17}$$

The torque exerted onto the planet by disk gravity is the backreaction of this torque.

The apparent singularities of equation (3.16) are at $r = r_L$ where $D(r_L) = 0$ and $r = r_c$ where $\omega = m\Omega(r_c)$. The former is called Lindblad resonance and the latter is called corotation resonance. Two Lindblad resonances exist for each mode m, one in interior of the planet's orbit and the other resides exterior to the planet's orbit.

3.2   Torque on Lindblad and Corotation Resonances

We now calculate the torque exerted around Lindblad and corotation resonances. We see later that the torque is most effectively exerted in the vicinity of these resonances.

3.2.1   Lindblad Resonances

In order to calculate the torque exerted in the vicinity of Lindblad resonances, we first make a local approximation in the vicinity of the corotation point. This approximation is to assume $d/dr, m/r \gg 1/r$ and that the all the background values which change on the scale of the disk radius are constant except for shear flow, whose variation is taken into account upto the first order of $(r - r_p)/r_p$. This approximation is also known as "shearing-sheet" approximation. Note that if we make this approximation, the interior and exterior part of the disk with respect to the planet become exactly symmetric, and the torque obtained for inner disk and the outer disk is the same except for the overall sign. Therefore, there is no net torque on the planet in this approximation. We later discuss how the difference between the outer and inner parts are incorporated.

We further make tight-winding (WKB) approximation, and thin-disk approximation. Tight-winding approximation is

$$\frac{d}{dr} \gg \frac{m}{r} \tag{3.18}$$

and thin-disk approximation is

$$\frac{c}{r\Omega} \ll 1. \tag{3.19}$$

Tight-winding approximation limits the mode m to be

$$m\frac{c}{r\Omega} \ll 1. \tag{3.20}$$

We later describe how to treat high-m modes.

We expand equation (3.16) around the Lindblad resonances, $r = r_L$. Changing the radial coordinate r to $x = (r - r_L)/r_L$ and using the above described approximations, it is possible to derive

$$\left[\frac{d^2}{dx^2} - \frac{1}{x}\frac{d}{dx} - \beta x \right] \delta\eta = \frac{1}{x}\Psi \tag{3.21}$$

where

$$\beta = \mathcal{D}\frac{r_L^2}{c^2}, \tag{3.22}$$

and

$$\mathcal{D} = \left(r\frac{dD}{dr}\right)_{r=r_L}, \tag{3.23}$$

$$\Psi = \left[r\frac{d\psi}{dr} - \frac{2m\Omega}{\omega - m\Omega}\psi\right]_{r=r_L}. \tag{3.24}$$

The appropriate boundary condition in solving equation (3.21) is that there is no reflection at the boundary. This leads to the solution

$$\delta\eta = \pi\mathrm{sgn}\beta\frac{\Psi}{|\beta|^{\frac{1}{3}}}\left[Gi'(z) \mp iAi'(z)\right] \tag{3.25}$$

where the upper sign is for the disk inside the planet orbit and the lower sign is for the outside the planet orbit. The new radial coordinate z is defined by

$$x = \pm|\beta|^{-\frac{1}{3}}z. \tag{3.26}$$

We denote Airy function by $Ai(z)$, which satisfies

$$\frac{d^2}{dz^2}Ai(z) - zAi(z) = 0 \tag{3.27}$$

and $Gi(z)$ satisfies the equation

$$\frac{d^2}{dz^2}Gi(z) - zGi(z) = -\frac{1}{\pi}. \tag{3.28}$$

Using Equation (3.17), we obtain the torque exerted on Lindblad resonance,

$$T = -\pi^2\Sigma m\frac{1}{\mathcal{D}}\Psi^2. \tag{3.29}$$

3.2.2   Corotation Resonance

We next consider corotation resonances. We write the radial coordinate in the vicinity of the corotation resonance $x = (r - r_c)/r_c$ and expand the equations around $x = 0$. Using tight-winding approximation, we obtain

$$\left[\frac{d^2}{dx^2} + \frac{p}{x} - q^2\right]\delta\eta = -\frac{p}{x}\psi(r_c), \tag{3.30}$$

where

$$p = \left[\frac{2\Omega}{d\Omega/dr} \frac{d}{dr} \ln \frac{\Sigma\Omega}{D} \right]_{r=r_c} \tag{3.31}$$

and

$$q = \left(\frac{\kappa r}{c} \right)_{r=r_c}. \tag{3.32}$$

The order of magnitude of p and q is $p \sim m \ll q \sim r\Omega/c$ and therefore, second term on the right hand side is smaller than third term in the range $q^{-1} \ll x \ll 1$.

The appropriate boundary condition is that $\delta\eta$ does not diverge on the either end of the resonance. Therefore,

$$\delta\eta = \frac{p}{2q} \psi(r_c) \left[e^{qx} \int_x^\infty \frac{dt}{t + i\epsilon} e^{-qt} + e^{-qx} \int_{-\infty}^x \frac{dt}{t + i\epsilon} e^{qt} \right] \tag{3.33}$$

where $\epsilon \ll 1$ is the small positive number. The positivity of ϵ is physically required, considering the causality or the effects of small dissipation. It is possible to derive the waveform for $qx \gg 1$ by calculating equation (3.33). This gives

$$\delta\eta = \frac{p}{q^2 x} \psi(r_c) - i\pi \frac{p}{2q} e^{-|qx|} \tag{3.34}$$

Torque exerted on the corotation resonance is now

$$T = \frac{\pi^2 m}{2} \left[\frac{\psi^2}{d\Omega/dr} \frac{d}{dr} \frac{\Sigma}{B} \right]_{r_c}. \tag{3.35}$$

Comparing Equation (3.29) and (3.35), the torque on Lindblad resonance T_L and T_c may be

$$\frac{T_L}{T_c} \sim m^2. \tag{3.36}$$

Therefore, for high-m mode, Lindblad torque seems more important. Korycansky and Pollack (1993) [48] solved the linearized equations numerically. They have found that total torque including the effects of both corotation and Lindblad torque is differ by a factor of two from that calculated using only Lindblad torque. Therefore, the timescale of planetary migration can be estimated using only the contribution from Lindblad torque, but the corotation torque has non-negligible contribution to the total torque.

Recently, it has been pointed out that the corotation torque can have a significant effects on type I migration rate if non-isothermal effects are considered (e.g., Baruteau and Masset 2008 [10] Paardekooper and Papaloizou 2009 [69]).
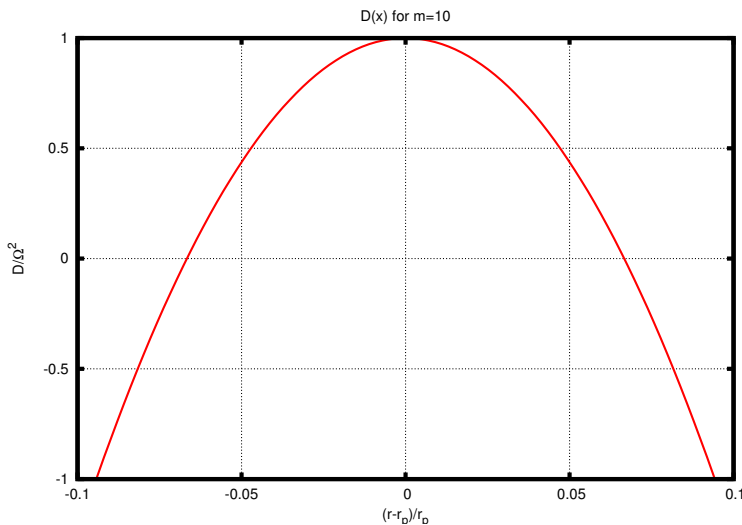
Figure 3.1: The functional form of $D(x)$ for $m = 10$ mode. Horizontal axis shows $x = (r - r_p)/r_p$ where r_p is the corotation radius. If Keplerian rotation is assumed, $D(x) = 1 - (9/4)m^2 x^2$ in the local approximation.

3.3 Waves on the Disk

We have calculated the torque exerted on the disk by the planet's gravitational force. In this section, we look at how this torque is related to the wave on the disk.

We use tight-winding approximation and thin-disk approximation. The equation that governs the wave propagation in the disk is Equation (3.16) without planet's forcing term

$$\left[\frac{d^2}{dr^2} - \frac{D}{c^2} \right] \delta\eta = 0. \qquad (3.37)$$

This equation is of the form of Schrödinger equation, and in the region where $D < 0$, wave propagates (propagation region) while in the region where $D > 0$, wave does not propagate (evanescent region). The form of D is shown in Figure 3.1. Evanescent region resides in the immediate vicinity of the planet's location.

We now investigate the relationship between the angular momentum flux carried by the wave and the torque exerted on the disk. The angular momentum flux carried by the wave is

$$F_A = r^2 \Sigma \int d\phi \, v_r(t, r, \phi) v_\phi(t, r, \phi), \qquad (3.38)$$

where v_r and v_ϕ are the variables in real space. The angular momentum flux carried by the wave with mode m is, using equations (3.12) and (3.13),

$$F_A = \frac{\pi m r \Sigma}{D} \left[\Im(\delta\eta)\Re\frac{d}{dr}(\psi + \delta\eta) - \Re(\psi + \delta\eta)\Im\frac{d}{dr}(\delta\eta) \right] \qquad (3.39)$$

We note that in the absence of the source of perturbation (such as planet potential), angular momentum conserves

$$\frac{dF_A}{dr} = 0. \qquad (3.40)$$

In the region distant away from the planet, the wave angular momentum conserves in the linear perturbation theory.

The angular momentum flux carried by the wave excited at the Lindblad resonance is calculated using Equation (3.25). At the edge of the disk, $z \to -\infty$ the angular momentum flux is

$$F_A \sim \frac{\pi^2 m \Sigma}{|\mathcal{D}|}\Psi^2, \qquad (3.41)$$

which is in complete agreement with the value of the torque excited at Lindblad resonance given by equation (3.29). Therefore, linear calculation states that the torque exerted at Lindblad resonance is carried away to infinity as a form of density wave. It is to be noted that as the density wave propagates in the disk, it damps either by dissipative mechanism or shock damping (e.g., Goodman and Rafikov 2001 [39]).

We have looked at that the torque exerted at Lindblad resonances is equal to the angular momentum flux carried by the density wave. We now investigate the corotation resonance. Since the region near the corotation point is evanescent region, there is no angular momentum flux carried to the disk edge. This can be seen by substituting equation (3.39) in equation (3.34),

$$F_A \sim -\text{sgn}(x)\frac{\pi^2 m}{4}\frac{1}{d\Omega/dr}\left(\frac{d}{dr}\frac{\Sigma}{B}\right)\psi^2(r_c)e^{-|qx|} \qquad (3.42)$$

and therefore there is no angular momentum flux carried to $|x| \to \infty$. However, there is angular momentum flux jump at the corotation,

$$F_A(-0) - F_A(+0) = \frac{\pi^2 m}{2}\frac{1}{d\Omega/dr}\left(\frac{d}{dr}\frac{\Sigma}{B}\right)\psi^2(r_c), \qquad (3.43)$$

which is equal to the torque exerted at the corotation resonance given by equation (3.35). It is noted that at the corotation, small viscous effect denoted by ϵ plays an essential roll.

Inner spiral wave carries angular
momentum flux to −z direction
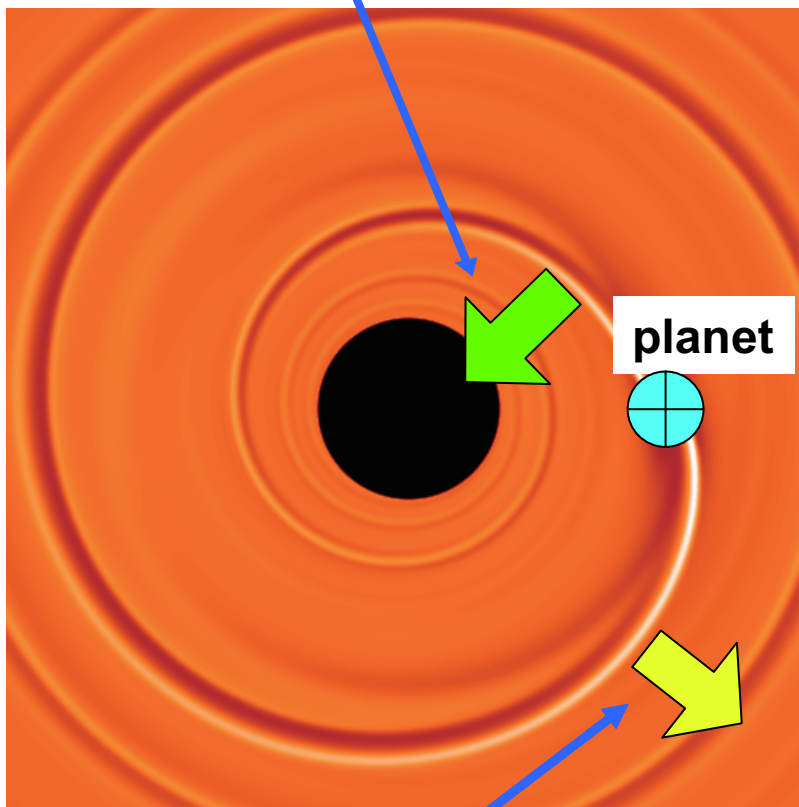
planet

Outer spiral wave carries angular
momentum flux to +z direction

Figure 3.2: Schematic diagram of type I migration. The planet excites the wave in the disk, which carries angular momentum. The planet is exerted torque as a backreaction of this wave excitation. The background figure is taken from the simulation performed by Masset [56].

3.4   Torque cutoff for high-m modes

The analyses by Goldreich and Tremaine use tight-winding approximation and therefore, they can be used for modes $1 \ll m \ll r\Omega/c$. Artymowicz (1993) [4] performed the calculations valid for high-m modes using only local approximation

$$\frac{d}{dr}, \frac{m}{r} \gg \frac{1}{r}. \tag{3.44}$$

In this section, we outline the analysis performed by Artymowicz. We note that using the Goldreich and Tremaine formula (3.29), contribution from high-m modes diverges to give the total torque infinity. The analysis of Artymowicz shows that the modes that give the most dominant contribution to the torque is actually $m \sim r/H$.

For simplicity, the background disk is rotating at Kepler velocity. The perturbation equations are

$$-i(\omega - m\Omega)\frac{\delta\Sigma}{\Sigma} + \frac{d}{dr}\delta v_r + \frac{im}{r}\delta v_\phi = 0 \tag{3.45}$$

$$-i(\omega - m\Omega)\delta v_r - 2\Omega\delta v_\phi + \frac{d}{dr}\delta\eta = -\frac{d}{dr}\psi \tag{3.46}$$

$$\frac{1}{2}\Omega\delta v_r - i(\omega - m\Omega)\delta v_\phi + \frac{im}{r}\eta = -\frac{im}{r}\psi \tag{3.47}$$

and equation of state is

$$\delta\eta = c^2\frac{\delta\Sigma}{\Sigma}. \tag{3.48}$$

From above equations, we obtain

$$\frac{d}{dr}\delta v_\phi - \frac{im}{r}\delta v_r - \frac{1}{2}\Omega\frac{\delta\Sigma}{\Sigma} = 0, \tag{3.49}$$

which corresponds to the conservation of specific vorticity.

We then obtain the equations to write δv_r and $\delta\eta$ in terms of δv_ϕ

$$\delta v_r = -\left(\frac{m^2}{r^2} + \frac{\Omega^2}{c^2}\right)^{-1}\left[\frac{im}{r}\frac{d}{dr}\delta v_\phi - \frac{\Omega}{2c^2}i(\omega - m\Omega)\delta v_\phi + \frac{\Omega}{2c^2}\frac{im}{r}\psi\right] \tag{3.50}$$

$$\delta\eta = -\left(\frac{m^2}{r^2} + \frac{\Omega^2}{c^2}\right)^{-1}\left[-\frac{1}{2}\Omega\frac{d}{dr}\delta v_\phi - \frac{m}{r}(\omega - m\Omega)\delta v_\phi + \frac{m^2}{r^2}\psi\right] \tag{3.51}$$

Substituting these equations into equation (3.46), we obtain a single ordinary differential equation for δv_ϕ,

$$\frac{d^2}{dz^2}\delta v_\phi - \left(D_z + \frac{\gamma^2}{4}\right)\delta v_\phi = R_z \tag{3.52}$$

The symbols in equation (3.52) have the following meaning. We first define D by

$$D = \Omega^2 - (\omega - m\Omega)^2 \qquad (3.53)$$

We call Lindblad resonances defined by $D(r_L) = 0$ the "nominal" Lindblad resonances. We consider the inner resonances for simplicity (outer resonances can be investigated exactly in the same manner.) We take the radial coordinate centered at the nominal Lindblad resonance locations

$$x = \frac{r - r_L}{r_L} \qquad (3.54)$$

and expand D,

$$D \sim 3m\Omega_L^2 x \left(1 - \frac{3}{4}mx + \mathcal{O}(mx^2) \right). \qquad (3.55)$$

Let

$$\beta = +3m\frac{\Omega_L^2 r_L^2}{c^2} \qquad (3.56)$$

and change the radial coordinate

$$z = \beta^{\frac{1}{3}}x. \qquad (3.57)$$

Then,

$$D = \left(3m\Omega_L^2 \frac{c}{r_L} \right)^{\frac{2}{3}} z \left(1 - \frac{3}{8}\gamma z \right) = \left(3m\Omega_L^2 \frac{c}{r_L} \right)^{\frac{2}{3}} D_z, \qquad (3.58)$$

where the right hand side defines D_z and γ is defined by

$$\gamma = \frac{2m}{|\beta|^{\frac{1}{3}}}. \qquad (3.59)$$

The source term of equation (3.52), R_z, is

$$R_z = -\frac{r_L\Omega_L}{2c^2|\beta|^{\frac{1}{3}}} \left(\frac{d}{dz} + \gamma f \right) \psi, \qquad (3.60)$$

where

$$f = \frac{m(\Omega(r) - \Omega_p)}{\Omega(r)} \sim 1 - \frac{3}{2}mx. \qquad (3.61)$$

For later convenience, we define

$$\xi = m\frac{c}{r_L\Omega_L}, \qquad (3.62)$$

which is related to γ by

$$\xi^2 = \frac{3}{8}\gamma^3. \qquad (3.63)$$

We now solve equation (3.52) to find the angular momentum flux carried away by the density wave, which is equal to the torque exerted on the planet. Changing the radial coordinate again to X defined by

$$X = \lambda\left(z - \frac{4}{3\gamma}\right), \qquad (3.64)$$

where

$$\lambda = \left(\frac{3\gamma}{2}\right)^{\frac{1}{4}}. \qquad (3.65)$$

Note that $X = 0$ corresponds to the corotation point. The homogeneous equation for equation (3.52) is now

$$\frac{d^2v}{dX^2} + \left(\frac{1}{4}X^2 - C\right)v = 0, \qquad (3.66)$$

where

$$C = \frac{1 + \xi^2}{3\xi}. \qquad (3.67)$$

The solution of the homogeneous equation may be given by parabolic cylinder function (Abramowitz and Stegun 1956 [1])

$$v_A(z) = \left(\frac{\tau}{2\lambda}\right)^{\frac{1}{2}} E(C, X) \qquad (3.68)$$

$$v_B(z) = \left(\frac{\tau}{2\lambda}\right)^{\frac{1}{2}} E^*(C, -X) \qquad (3.69)$$

where

$$\tau = e^{-\pi C}. \qquad (3.70)$$

Before calculating the solution for equation (3.52), we briefly comment on the wave propagation property described by equation (3.66). The region near the corotation $X = 0$ is evanescent region and the region away from the planet is propagation region. The boundary is given by

$$X = \mp 2\sqrt{C}. \qquad (3.71)$$

This location is called "effective" Lindblad resonance and we denote this with subscript "eff". The distance between the effective Lindblad resonances and the corotation point is

$$|r_{eff} - r_p| = \frac{2}{3}H\frac{\sqrt{1 + \xi^2}}{\xi} \qquad (3.72)$$
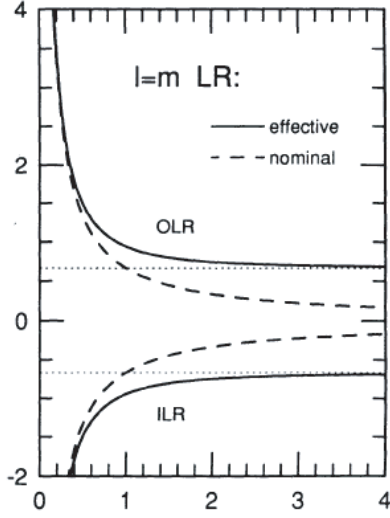
Figure 3.3: Effective and nominal Lindblad resonances. Horizontal axis shows ξ and the vertical axis shows $(r - r_p)/H$. This figure is taken from Artymowicz (1993) [4]

where H is the scale height

$$H = \frac{c}{\Omega}. \tag{3.73}$$

For low-m modes, effective Lindblad resonance and the nominal Lindblad resonances coincide, but for high-m modes, $\xi \to \infty$,

$$|r_{eff} - r_c| \to \frac{2}{3}H. \tag{3.74}$$

Figure 3.3 shows the locations of these resonances.

The solution for equation (3.52) is then

$$\delta v_\phi = -v_A(z) \int_{-\infty}^{z} v_B(s) R_z(s) ds + v_B(z) \int_{\infty}^{z} v_A(s) R_z(s) ds. \tag{3.75}$$

Angular momentum flux carried by the wave to infinity is then calculated as

$$F = \frac{\pi^2 m \Sigma}{|\mathcal{D}|} \Psi^2, \tag{3.76}$$

where Ψ is given by

$$\Psi = \left(\frac{\tau}{2\pi(1 + 4\xi^2)} \right)^{\frac{1}{2}} |\beta|^{\frac{1}{3}} \int_{-\infty}^{\infty} dz v_A(z) \left(\frac{d}{dz} + \gamma f \right) \psi. \tag{3.77}$$

In case where two effective Lindblad resonances are well separated, equation
(3.77) takes a simple form

$$T = \frac{\pi^2 m \Sigma}{|\mathcal{D}|} \frac{1}{(1 + 4\xi^2)(1 + \xi^2)^{\frac{1}{2}}} \left[\frac{d\psi}{dx} + 2mf\psi \right]^2_{eff}. \tag{3.78}$$

We compare the torque formula by Goldreich and Tremaine (3.29) and
Artymowicz formula (3.78) to investigate the most dominant mode for torque.
The Fourier transform of the gravitational potential can be well approximated
by modified Bessel function

$$\psi \propto K_0(m|x|) \tag{3.79}$$

where $x = (r - r_p)/r_p$. Goldreich and Tremaine formula states that the
torque is proportional to the strength of the potential at nominal Lindblad
resonances. The location of nominal Lindblad resonances is $|r_L - r_p| \propto 1/m$
for high-m modes, the value of the potential at the resonance is independent
of the mode number m, and we end up with $T \propto m^2$ (note that there
is another m contribution from $\mathcal{D}$). Therefore, contribution from high-m
modes diverges. On the other hand, Artymowicz formula states that the
torque is determined by the values at effective Lindblad resonances, whose
distance from the corotation point is $\sim H$ for high-m modes. Therefore,
the gravitational potential for such modes are $\psi \propto K_0(mH)$, which strongly
damps as m gets larger. This cutoff at high-m modes is called "torque
cutoff". This keeps the torque from diverging, and the most dominant modes
for torque is found to be $m \sim r/H$.

3.5   Differential Torque

Torque formula (3.29) and (3.78) are the torque exerted one side of the
torque. If we use local approximation, the torque exerted on the inner disk
and the outer disk is the same except for the overall sign. In reality, there is
difference between inside and outside the planet's orbit, which makes overall
torque non-zero. The sum of the torque contribution from both sides of the
disk is called differential torque. In this section, we briefly discuss the cause
of the difference and see that the planet tends to migrate inward. Detailed
calculations may be found in Ward (1986, 1997) [90] [91].

There are three contribution to the differential torque. The first contribu-
tion is the asymmetry of the position of Lindblad resonances. For example,
if the disk rotation is Keplerian, the position of the Lindblad resonances is
given by

$$\Omega(r_L) = \frac{m}{m \mp 1} \Omega_p, \tag{3.80}$$

where upper sign is for the disk interior to the planet orbit, and the lower sign is for the exterior disk. For the same mode m, outer Lindblad resonances always reside closer to the planet. The second contribution is the asymmetry of the magnitude of $\mathcal{D}$. For Keplerian disk,

$$|\mathcal{D}| = \left| r \frac{dD}{dr} \right| = 3\Omega_p^2 \frac{1}{m \mp 1}. \tag{3.81}$$

Therefore, the magnitude of $\mathcal{D}$ is always larger for interior disk. The third contribution is the asymmetry of the gravitational potential Ψ. The value of Ψ for outer disk is larger than for the inner disk (Ward 1997 [91]). These three contributions makes the outer torque stronger than the inner torque. Therefore, planets tend to migrate inward if isothermal disk is considered.

We also note the effect called pressure buffer. Torque formula (3.29) shows that the torque is proportional to the disk surface density and therefore, one may consider that the planets can migrate outward if the surface density is the decreasing function of the radius. However, there is yet another competing mechanism in this case. If surface density is a decreasing function of radius, pressure is also likely to decrease as a function of radius. Therefore, the disk rotates at slightly sub-Keplerian velocity. In this case, Lindblad resonances are moved slightly inward compared to the Kepler rotation case, which makes the outer Lindblad resonances closer to the planet. This effect compensates the gradient of the surface density. This is called pressure buffer, and the planet is still likely to migrate inward.

Finally, we note that since the most dominant mode contributing to the torque is $m \sim r/H$, the differential torque is of the order H/r smaller than the one-sided torque.

3.6 Timescale of Type I migration

In this section, we estimate the timescale of type I migration by summing up the contributions from all the modes m. We first consider one-sided torque, which is the torque exerted one side of the disk with respect to the planet's orbit.

For the sake of order-of-magnitude estimate, we only consider Lindblad torque. Torque from low-m modes can be estimated by the Goldreich-Tremaine formula (3.29), while the contribution from high-m modes are negligible because of the torque cutoff. The maximum mode to be considered, m_{max} is $\sim r/H$. The contribution to the torque from each mode is given by

$$T_m \sim \frac{4}{3} \frac{\Sigma}{\Omega_L^2} \left(\frac{GM_p}{r_p} \right)^2 m^2 \left(2K_0 \left(\frac{2}{3} \right) + K_1 \left(\frac{2}{3} \right) \right)^2 \tag{3.82}$$

where the Fourier transform of the gravitational potential is approximated by modified Bessel function. Summing up this from $m = 1$ to $m_{max} \sim r/H$, we have

$$T \sim \frac{4}{9} \frac{\Sigma}{\Omega_L^2} \left(\frac{GM_p}{r_P} \right)^2 \left(\frac{r\Omega}{c} \right)^3 \left(2K_0 \left(\frac{2}{3} \right) + K_1 \left(\frac{2}{3} \right) \right)^2 \qquad (3.83)$$

for one-sided torque. Since differential torque is smaller than the one-sided torque by a factor of H/r, the total torque is

$$T \sim \frac{\Sigma}{\Omega_L^2} \left(\frac{GM_p}{r_p} \right)^2 \left(\frac{r\Omega}{c} \right)^2 \qquad (3.84)$$

We estimate the timescale of the planetary migration τ_{mig} using equation (3.84). Since

$$\tau_{mig}^{-1} = \frac{1}{r_p} \frac{dr_p}{dt} = \frac{2}{L_p} \frac{dL_p}{dt} = \frac{2T}{L_p}, \qquad (3.85)$$

where L_p is the orbital angular momentum of the planet, the migration timescale is given by

$$\tau_{mig}^{-1} \sim 2 \frac{\Sigma r_p^2}{M_c} \frac{M_p}{M_c} \left(\frac{r\Omega}{c} \right)^2 \Omega_K \qquad (3.86)$$

where Ω_K is the Keplerian angular frequency. Substituting typical parameters, we have

$$\tau_{mig} \sim 2 \times 10^5 \text{yr} \left(\frac{\Sigma r_p^2 / M_\odot}{4 \times 10^{-4}} \right)^{-1} \left(\frac{M_p / M_\odot}{3 \times 10^{-6}} \right)^{-1} \left(\frac{c/r\Omega}{0.05} \right)^2, \qquad (3.87)$$

which is shorter than the observed disk dispersal timescale (e.g., Haisch et al 2001 [41]). Since the direction of migration tends to inward, the planet would fall onto the central star even if they are formed, which causes a serious problem in the theory of planetary system formation. Detailed three-dimensional linear calculations (Tanaka et al. 2002 [83]) and numerical simulations (e.g., D'Angelo et al. 2003 [19]) also supports this conclusion.

Our calculation upto now considered isothermal, non-magnetized, laminar disk. If we break these assumptions, the very direction of migration becomes under question. It has been pointed out recently that there may be a way to halt type I migration by ordered magnetic field (Terquem 2003 [86]), non-isothermal effects (Paardekooper et al. 2009 [68]), turbulence (Nelson and Papaloizou 2004 [65]), or so on. The timescale given by equation (3.84) gives a good estimate, but the direction can be both outward and inward.

One of the main research topic in planet formation theory is to calculate migration rate under various circumstances, to find a "good" disk for planet formation. Planetary migration was totally neglected in the original core-accretion scenario. It is now necessary to construct more realistic formation theory which takes into account the effects of inward or outward planetary migration.

Chapter 4

Effects of Magnetic Field

The properties of planetary migration may be totally different if magnetic field is considered. Nelson and Papaloizou (2004) [65] performed numerical calculations of type I migration in a magnetized disk and indicated that the turbulence due to MRI would result in stochastic torque on the planet. A simple model for the random torque was presented by Laughlin et al. (2004) [52]. Terquem (2003) [86] performed the linear analysis of the torque for two-dimensional laminar disk with toroidal magnetic field and indicated that when stronger magnetic field was exerted on the disk inside the planet's orbit than the outside, inward migration might be halted. Fromang et al. (2005) [34] further investigated this situation by numerical calculation and the numerical results showed good agreement with linear analysis.

In this chapter, we review how the properties of disk-planet interaction and type I migration are altered by the effects of toroidal magnetic field in Section 4.1. We then extend the investigations to poloidal magnetic field case in Section 4.2 using shearing-sheet analysis. We note that shearing-sheet approximation assumes symmetric structure inside and outside the planet's orbit, and calculate the torque exerted on one side of the disk. However, most of the important physical aspects of disk-planet interaction can be captured by this analysis. We also note that we restrict ourselves to a laminar disk, the case without MRI, and derive analytic formulae of torque exerted on some important resonances. We perform a three-dimensional calculation and our formalism is a natural extension of previous studies of unmagnetized cases that is developed by Goldreich and Tremaine (1979) [38] and Artymowicz (1993) [4]. Type I migration in a disk with strong poloidal magnetic field may be also important in the formation of planets around neutron stars (e.g., Bailes et al. 1991[5]).

4.1   The Effects of Toroidal Magnetic Field

Terquem (2003) [86] performed linear analysis of disk-planet interaction including the effects of toroidal magnetic field. There is a large uncertainty in the configuration of magnetic field in protoplanetary disks. However, it may be possible that toroidal field dominates as a result of MRI. Moreover, the analyses with toroidal field is slightly simpler than poloidal case, since calculations restricted only modes without vertical variation is necessary. In this section, we briefly summarize the analyses by Terquem (2003) [86].

4.1.1   Basic Equations

Basic equations are the equation of continuity,

$$\frac{\partial \rho}{\partial t} + \nabla \cdot (\rho \mathbf{v}) = 0 \tag{4.1}$$

equation of motion,

$$\rho \left[\frac{\partial \mathbf{v}}{\partial t} + (\mathbf{v} \cdot \nabla)\mathbf{v} \right] = -\nabla p + \frac{1}{4\pi}(\nabla \times \mathbf{B}) \times \mathbf{B} - \rho \nabla \psi \tag{4.2}$$

and induction equation,

$$\frac{\partial \mathbf{B}}{\partial t} = \nabla \times (\mathbf{v} \times \mathbf{B}). \tag{4.3}$$

We consider thin disk and average the physical quantities in the z-direction. Equation of continuity is

$$\frac{\partial \Sigma}{\partial t} + \nabla \cdot (\Sigma \mathbf{v}) = 0, \tag{4.4}$$

where Σ is the surface density of the disk. Other equations takes similar form. We assume the equation of state with

$$c^2 = \frac{d\langle p \rangle}{d\Sigma}, \tag{4.5}$$

where $\langle \rangle$ denotes the averaging over the z-direction.

We use cylindrical coordinate (r, ϕ, z), and the unit vectors are denoted by $\mathbf{e}$, e.g., $\mathbf{e}_r$. We assume the background rotation profile by $\Omega(r)$ and the magnetic field configuration $(0, B(r,z), 0)$. The Lorentz force is given by,

$$\frac{1}{4\pi}\langle (\nabla \times \mathbf{B}) \times \mathbf{B} \rangle = -\frac{1}{8\pi}\frac{1}{r^2}\frac{d}{dr}(r^2 \langle B^2 \rangle)\mathbf{e}_r = F_r \mathbf{e}_r. \tag{4.6}$$

We now consider the perturbation. From hereon we omit $\langle\rangle$ that denotes z-average. We denote all the perturbed variables by δ, and Fourier transform in the time and azimuthal direction.

$$\delta X(r, \phi, t) = \sum_{m=0}^{\infty} \delta X(r) e^{i(m\phi - \omega t)} \tag{4.7}$$

We then assume the stationary state in a frame co-rotating with the planet,

$$\omega = m\Omega_p. \tag{4.8}$$

Let

$$\sigma = \omega - m\Omega = m(\Omega_p - \Omega) \tag{4.9}$$

and define Lagrangian displacement ξ by

$$\delta v_r(r) = -i\sigma \delta \xi_r(r) \tag{4.10}$$

$$\delta v_\phi = -i\sigma \xi_\phi - \xi_r r \frac{d\Omega}{dr}. \tag{4.11}$$

Using Lagrangian displacement, it is possible to integrate the induction equation. It is convenient to use δW, ξ_r, and δv_ϕ as independent variables, where δW is the enthalpy perturbation

$$\delta W = c^2 \frac{\delta \Sigma}{\Sigma}. \tag{4.12}$$

The perturbed Lorentz force $\delta F_r \mathbf{e}_r + \delta F_\phi \mathbf{e}_\phi$ is given by

$$\delta F_r = \frac{B^2}{4\pi r} \left(r \frac{d^2 \xi_r}{dr^2} + \left(\frac{3}{2} b_1 - 1 \right) \frac{d\xi}{dr} + \left(\frac{1}{2} b_1 - m^2 \right) \frac{\xi_r}{r} \right) \tag{4.13}$$

$$\delta F_\phi = \frac{imb_1}{8\pi} \frac{B^2}{r^2} \xi_r, \tag{4.14}$$

where

$$b_1 = \frac{d \ln(r^2 B^2)}{d \ln r} \tag{4.15}$$

and

$$b_2 = \frac{1}{B^2} \frac{d}{dr} \left(r^2 \frac{dB^2}{dr} \right). \tag{4.16}$$

Perturbation for the equation of continuity is

$$\frac{\sigma}{c^2} \delta W = -\frac{1}{r\Sigma} \frac{d}{dr} (r\sigma \Sigma \xi_r) - \frac{\delta v_\phi}{r} \tag{4.17}$$

and the equation of motion is

$$-m^2\sigma^2\xi_r - 2\Omega\delta v_\phi = -\frac{d}{dr}(\delta W + \psi) + \frac{1}{\Sigma}\left(-\frac{\delta W}{c^2}F_r + \delta F_r\right) \qquad (4.18)$$

$$\sigma\delta v_\phi + \frac{\sigma\kappa^2}{2\Omega}\xi_r = -\frac{1}{r}(\delta W + \psi) - \frac{i}{m\Sigma}\delta F_\phi, \qquad (4.19)$$

where κ is epicyclic frequency. From equations (4.17) and (4.19),

$$\delta v_\phi = \frac{1}{r^2\sigma^2 - c^2}\left[r^2\sigma^2\left(\frac{b_1 v_A^2}{2r^2} - \frac{\sigma\kappa^2}{2\Omega}\right)\xi_r - r\sigma\psi + \frac{c^2}{\Sigma}\frac{d}{dr}(r\sigma\xi_r)\right] \qquad (4.20)$$

and

$$\delta W = \frac{1}{r^2\sigma^2 - c^2}\left[-rc^2\left(\frac{b_1 v_A^2}{2r^2} - \frac{\sigma\kappa^2}{2\Omega}\right)\xi_r + c^2\psi - \frac{c^2 r\sigma}{\Sigma}\frac{d}{dr}(r\sigma\xi_r)\right], \quad (4.21)$$

where v_A is Alfvén velocity

$$v_A^2 = \frac{B^2}{4\pi\Sigma}. \qquad (4.22)$$

Substituting these into equation (4.18), we obtain a single ordinary differential equation for ξ_r,

$$\mathcal{A}_2\frac{d^2\xi_r}{dr^2} + \frac{\mathcal{A}_1}{r}\frac{d\xi_r}{dr} + \mathcal{A}_0\frac{\xi_r}{r^2} = \frac{1}{c^2}\frac{d\psi}{dr} - \mathcal{S}_0\psi, \qquad (4.23)$$

where we have defined

$$\mathcal{A}_2 = 1 + \frac{1}{\beta}\left(1 - \frac{c^2}{r^2\sigma^2}\right) \qquad (4.24)$$

$$\mathcal{A}_1 = \frac{2c^2}{r^2\sigma^2}\left(-1 - \frac{\kappa^2}{2\Omega\sigma} + \frac{2\Omega}{\sigma} + \frac{r^2\sigma^2}{c^2}c_1\right) + 1 + d_1 + \frac{b_1 - 1}{\beta}\left(1 - \frac{c^2}{r^2\sigma^2}\right) \tag{4.25}$$

$$\mathcal{A}_0 = \frac{r^2\sigma^2}{c^2}\left(m^2 - \frac{\kappa^2}{\sigma^2}\right) - d_1^2 + d_2 + 1 - m^2 + 2c_1 d_1 + \frac{2\Omega}{\sigma}d_1$$

$$+ \frac{2r^2\sigma^2}{r^2\sigma^2 - c^2}\left(-\frac{\kappa^2}{2\Omega\sigma} + \frac{2\Omega}{\sigma} - 1 + c_1\right)$$

$$+ \frac{1}{\beta}\left[b_1\left(\frac{2\Omega}{\sigma} - \frac{1}{2} - \frac{d_1}{2}\left(1 + \frac{c^2}{r^2\sigma^2}\right) + \frac{c^2}{r^2\sigma^2 - c^2}\left(-\frac{\kappa^2}{2\Omega\sigma} + \frac{2\Omega}{\sigma} - 1 + c_1\right)\right)\right.$$

$$\left. + \frac{b_1}{2} - m^2 + \frac{c^2}{r^2\sigma^2}(m^2 - 1) - \frac{b_1^2 c^2}{4\beta r^2\sigma^2}\right] \quad (4.26)$$

$$S_0 = \frac{1}{r^2\sigma^2}\left[\frac{2r^2\sigma^2}{r^2\sigma^2 - c^2}\left(\frac{\kappa^2}{2\Omega\sigma} - \frac{2\Omega}{\sigma} + 1 - c_1\right) - \frac{2r^2\Omega\sigma}{c^2} + \frac{b_1}{2\beta}\right] \qquad (4.27)$$

and the parameters are

$$d_1 = \frac{d\ln\Sigma}{d\ln r} \qquad (4.28)$$

$$d_2 = \frac{r^2}{\Sigma}\frac{d^2\Sigma}{dr^2} \qquad (4.29)$$

$$c_1 = \frac{d\ln c}{d\ln r}. \qquad (4.30)$$

Solving the equation (4.23) with outgoing boundary condition, we have ξ_r, which can be used to derive density perturbation through equation (4.21).

We note that we have not used local approximation in this formulation.

4.1.2   Wave on the Disk

We now investigate the wave propagation property on the gas disk. We define $x = (r - r_p)/r_p$ and y by

$$y = \xi_r\exp\left[\frac{1}{2}\int\frac{\mathcal{A}_1}{\mathcal{A}_2}dx\right]. \qquad (4.31)$$

We now obtain, from equation (4.23)

$$\frac{d^2y}{dx^2} + \mathcal{K}y = 0, \qquad (4.32)$$

where

$$\mathcal{K} = \frac{\mathcal{A}_0}{\mathcal{A}_2} - \frac{1}{4}\left(\frac{\mathcal{A}_1}{\mathcal{A}_2}\right)^2 - \frac{1}{2}\frac{d}{dx}\left(\frac{\mathcal{A}_1}{\mathcal{A}_2}\right) \qquad (4.33)$$

The region where $\mathcal{K} > 0$ is propagation region and $\mathcal{K} < 0$ is evanescent region. We also note that $\mathcal{A}_2 = 0$ is singularity. At this singularity,

$$m^2(\Omega - \Omega_p)^2 = \frac{m^2c^2v_A^2}{r^2(v_A^2 + c^2)}. \qquad (4.34)$$

In other words, perturbation frequency by the planet is equal to the frequency of slow wave propagating along the background magnetic field. This point is called magnetic resonance. One magnetic resonance exists in the disk interior to the planet's orbit and another one in the exterior disk.

Figure 4.1 shows the sign of $\mathcal{K}$ and the location of magnetic resonances for each m mode. We note that the wave propagation property is very different from unmagnetized case. Especially, there are two propagation regions in one side of the disk, which corresponds to the two wave modes.
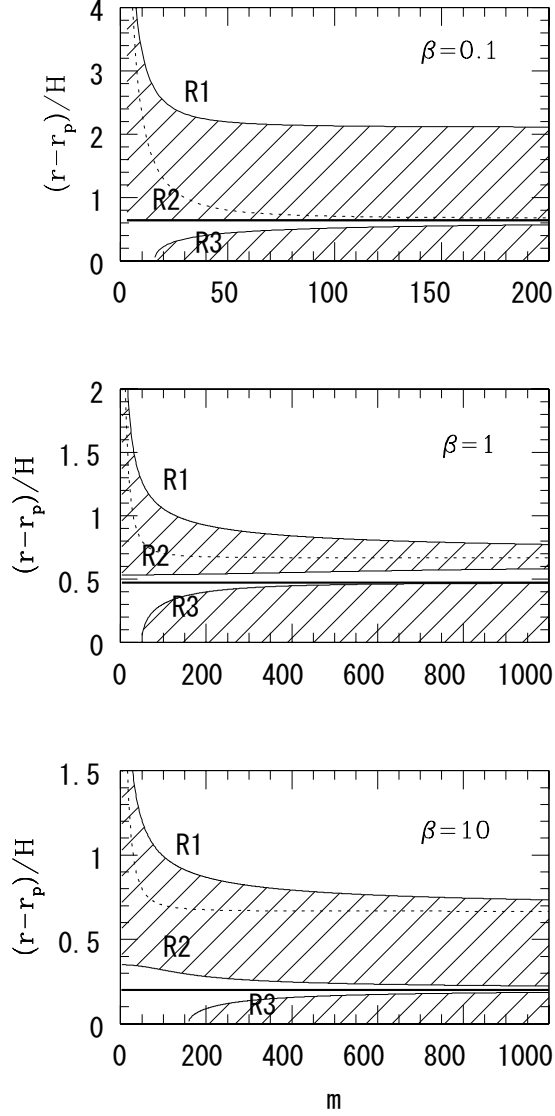
Figure 4.1: Wave propagation property of the disk with toroidal magnetic field. Horizontal axis shows the mode number m and the vertical axis shows the radius normalized by scale height $H = c/\Omega$. In this figure, scale height is fixed at $H/r = 0.03$. Top panel shows the case with $\beta = 0.1$, middle panel shows $\beta = 1$, and the bottom panel shows $\beta = 10$. Lines with R1, R2, and R3 are lines with $\mathcal{K} = 0$, and the thick line denotes the location of magnetic resonance. The shaded regions are wave evanescent region. Dotted line shows the locations of effective Lindblad resonances without magnetic field for comparison. This figure is taken from Terquem (2003) [86].

4.1.3 Divergence of density perturbation at magnetic resonances

We denote the location of magnetic resonance by $r = r_M$. This point is the singularity of equation (4.23). We look at how the solution behaves in the vicinity of this point. We use radial coordinate centered at the resonance, $x = (r - r_M)/r_M$, and take the most dominant terms at $x \sim 0$. Equation (4.23) now becomes

$$x\frac{d^2\xi_r}{dx^2} + \frac{d\xi_r}{dx} + \mathcal{A}\xi = r_M\mathcal{S}, \tag{4.35}$$

where

$$\mathcal{A} = \mp\frac{\beta_M}{3(1 + \beta_M^{\frac{3}{2}}h_M)}\left(\frac{m^2h_M^2}{1 + \beta_M} + 5 + \frac{6}{\beta_M}\right) \tag{4.36}$$

$$\mathcal{S} = \frac{1}{3(1 + \beta_M)h_M}\left[\frac{\mp\beta_M}{(1 + \beta_M)^{\frac{1}{2}}}\left(\frac{1}{r^2\Omega^2}\frac{d\psi}{dx}\right)_{x=0} + \frac{3 + \beta_M}{h_M}\left(\frac{\psi}{r^2\Omega^2}\right)_{x=0}\right]. \tag{4.37}$$

The upper sign denotes the interior disk, and the lower sign denotes the exterior disk. We use the subscript "M" for values evaluated at the resonance locations. The general solution of equation (4.35) is

$$\frac{\xi_r}{r_M} = \frac{\mathcal{S}}{\mathcal{A}} + \frac{\pi}{2}CY_0(2\sqrt{\mathcal{A}x}) + C'J_0(2\sqrt{\mathcal{A}x}), \tag{4.38}$$

where C and C' are constant. The singularity may be regularized by $x \to x + i\gamma$, where $\gamma \ll 1$ is the small positive number. The solution near the magnetic resonance is

$$\frac{\xi_r}{r_M} \sim C\ln\left[4\mathcal{A}(x + i\gamma)\right] \sim C\left(\ln|4\mathcal{A}\gamma| + i\arctan\frac{\gamma}{x}\right) \tag{4.39}$$

Using equations (4.20) and (4.21) to derive δv_ϕ and enthalpy perturbation, we have

$$\frac{\delta W}{r_M^2\Omega^2} \sim C\frac{h_M^2}{\beta_M^2(x + i\gamma)} \tag{4.40}$$

$$\delta v_\phi \sim \mp C\frac{(1 + \beta_M)^{\frac{1}{2}}h_M}{\beta_M(x + i\gamma)} \tag{4.41}$$

which indicates that there is a divergence of the density profile like $1/x$. For $\gamma \to 0$,

$$\frac{1}{x + i\gamma} \to \mathcal{P}\frac{1}{x} - i\pi\delta(x), \tag{4.42}$$

and therefore, strong torque may be exerted at the magnetic resonance.

b_1	$\tilde{T}_m(r_{in}, r_{ILR})$	$\tilde{T}_m(r_{ILR}, r_p)$	$\tilde{T}_m(r_p, r_{OLR})$	$\tilde{T}_m(r_{OLR}, r_{out})$	Total torque $\tilde{T}_m$
8	-172	-110	624	194	536
7	-171	-153	553	186	415
3	-165	-305	408	208	146
2	-163	-344	377	209	79
1	-160	-385	333	211	-1
0	-158	-423	298	217	-66
-1	-154	-463	263	217	-137
-3	-155	-570	184	217	-324
-5	-145	-641	129	225	-432
-8	-105	-645	69	225	-456
	-126	-333	310	170	21

Table 4.1: Torque exerted on the disk with toroidal magnetic field. The magnitude of the torque is normalized by $\Sigma_p r_p^4 \Omega_p^2$, and the parameters are $d_1 = 0$, c is constant, $c/r_p\Omega_p = 0.03$, and $\beta(r_p) = 1$. Results with different magnetic field configuration parameter b_1 are shown for $m = 10$ mode. The bottom line shows the unmagnetized result. This table is taken from Terquem (2003) [86].

4.1.4 Planetary migration in a disk with toroidal magnetic field

Terquem (2003) [86] solved equation (4.23) with outgoing boundary conditions. Figure 4.2 shows the enthalpy perturbation for $m = 10$. As noted in the previous section, there is a strong divergence of enthalpy in the vicinity of magnetic resonances. Figure 4.3 shows the torque exerted at each radius of the disk. It is clearly shown that strong torque is exerted in the vicinity of magnetic resonance.

Table 4.1 shows the torque on the disk exerted by $m = 10$ mode for different magnetic field profile parameter b_1. Contributions to the torque from four regions: from inner edge to the inner Lindblad resonance r_{ILR}, from inner Lindblad resonance to the planet position r_p, from planet position to the outer Lindblad resonance r_{OLR}, and from the outer Lindblad resonance to the outer edge are shown. It is to be noted that if the background magnetic field profile decreases faster than $B \propto r^{-1}$, the net total torque exerted on the disk becomes negative to make the planet migrate outward.

Figure 4.4 shows the total torque exerted by each mode for different values
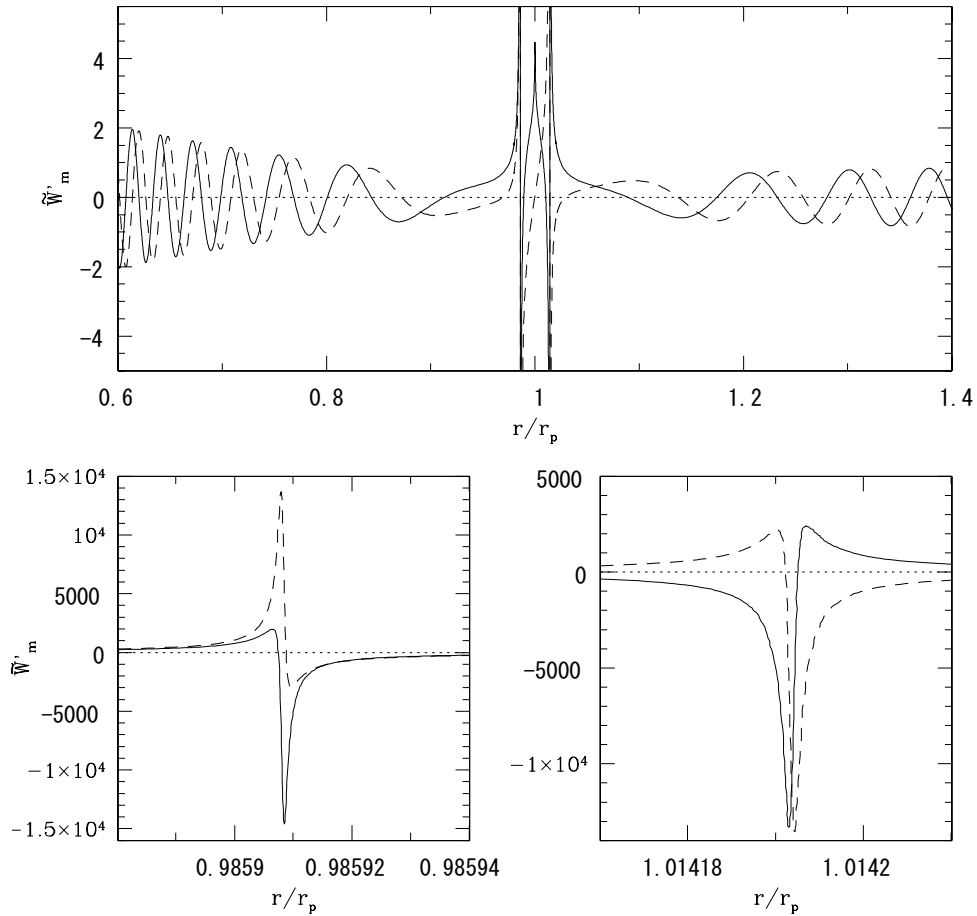
Figure 4.2: Enthalpy perturbation for $m = 10$ mode. Parameters are such that Σ, B^2, and c are constant,$c/(r_p\Omega_p) = 0.03$, and $\beta = 1$. Solid line shows the real part, and the dashed line shows the imaginary part. Bottom two panels show the close-up in the vicinity of the magnetic resonances. This figure is taken from Terquem (2003) [86].

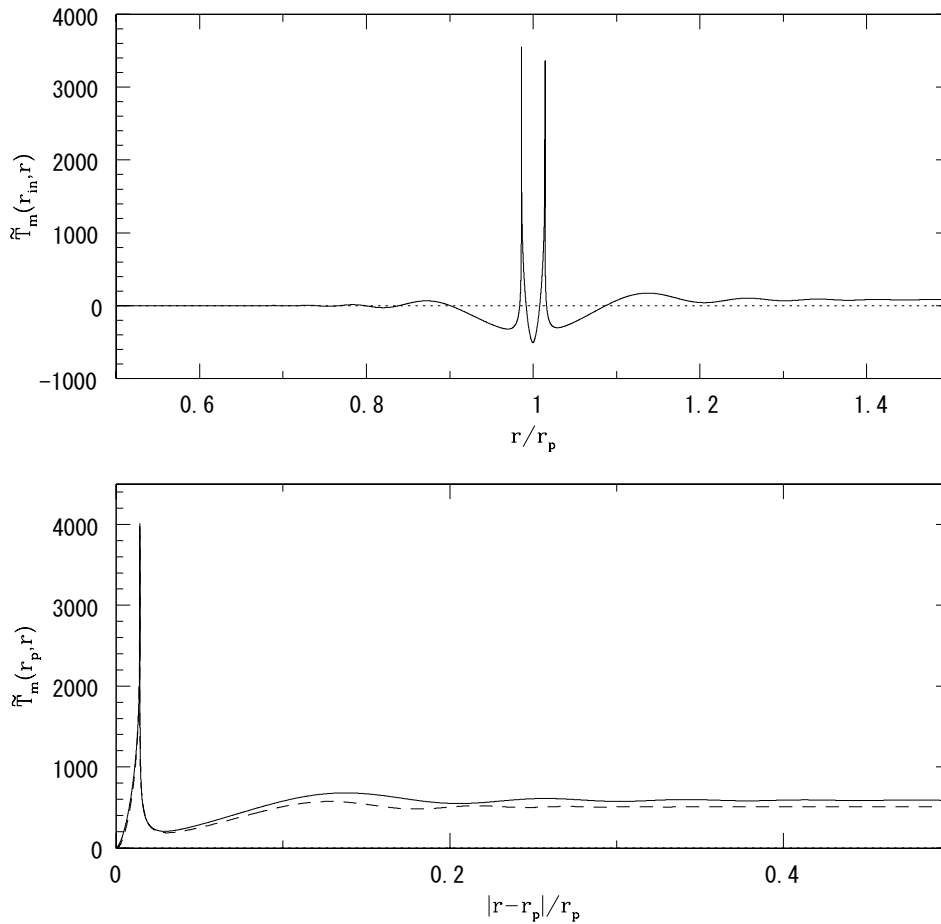Figure 4.3: Torque exerted on the disk with toroidal magnetic field. Parameters are the same as Figure 4.2. Top panel shows the torque integrated from the inner edge to the outer edge. Bottom panel shows the torque integrated from the corotation point to outer (solid line) or to inner (dashed line) edge. The asymmetry between the inner and outer parts give the total differential torque. This figure is taken from Terquem (2003) [86].
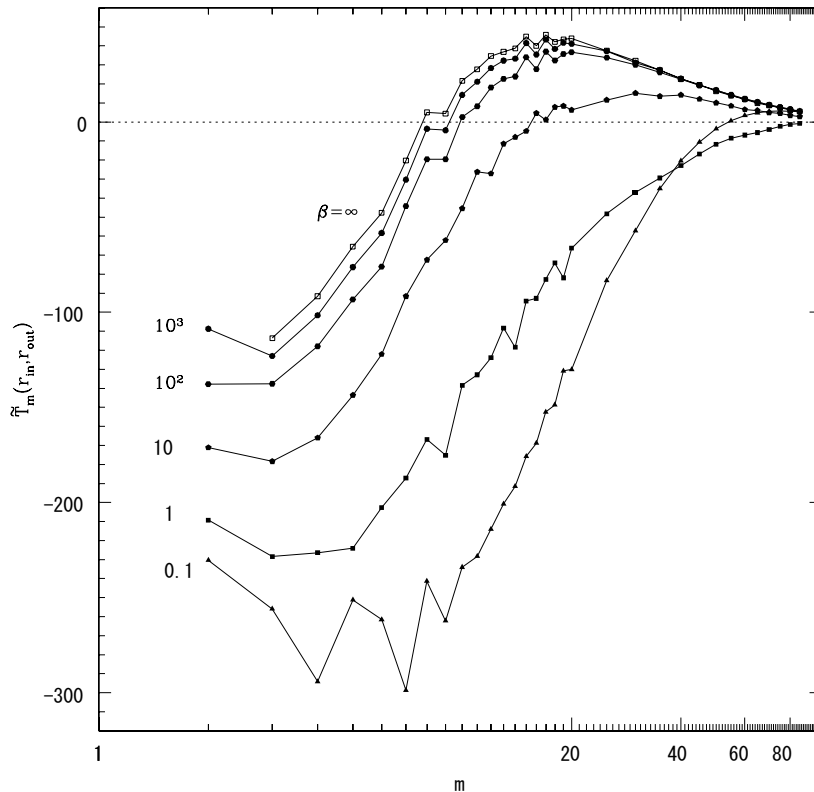
Figure 4.4: Torque exerted on the disk from each mode m with fixed $b_1 = -1$, $d_1 = 0$, $c/(r_p \Omega_p) = 0.03$, and c is constant. The values of $\beta(r_P)$ are varied. This figure is taken from Terquem (2003) [86].

of magnetic field β for fixed $b_1 = -1$. If magnetic field is strong, the torque tends to become negative. If $\beta < 10$, the total torque summed up for all the m-modes become negative, and the planet would migrate outward.

4.2 The Effects of Poloidal Magnetic Field

We have seen that toroidal magnetic field can alter the properties of disk-planet interaction and migration greatly. It would be a natural question what happens if different configuration of magnetic field is considered. In this section, we investigate how poloidal magnetic field alters the disk-planet interaction using linear analyses in the shearing-sheet. The results of linear analyses are then compared with simulation and show good agreement.

For poloidal configuration, it is necessary to perform three-dimensional analyses. For two-dimensional modes, we derive an analytic formula which

generalizes that of Artymowicz (1993). For three-dimensional modes, we employ WKB approximation and derive an analytic torque formula in a strong field limit. We show, for three-dimensional modes, that there is a divergence in perturbed density at certain resonances and the torque is localized at this point. We also show that two-dimensional modes are suppressed by poloidal magnetic field and three-dimensional modes will dominate the total torque if very strong magnetic field is exerted.

4.2.1   Linear Calculation of Torque

Basic Equations

We consider only a local region around the planet using shearing sheet model [64]. Although it gives the same magnitude but the opposite sign of the torque between the inner and outer regions of the planet so the net torque becomes zero, we focus on one side of the disk in this setup and simplify the problem to understand the effect of magnetic field. We assume that the temperature is constant and the self-gravity of the disk is negligible in this local region. The orbit of the protoplanet is assumed to be circular on the equatorial plane of the disk. We set up local Cartesian coordinates with origin at the protoplanet's position and the x-, y-, and z-axes are radial, azimuthal, and vertical direction of the disk, respectively. We use ideal MHD equations:

$$\frac{\partial \rho}{\partial t} + \nabla \cdot (\rho \boldsymbol{v}) = 0 \tag{4.43}$$

$$\frac{\partial \boldsymbol{v}}{\partial t} + (\boldsymbol{v} \cdot \nabla)\boldsymbol{v} = -\frac{1}{\rho}\nabla P - \nabla \psi_{\text{eff}} - 2\Omega_{\text{p}}(\boldsymbol{e}_z \times \boldsymbol{v}) - \frac{1}{4\pi\rho}\boldsymbol{B} \times (\nabla \times \boldsymbol{B}) \tag{4.44}$$

$$\frac{\partial \boldsymbol{B}}{\partial t} = \nabla \times (\boldsymbol{v} \times \boldsymbol{B}) \tag{4.45}$$

where ρ, $\boldsymbol{v}$, P, ψ_{eff}, Ω_{p}, $\boldsymbol{e}_z$, and B are the gas density, velocity, gas pressure, effective potential including tidal force and the planet's gravitational potential, Keplerian angular velocity of the protoplanet, a unit vector directed to the z-axis, and the magnetic flux density, respectively. We adopt an isothermal equation of state, $P = c^2\rho$, where c is sound speed. The Keplerian angular velocity of the protoplanet is given by

$$\Omega_{\text{p}} = \left(\frac{G\,M_{\text{c}}}{r_{\text{p}}^3}\right)^{1/2}, \tag{4.46}$$

where G, M_{c}, and r_{p} are the gravitational constant, mass of the central star, and the distance between the protoplanet and the central star, respectively.

Our calculations are normalized by unit time, $\Omega_{\rm p}^{-1}$, unit velocity, c, and unit length, $h \equiv c/\Omega_{\rm P}$. The effective potential $\psi_{\rm eff}$ in our normalization is given by, assuming a Keplerian disk,

$$\tilde{\psi}_{\rm eff} = -\frac{3}{2}\tilde{x}^2 - \frac{3\tilde{r}_{\rm H}^3}{\tilde{r}}, \tag{4.47}$$

where all the quantities with tilde indicate the normalized value. The first term of the right hand side of equation (4.47) is composed of the gravitational potential of the central star and the centrifugal potential, and higher orders in x, y, and z are neglected. We also neglect the z-dependence of the gravitational potential of the central star for simplicity, and consider later the constant background density. This greatly simplifies the calculation, and we have found that it does not seriously affect the results. The second term of the right hand side of equation (4.47) is the gravitational potential of the protoplanet, where $\tilde{r}_{\rm H}$ and $\tilde{r}$ are normalized Hill radius and the distance from the center of the protoplanet respectively. The Hill radius is defined by $r_{\rm H} = (M_{\rm p}/3M_{\rm c})^{1/3}r_{\rm p}$, where $M_{\rm p}$ is the mass of the protoplanet.

The background disk is assumed to have no planet. The background gas flow has a Keplerian shear, $\boldsymbol{v_0} = -(3x/2)\boldsymbol{e}_y$, background density is assumed to be constant, ρ_0, and the background magnetic field is assumed to be constant and poloidal, $\boldsymbol{B}_0 = B_0\boldsymbol{e}_z$. We denote all the background quantities with subscript zero.

We treat the planet as a perturber on this background disk and derive the stationary pattern excited by the planet, as in Goldreich & Tremaine (1979) [38]. We denote perturbed quantities with δ, e.g., density perturbation is denoted as $\delta\rho$. We Fourier transform in t-, y-, and z-directions, i.e., we shall consider the solution of the form $\delta\rho \propto \exp[-i(\omega t - k_y y - k_z z)]$. Since we consider the stationary pattern, the frequency ω is zero. The perturbed quantities are then

$$\delta\rho(x, y, z) = \sum_{k_y, k_z} \delta\rho_{k_y, k_z}(x)e^{i(k_y y + k_z z)}, \tag{4.48}$$

and the inverse transformation is

$$\delta\rho_{k_y, k_z}(x) = \frac{1}{L_y L_z} \int_{-L_z/2}^{L_z/2} \int_{-L_y/2}^{L_y/2} dy dz \delta\rho(x, y, z)e^{-i(k_y y + k_z z)}, \tag{4.49}$$

where L_y and L_z denote the box sizes of y- and z-directions respectively. Imposing periodic boundary conditions in y- and z- directions, the wave numbers in these directions are $k_y = 2\pi n_y/L_y$ and $k_z = 2\pi n_z/L_z$ respectively,

where n_y and n_z are integer. We shall drop the subscripts k_y and k_z of the Fourier modes unless it is ambiguous.

We define the Lagrangian displacement $\boldsymbol{\xi}$ by

$$\delta v_x = -i\sigma(x)\xi_x, \tag{4.50}$$

$$\delta v_y = -i\sigma(x)\xi_y + \frac{3}{2}\Omega_p\xi_x, \tag{4.51}$$

$$\delta v_z = -i\sigma(x)\xi_z, \tag{4.52}$$

where

$$\sigma(x) \equiv \omega + \frac{3}{2}\Omega_p k_y x. \tag{4.53}$$

Using the Lagrangian displacement, the linearized induction equations are

$$\delta B_x = ik_z B_0 \xi_x, \tag{4.54}$$

$$\delta B_y = ik_z B_0 \xi_y, \tag{4.55}$$

$$\delta B_z = -B_0 \left(\frac{d\xi_x}{dx} + ik_y\xi_y \right). \tag{4.56}$$

The equation of continuity is

$$\frac{\delta\rho}{\rho_0} + \frac{d\xi_x}{dx} + ik_y\xi_y + ik_z\xi_z = 0, \tag{4.57}$$

and the equations of motion become, using the induction equations,

$$(-\sigma^2 \quad -3\Omega_p^2)\xi_x + 2i\Omega_p\sigma\xi_y =$$
$$-(c^2 + v_A^2)\frac{d}{dx}\frac{\delta\rho}{\rho_0} + v_A^2 \left(-k_z^2\xi_x - ik_z\frac{d\xi_z}{dx} \right) - \frac{d\psi_p}{dx}, \tag{4.58}$$

$$-\sigma^2\xi_y \quad -2i\Omega_p\sigma\xi_x =$$
$$-(c^2 + v_A^2)ik_y\frac{\delta\rho}{\rho_0} - v_A^2 \left(-k_y k_z\xi_z + k_z^2\xi_y \right) - ik_y\psi_p, \tag{4.59}$$

$$-\sigma^2\xi_z = -c^2 ik_z\frac{\delta\rho}{\rho_0} - ik_z\psi_p, \tag{4.60}$$

where $v_A^2 = B_0^2/4\pi\rho_0$ denotes the Alfvén velocity of the background gas. We shall also define, for later convenience, the plasma β by c^2/v_A^2.

The equations (4.57), (4.58), (4.59) and (4.60) are four independent equations for four variables $\delta\rho$ and $\boldsymbol{\xi}$. The boundary conditions to be imposed

are such that wave excited propagate away from the planet in both inner and outer parts of the disk.

Once the wave pattern is derived for each Fourier mode, z-component of the torque, of which backreaction causes the orbital migration, exerted on the disk by the planet for each mode is calculated by

$$T_{k_y,k_z} = -2L_y L_z \rho_0 r_p k_y \int \text{Im}\left(\frac{\delta\rho_{k_y,k_z}(x)}{\rho_0}\right)\psi_{\text{pk}_y\text{k}_z}(x)dx, \qquad (4.61)$$

where Im denotes the imaginary part.

Wave Propagation Property of the Disk

We shall investigate the wave propagation property of the disk with poloidal magnetic field. First, we derive a wave equation from (4.57)-(4.60). The x- and y-components of the equations of motion can be written

$$(\sigma^2 + 3\Omega_p^2 - v_A^2 k_z^2)\xi_x - 2i\Omega_p\sigma\xi_y = \frac{df}{dx}, \qquad (4.62)$$

$$(\sigma^2 - v_A^2 k_z^2)\xi_y + 2i\Omega_p\sigma\xi_x = ik_y f, \qquad (4.63)$$

where $f(x)$ is defined by

$$f(x) \equiv \frac{1}{\sigma^2}\left[\left\{(c^2 + v_A^2)\sigma^2 - c^2 v_A^2 k_z^2\right\}\frac{\delta\rho}{\rho_0} + (\sigma^2 - v_A^2 k_z^2)\psi_p\right]. \qquad (4.64)$$

Equations (4.62) and (4.63) are the generalization of equation (10) of Goldreich & Tremaine (1979) [38]. Variable $f(x)$ is related to the perturbation of total pressure $\delta\Pi = c^2\delta\rho + B_0\delta B_z/4\pi$ by

$$f(x) = \frac{\delta\Pi}{\rho_0} + \psi_{\text{p}}. \qquad (4.65)$$

Therefore, it is a natural extension of the variable used by Goldreich & Tremaine (1979) [38] that is $c^2\delta\rho/\rho_0 + \psi_{\text{p}}$. Solving for ξ_x and ξ_y,

$$\xi_x = \frac{1}{D}\left[(\sigma^2 - v_A^2 k_z^2)\frac{df}{dx} - 2\Omega_p\sigma k_y f\right], \qquad (4.66)$$

$$\xi_y = \frac{1}{D}\left[-2i\Omega_p\sigma\frac{df}{dx} + \left(\sigma^2 + 3\Omega_p^2 - v_A^2 k_z^2\right)ik_y f\right], \qquad (4.67)$$

where D is

$$D = (\sigma^2 - v_A^2 k_z^2)(\sigma^2 - v_A^2 k_z^2 + 3\Omega_p^2) - 4\sigma^2\Omega_p^2. \qquad (4.68)$$

This generalizes what is denoted by D in the case of unmagnetized disk, e.g., equation (12) of Goldreich & Tremaine (1979) [38]. Note that in the absence of magnetic field, D is a quadratic function of σ, while this becomes a quartic function in the present situation. From equations (4.57) and (4.60), we finally obtain a second order ordinary differential equation which describes wave excitation and propagation of the disk,

$$\frac{d^2 f}{dx^2} + \mathcal{A}_1 \frac{df}{dx} + \mathcal{A}_2 f = \mathcal{S}, \tag{4.69}$$

where

$$\mathcal{A}_1 = \frac{d}{dx} \ln \frac{\sigma^2 - v_A^2 k_z^2}{D}, \tag{4.70}$$

$$\mathcal{A}_2 = \frac{(\sigma^2 - c^2 k_z^2)D}{\{(c^2 + v_A^2)\sigma^2 - c^2 v_A^2 k_z^2\}(\sigma^2 - v_A^2 k_z^2)}$$
$$+ \frac{2\Omega_p \sigma k_y}{\sigma^2 - v_A^2 k_z^2} \frac{d}{dx}(\ln D) - k_y^2, \tag{4.71}$$

$$\mathcal{S} = \frac{\sigma^2 D}{\{(c^2 + v_A^2)\sigma^2 - c^2 v_A^2 k_z^2\}(\sigma^2 - v_A^2 k_z^2)} \psi_p. \tag{4.72}$$

Imposing WKB approximation, df/dx, $k_z f \gg k_y f$, this equation simplifies to
Schrödinger type:

$$\frac{d^2 f}{dx^2} + V(x)f = \mathcal{S} \tag{4.73}$$

where

$$V(x) = \frac{(\sigma^2 - c^2 k_z^2)D}{\{(c^2 + v_A^2)\sigma^2 - c^2 v_A^2 k_z^2\}(\sigma^2 - v_A^2 k_z^2)}. \tag{4.74}$$

The regions where $V(x) > 0$ are wave propagation regions, and those where $V(x) < 0$ are evanescent. The boundary between these regions, where $V(x) = 0$ or $V(x) = \pm\infty$, is the resonances. Figure 4.5 shows the appropriately normalized potential $V(x)$ for disk with $\beta = 0.9$ and mode $k_y h = 0.196$ and $k_z h = 3.14$.

There are two or three points where $V(x) = 0$ in one side of the disk with respect to the planet (either $x > 0$ or $x < 0$), depending on the value of β. From the condition $D = 0$, we have

$$\sigma^2 = v_A^2 k_z^2 + \frac{1}{2}\left[\Omega_p^2 \pm \sqrt{\Omega_p^4 + 16\Omega_p^2 v_A^2 k_z^2}\right] \tag{4.75}$$

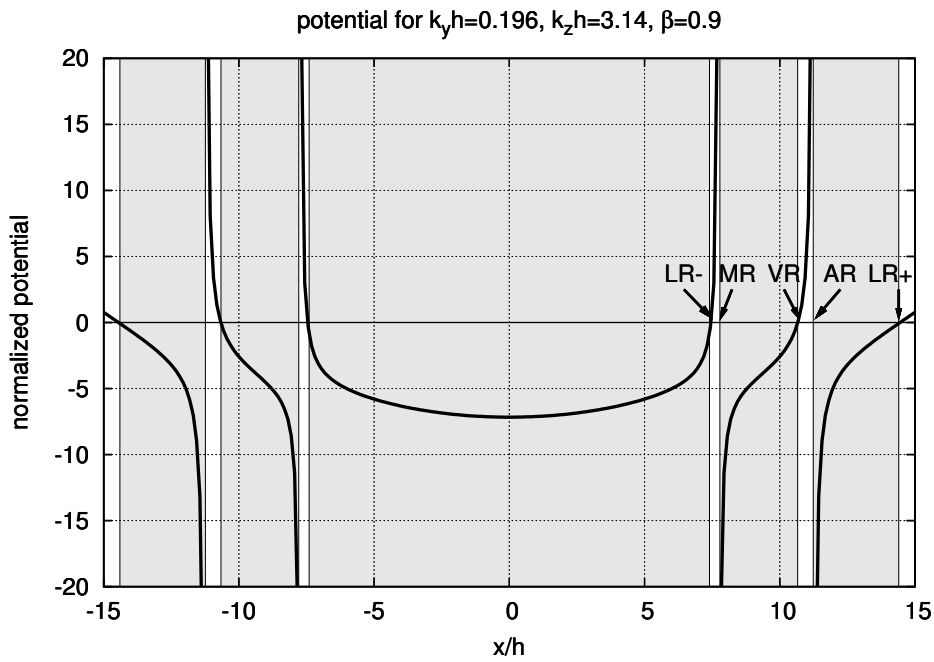Figure 4.5: Potential $V(x)$ given by equation (4.74) for $\beta = 0.9$, $k_y h = 0.196$, and $k_z h = 3.14$. Resonance positions in the outer disk ($x > 0$) are indicated. LR+ and LR− denote Lindblad resonances, AR denotes Alfvén resonance, VR denotes vertical resonance, and MR denotes magnetic resonance. The grey regions correspond to the evanescent regions. Note that regions $|x/h| > 15$ are all propagation regions.

We call the point with positive sign Lindblad Resonance Plus (LR+) and with negative sign Lindblad Resonance Minus (LR−). In the unmagnetized disk, LR+ coincides with the usual Lindblad resonance, $\sigma^2 = \kappa^2$, where κ is the epicycle frequency, and LR− degenerates into corotation point. We note that LR− exists only when $v_A^2 k_z^2 > 3\Omega_p^2$, which is exactly the same as the stability condition against MRI [6]. When LR− does not exist but $k_z \neq 0$, the corotation region becomes a wave propagation region. Since $\sigma = 0$ at the corotation, this indicates that there is a mode with zero frequency but non-zero wavelength, and therefore, in general, there is an unstable mode. Another condition for $V(x) = 0$ is

$$\sigma^2 = c^2 k_z^2. \tag{4.76}$$

This condition does not depend on magnetic field strength. This resonance corresponds to that found by Takeuchi & Miyama (1998) [81] and is named "Vertical Resonance" by Zhang & Lai (2006) [94]. We shall also call this point Vertical Resonance (VR) in this paper.

There are two points in one side of the disk where $V(x)$ diverges. One is given by

$$\sigma^2 = v_A^2 k_z^2. \tag{4.77}$$

At this point, the radial wavelength of Alfvén wave becomes zero. We shall call this point Alfvén Resonance (AR). Note that this divergence is related to what is called Alfvén resonance in plasma physics (see e.g., Stix 1992 [80]). The other point where $V(x)$ diverges is given by

$$\sigma^2 = \frac{c^2 v_A^2 k_z^2}{c^2 + v_A^2}. \tag{4.78}$$

At this point, the wavelength of the slow mode becomes zero, and this corresponds to "Magnetic Resonance" found by Terquem (2003) [86] in the analysis of toroidal field. Therefore, we shall also call this point Magnetic Resonance (MR) in this paper.

For two-dimensional modes, $k_z = 0$, only LR+ exists, and the region in the vicinity of the corotation is evanescent region, whereas the regions further away from LR+ are propagation regions. The details of the wave propagation property of the disk depend on the value of β and k_z, but in general, there are three propagation regions on one side of the corotation, corresponding to the three wave modes of the magnetohydrodynamics. There are only two propagation regions in the analysis of Terquem (2003) [86], since the mode is restricted to $k_z = 0$ and the Alfvén wave with $\delta v_z \neq 0$ is not taken into account. Figure 4.6 shows the wave propagation property of one side of the disk in the case of $\beta < 1$.
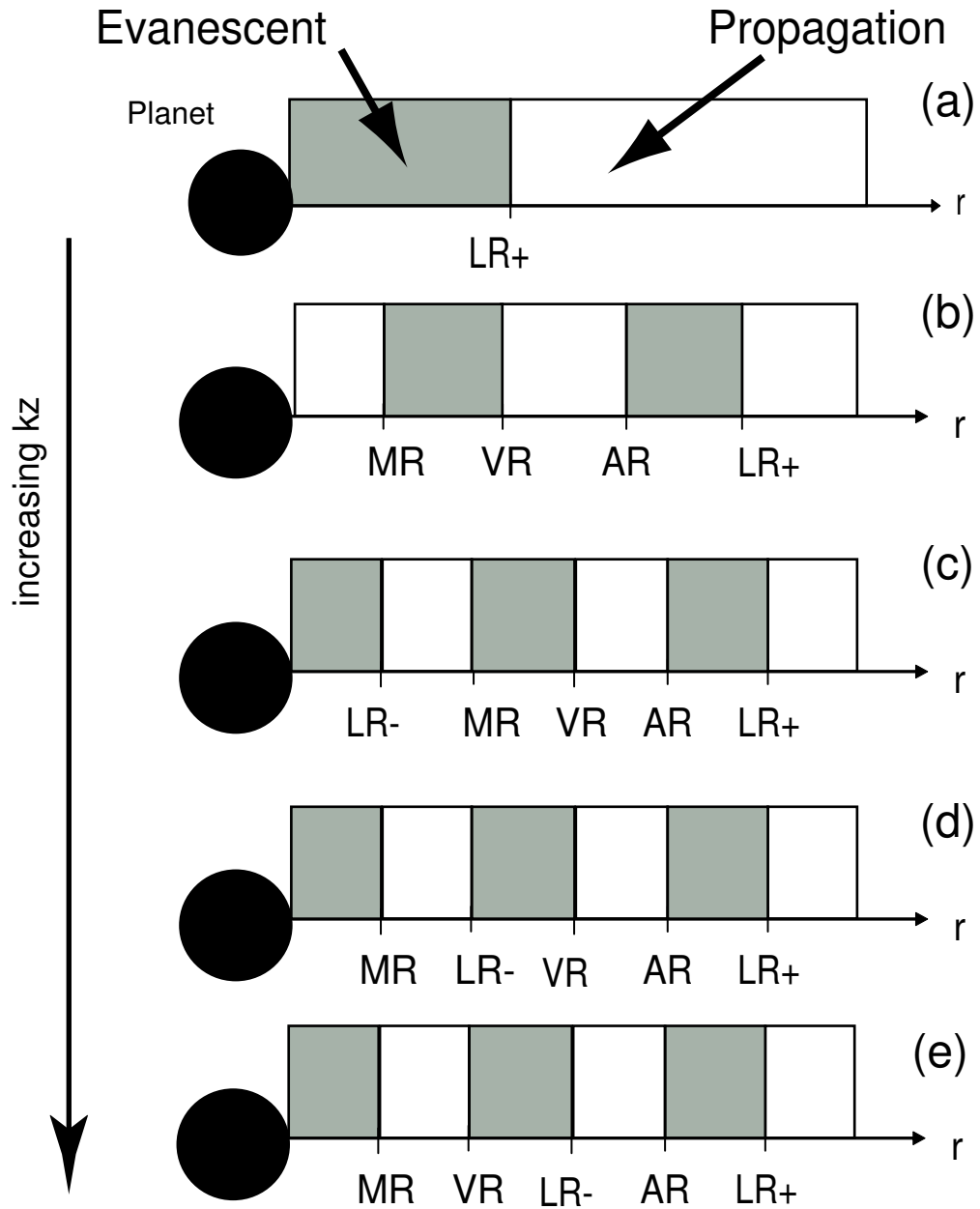
Figure 4.6: Wave propagation property for $\beta < 1$ disk. The parameters used in figure 4.5 corresponds to case (c).

With careful investigation of the properties of the resonances, it is possible to analyze the wave excitation, propagation, and absorption. In this paper, however, we calculate the torque in some restricted cases and compare the results with numerical calculation. We first investigate the case when $k_z = 0$. We then calculate three dimensional modes, $k_z \neq 0$, when very strong magnetic field is exerted. In these cases, MRI does not occur [6], and we expect the wave pattern becomes stationary with respect to the planet's motion.

Two Dimensional Mode: $k_z = 0$

We consider the two-dimensional, or $k_z = 0$, mode. In this case it is possible to calculate the torque exerted on the disk without imposing WKB approximation. When $k_z = 0$, it is clear from equation (4.60) that the fluid particles do not move along z-axis, $\xi_z = 0$, and the effect of magnetic field appears only in the pressure term. The sound speed becomes the phase velocity of the fast mode, $c^2 + v_A^2$, and this acts as an effective sound speed. We can then follow the track of Artymowicz (1993) [4] and calculate the torque exerted on the disk by evaluating the angular momentum flux carried by the wave at $|x| \to \infty$.

The position of the effective Lindblad resonance is given by

$$\sigma^2(x_{\text{eff}}) - \Omega_p^2 - c^2 k_y^2 (1 + \beta^{-1}) = 0. \tag{4.79}$$

When

$$\frac{\Omega_p^2 + c^2 k_y^2 (1 + \beta^{-1})}{\Omega_p c k_y \sqrt{1 + \beta^{-1}}} \gg 1, \tag{4.80}$$

the resonances inside and outside of the corotation radius are well isolated each other, and the torque exerted on the disk may be evaluated by the strength of the gravitational potential of the planet at the resonance point.

We now describe how the formula for one-sided torque is derived. The linearized equations of continuity and motion for $k_z = 0$ modes are

$$-i\sigma \frac{\delta\rho}{\rho_0} + \frac{d}{dx}\delta v_x + ik_y \delta v_y = 0, \tag{4.81}$$

$$-i\sigma \delta v_x + c^2 (1 + \beta^{-1}) \frac{d}{dx}\frac{\delta\rho}{\rho_0} - 2\Omega_p \delta v_y = -\frac{d}{dx}\psi_p, \tag{4.82}$$

$$-i\sigma \delta v_y + \frac{1}{2}\Omega_p \delta v_x + ik_y c^2 (1 + \beta^{-1})\frac{\delta\rho}{\rho_0} = -ik_y \psi_p. \tag{4.83}$$

From these, we obtain the equation for vorticity:

$$\frac{d}{dx}\delta v_y - \frac{1}{2}\Omega_p \frac{\delta\rho}{\rho_0} - ik_y \delta v_x = 0. \tag{4.84}$$

Using the equations of motion, we finally obtain the Schrödinger-type second-order ordinary differential equation for δv_y:

$$\frac{d^2}{dx^2}\delta v_y + \frac{1}{c^2(1+\beta^{-1})}\left[\sigma^2 - \Omega_p^2 - c^2(1+\beta^{-1})k_y^2\right]\delta v_y$$
$$= \frac{1}{c^2(1+\beta^{-1})}\left[-\frac{1}{2}\Omega_p\frac{d\psi_p}{dx} + \sigma k_y\psi_p\right]. \tag{4.85}$$

The position of the effective Lindblad resonance is given by

$$\sigma^2 = \Omega_p^2 + c^2(1+\beta^{-1})k_y^2. \tag{4.86}$$

Waves are evanescent in the region in the vicinity of the planet and the regions further away from the resonance are propagation regions. Waves are excited at the effective Lindblad resonances and propagate away from the planet to $|x| \to \infty$.

We shall now evaluate the angular momentum flux at infinity. The angular momentum flux is calculated by

$$F_A = 2r_p\rho_0 L_y L_z \text{Re}\left[\delta v_x \delta v_y^*\right]. \tag{4.87}$$

Since the gravitational potential of the planet vanishes at infinity, the flux at the infinity is

$$F_A(x \to \infty) = 2r_p\rho_0 L_y L_z \frac{4c^2(1+\beta^{-1})k_y}{\Omega_p^2 + c^2(1+\beta^{-1})k_y^2}\text{Im}\left[\delta v_y^*\frac{d}{dx}\delta v_y\right]. \tag{4.88}$$

The solution of the wave equation (4.85) is given by parabolic cylinder functions. Here, for simplicity, we assume the two resonances, inside and outside the planet, are isolated each other. The equation in the vicinity of the resonance is then given by

$$\frac{d^2}{dz^2}\delta v_y + 2\gamma(z-\gamma)\delta v_y = -S, \tag{4.89}$$

where

$$z = \left[\frac{3\Omega_p k_y}{2c\sqrt{1+\beta^{-1}}}\right]^{\frac{1}{2}}x \tag{4.90}$$

$$\gamma^2 = \frac{2}{3}\frac{\Omega_p^2 + c^2(1+\beta^{-1})k_y^2}{\Omega_p ck_y\sqrt{1+\beta^{-1}}} \tag{4.91}$$

$$S = \frac{\Omega_p}{c(1+\beta^{-1})^{3/4}\sqrt{6\Omega_p ck_y}}\left[\frac{d\psi_p}{dz} - \sigma(1+\beta^{-1})^{1/4}\sqrt{\frac{8ck_y}{3\Omega_p^3}}\psi_p\right]_{\text{eff}}. \tag{4.92}$$

The subscript "eff" denotes the quantity evaluated at the resonance.

We impose the boundary condition as follows. In the evanescent region, the solution does not grow exponentially and in the propagation region, the waves propagate away from the planet. The solution is then

$$\delta v_y = \frac{\pi S}{(2\gamma)^{2/3}} \left\{ \mathrm{Gi}\left[-(2\gamma)^{1/3}(z-\gamma)\right] + i\mathrm{Ai}\left[-(2\gamma)^{1/3}(z-\gamma)\right] \right\} \quad (4.93)$$

Where Ai represents the Airy function and Gi is the solution of the equation [1]

$$\frac{d^2}{dx^2}\mathrm{Gi}(x) - x\mathrm{Gi}(x) = -\frac{1}{\pi}. \quad (4.94)$$

Substituting the equation (4.93) into (4.88), we obtain the torque formula:

$$T_{\mathrm{2D}} = \frac{2\pi}{3} r_p \rho_0 L_y L_z \frac{\Omega_p}{\Omega_p^2 + 4c^2 k_y^2(1+\beta^{-1})} \frac{1}{\sqrt{\Omega_p^2 + c^2 k_y^2(1+\beta^{-1})}} \Psi_{\mathrm{eff}}^2, \quad (4.95)$$

where

$$\Psi_{\mathrm{eff}} = \frac{d\psi_p}{dx}(x_{\mathrm{eff}}) - 2k_y \frac{\sqrt{\Omega_p^2 + c^2 k_y^2(1+\beta^{-1})}}{\Omega_p} \psi_p(x_{\mathrm{eff}}). \quad (4.96)$$

The condition of the isolation of the resonances is satisfied when the solution at one resonance does not affect the other resonance. The distance between the resonances is $\delta z_{\mathrm{res}} \sim \gamma$, while the scale that the solution in the vicinity of one resonance changes in the evanescent region is $\delta z_{\mathrm{wave}} \sim \gamma^{-1/3}$. Hence, resonances are well separated each other when $\delta z_{\mathrm{res}} \gg \delta z_{\mathrm{wave}}$, or $\gamma \gg 1$.

Equation (4.95) generalizes the equation (56) of Artymowicz (1993) [4] to a magnetized disk. Since the effective sound speed becomes faster when poloidal magnetic fields present, the magnitude of the torque becomes smaller. There are two kinds of cutoff mechanism of the torque, as Artymowicz (1993) [4] pointed out. One is mild cutoff that comes from the coefficient of Ψ_{eff}. The other is the sharp cutoff, which is the consequence of the fact that position of the effective Lindblad resonance goes further away from the corotation when magnetic field is stronger. In the case of planetary migration, the effect of sharp cutoff is more important, and the torque by two-dimensional mode is strongly suppressed when $\beta \lesssim 1$. We emphasize that we have obtained the torque formula (4.95) including the torque cutoff at high k_y mode because we have not imposed WKB approximation, and hence, not neglected terms with k_y.

Three Dimensional Mode: $k_z \neq 0$, in the Limit of Strong Magnetic Field

In the unmagnetized disk, the contribution from three-dimensional, or $k_z \neq 0$, mode is small [83]. However, it is indicated in the previous section that the two-dimensional mode is strongly suppressed when strong magnetic field is present. Therefore three dimensional mode may be important in this case. We investigate three-dimensional mode in the limit of $\beta = 0$. We impose WKB approximation in this section.

In the limit of $\beta \to 0$, the resonances LR+, LR-, and AR are infinitely far away from the corotation and we can safely neglect their contribution. The other two resonances, MR and VR, degenerate and the equation (4.69) becomes

$$\frac{d^2 f}{dx^2} - k_z^2 f = S(x), \tag{4.97}$$

where the source term $S(x)$ is

$$S(x) = -\frac{\sigma^2}{\sigma^2 - c^2 k_z^2} \psi_p. \tag{4.98}$$

In this case, waves are evanescent in the vicinity of the corotation, but there is a singularity in the source term at the degenerate point of MR and VR,

$$\sigma_{\mathrm{MR}}^2 = c^2 k_z^2. \tag{4.99}$$

The subscript MR denotes the quantities evaluated at this point. Note that this divergence originally comes from the divergence of the source term (4.71) at MR.

In order to regularize the singularity, we consider the small viscosity effective only in the vicinity of this point. The viscosity is effectively taken into account by adding the small positive imaginary part to the frequency,

$$\sigma(x) \to \sigma(x) + i\epsilon, \tag{4.100}$$

where $\epsilon > 0$ is small positive number (see e.g., Meyer-Vernet and Sicardy 1987 [60]). Taking the limit of $\epsilon \to 0$,

$$\int \frac{g(x)}{\sigma - ck_z} dx = \mathcal{P} \int \frac{g(x)}{\sigma - ck_z} dx - i\pi \int \delta_D(\sigma - ck_z) g(x) dx \tag{4.101}$$

where $g(x)$ is an arbitrary smooth function, $\mathcal{P}$ denotes the principal value of the integration and $\delta_D(x)$ is the Dirac's delta function.

The boundary condition we impose is that the perturbation must vanish for $|x| \to \infty$, i.e.

$$f(x \to \infty) \propto e^{-k_z x}, \tag{4.102}$$

$$f(x \to -\infty) \propto e^{k_z x}. \tag{4.103}$$

The solution that satisfies this condition is

$$f(x) = -\frac{1}{2k_z} \left[e^{-k_z x} \int_{-\infty}^{x} e^{k_z u} S(u) du - e^{k_z x} \int_{+\infty}^{x} e^{-k_z u} S(u) du \right]. \tag{4.104}$$

Substituting $S(x)$, the real and imaginary part of the solution are

$$
\begin{aligned}
\frac{2}{k_z} \mathrm{Re} f &= \mathcal{P} \int_{-\infty}^{x} e^{k_z(u-x)} \psi_p(u) \left[1 + \frac{ck_z}{2} \left(\frac{1}{\sigma(u) - ck_z} - \frac{1}{\sigma(u) + ck_z} \right) \right] du \\
&\quad - \mathcal{P} \int_{+\infty}^{x} e^{k_z(x-u)} \psi_p(u) \left[1 + \frac{ck_z}{2} \left(\frac{1}{\sigma(u) - ck_z} - \frac{1}{\sigma(u) + ck_z} \right) \right] du
\end{aligned}
\tag{4.105}
$$

and

$$
-\frac{6\Omega_p k_y}{\pi c k_z^2 \psi_{p,\mathrm{MR}}} \mathrm{Im} f =
\begin{cases}
e^{k_z x} \left[\exp\left(-\frac{2ck_z^2}{3\Omega_p k_y} \right) - \exp\left(\frac{2ck_z^2}{3\Omega_p k_y} \right) \right] & x < -x_{\mathrm{MR}} \\[3mm]
\exp\left[-\frac{2ck_z^2}{3\Omega_p k_y} \right] \left(e^{-k_z x} - e^{k_z x} \right) & -x_{\mathrm{MR}} < x < x_{\mathrm{MR}} \\[3mm]
-e^{-k_z x} \left[\exp\left(-\frac{2ck_z^2}{3\Omega_p k_y} \right) - \exp\left(\frac{2ck_z^2}{3\Omega_p k_y} \right) \right] & x > x_{\mathrm{MR}}
\end{cases}
\tag{4.106}
$$

In the limit of $\beta \to 0$, the density perturbation is given by

$$\frac{\delta \rho}{\rho_0} = \frac{1}{\sigma^2 - c^2 k_z^2} \left[\frac{\sigma^2}{v_A^2} f + k_z^2 \psi_p \right]. \tag{4.107}$$

In order to calculate the torque, we need imaginary part of $\delta\rho/\rho_0$ which is given by

$$
\begin{aligned}
2ck_z \mathrm{Im} \left[\frac{\delta\rho}{\rho_0} \right] &= -\pi \left\{ \delta_D(\sigma - ck_z) - \delta_D(\sigma + ck_z) \right\} \left(\frac{\sigma^2}{v_A^2} \mathrm{Re} f + k_z^2 \psi_p \right) \\
&\quad + \frac{\sigma^2}{v_A^2} \left\{ \frac{\mathcal{P}}{\sigma - ck_z} - \frac{\mathcal{P}}{\sigma + ck_z} \right\} \mathrm{Im} f.
\end{aligned}
\tag{4.108}
$$

It is possible to show that f does not diverge at the resonance. For simplicity, we set the planet's gravitational potential ψ_p to be constant. The part of the equation (4.105),

$$\int_{-\infty}^{x} du\, e^{k_z(u-x)} - \int_{+\infty}^{x} du\, e^{k_z(x-u)} \tag{4.109}$$

is finite. We consider the rest. Since we are working on the local Cartesian coordinate where inside and outside the planet are symmetric, we assume $x > 0$ without loss of generality. Let I be

$$I = \mathcal{P} \int_{-\infty}^{x} du\, e^{k_z(u-x)} \left[\frac{1}{\sigma(u) - ck_z} - \frac{1}{\sigma(u) + ck_z} \right]$$
$$- \mathcal{P} \int_{-\infty}^{x} du\, e^{k_z(x-u)} \left[\frac{1}{\sigma(u) - ck_z} - \frac{1}{\sigma(u) + ck_z} \right], \tag{4.110}$$

then

$$I = I_A - I_B - I_C + I_D, \tag{4.111}$$

$$I_A = \exp\left[-k_z \left(x - \frac{2ck_z}{3\Omega_p k_y} \right) \right] \text{Ei}\left(k_z x - \frac{2ck_z^2}{3\Omega_p k_y} \right), \tag{4.112}$$

$$I_B = \exp\left[-k_z \left(x + \frac{2ck_z}{3\Omega_p k_y} \right) \right] \text{Ei}\left(k_z x + \frac{2ck_z^2}{3\Omega_p k_y} \right), \tag{4.113}$$

$$I_C = \exp\left[k_z \left(x - \frac{2ck_z}{3\Omega_p k_y} \right) \right] \text{Ei}\left(-k_z x + \frac{2ck_z^2}{3\Omega_p k_y} \right), \tag{4.114}$$

$$I_D = \exp\left[k_z \left(x + \frac{2ck_z}{3\Omega_p k_y} \right) \right] \text{Ei}\left(-k_z x - \frac{2ck_z^2}{3\Omega_p k_y} \right), \tag{4.115}$$

$$\tag{4.116}$$

where Ei denotes the exponential integral,

$$\text{Ei}(w) = \mathcal{P} \int_{-\infty}^{w} dt\, \frac{e^t}{t}. \tag{4.117}$$

We can check I_A, I_B, I_C, and I_D do not diverge at infinity by the asymptotic expansion of the exponential integral,

$$e^{-w} \int_{-\infty}^{w} \frac{e^t}{t} dt \sim \frac{1}{w} \tag{4.118}$$

and the inequality derived from the series expansion of the exponential integral,

$$\text{Ei}(w) = \gamma + \ln w + \sum_{n=1}^{\infty} \frac{w^n}{n\, n!} < \gamma + \ln w + e^w. \tag{4.119}$$

For $x \to \infty$, $I \sim \mathcal{O}(1)$.

We now consider the vicinity of the resonance, $x \sim 2ck_z/3\Omega_p k_y$. Although I_A and I_C are divergent logarithmically, the combination $I_A - I_C$ does not diverge:

$$I_A - I_C \sim \mathcal{P} \int_{-k_z\delta}^{k_z\delta} dt \frac{e^t}{t} \tag{4.120}$$

where we set $x \sim 2ck_z/3\Omega_p k_y + \delta$. It is easy to show $I_B, I_D \sim \mathcal{O}(1)$ and therefore, I is order of unity for all x. Although ψ_p is not strictly a constant, it is smooth in the vicinity of the resonance. Therefore, we can safely assume this to be constant when we discuss the divergence at the resonance.

From (4.105), the order of magnitude of $\mathrm{Re}f$ is

$$\mathrm{Re}f \sim \mathcal{O}\left(\frac{ck_z^2}{\Omega_p k_y}\psi_p\right). \tag{4.121}$$

It is clear from the equation (4.106), the imaginary part of f is also of the same order.

Given that f does not diverge at the resonance, we can neglect the term with σ^2/v_A^2 in right hand side of the equation (4.107) when magnetic field is strong enough. Quantitatively, we can neglect these terms when

$$\frac{\sigma^2}{v_A^2}\frac{ck_z^2}{\Omega_p k_y} \ll k_z^2 \tag{4.122}$$

since $f \sim \mathcal{O}(ck_z^2\psi_p/\Omega_p k_y)$. Since $\sigma^2 \sim c^2 k_z^2$ in the vicinity of the resonance, we obtain

$$\beta \ll \frac{\Omega_p k_y}{ck_z^2}. \tag{4.123}$$

When this condition is satisfied, the imaginary part of the density perturbation is

$$\mathrm{Im}\left[\frac{\delta\rho}{\rho_0}\right] \sim -\frac{\pi k_z}{2c}\left\{\delta_D(\sigma - ck_z) - \delta_D(\sigma + ck_z)\right\}\psi_p. \tag{4.124}$$

The first delta function indicates the torque exerted on the outer disk, and the second inner disk. These torques are of the same magnitude but different in sign. The magnitude of the torque on one side of the disk is then, from (4.61),

$$T_{\mathrm{MR}} = \frac{2\pi}{3}L_y L_z \frac{\rho_0 r_p k_z}{\Omega_p c}\psi_{p,\mathrm{MR}}^2. \tag{4.125}$$

4.2.2 Numerical Calculation

We have performed numerical calculations in order to investigate how well the equations (4.95) and (4.125) describe the realistic value of the torque. We have done two sets of runs. One is for a two-dimensional disk. The other is for a three-dimensional thick disk.

Numerical Methods

We adopt the nested grid method (see, e.g., Machida et al. 2005, Matsumoto & Hanawa, 2003) to obtain high spatial resolution near the planet. Each level of rectangular grid has the same number of cells ($= 64 \times 256$) for 2D run, while ($= 64 \times 256 \times 16$) for 3D run. The cell width $\Delta s(l)$ depends on the grid level l. The cell width is reduced by half with increasing grid level ($l \to l+1$). We use 4 grid levels ($l = 1,2 \cdots 4$) for 2D run and 5 levels for 3D run. The box size of the coarsest grid $l = 1$ is chosen to $(L_x, L_y) = (64h, 256h)$ for 2D run and $(L_x, L_y, L_z/2) = (64h, 256h, 16h)$ for 3D run. Note that in z-direction, the simulation box extends from midplane to $z = L_z/2$. The box size of the finest grid is $(x, y) = (2h, 8h)$ for 2D run and $(x, y, z) = (2h, 8h, h)$ for 3D run. The cell width of the coarsest grid is $\Delta s(1) = h$, while that of the finest grid has $\Delta s(4) = 0.125h$ for 2D run and $\Delta s(5) = 0.0625h$ for 3D run. We assume the fixed boundary condition in the x-direction and periodic boundary condition in the y-direction. For z-direction, we impose a periodic boundary condition between $z = -L_z/2$ and $z = L_z/2$.

For two dimensional calculation, we neglect the z-dependence of the planet potential, i.e. we adopt the potential of the form

$$\psi_p = -\frac{GM_p}{\sqrt{x^2 + y^2}}. \qquad (4.126)$$

We employ the softening in the gravitational potential as follows. The gravitational force $\boldsymbol{F}$ by the planet is given by

$$\boldsymbol{F} = \frac{GM_p}{(r + \varepsilon)^3}\boldsymbol{x}, \qquad (4.127)$$

where ε is the softening length, r is the distance from the planet's position, and $\boldsymbol{x}$ is the position vector. We choose ε such that this equals the mesh size of the finest grid, i.e., $\varepsilon = 0.125h$ for 2D run and $\varepsilon = 0.0625h$ for 3D run.

We fix the planet mass to be $\tilde{r}_H = 0.3$, corresponding to $3M_\oplus$ planets when $M_c = M_\odot$ and $h/r_p = 0.05$, and vary the initial strength of the poloidal magnetic field. We performed the calculations for $\beta = \infty$, 100, 10, 2, 0.3, 0.1, 0.01, and 0.001.

4.2.3 Comparison between Numerical Calculation and Linear Analysis

For all two-dimensional calculations and for three-dimensional calculation with $\beta = \infty$, 0.01, and 0.001, we do not observe MRI and steady states are realized. This is consistent with the stability criterion of MRI derived from linear analysis.

We then Fourier transform the density pattern of the steady state in y- and z-directions and calculate the torque exerted on one side of the disk by equation (4.61), and this torque is compared with the results of linear analysis. The normalization of the torque is taken to be

$$\tilde{T} = \frac{T}{\rho_0 r_p H^4 \Omega_p^2}.$$

(4.128)

We make use of FFT (e.g., Press et al. 1996 [31]). The wavenumber k we evaluate is given by

$$k = \frac{2\pi n}{L},$$

(4.129)

where L is the box size of the y- or z-directions and n is an integer with $-N/2 < n < N/2$ where N is the mesh number. We also Fourier transform the gravitational potential of the planet numerically to obtain the value of ψ_p.

Two-dimensional Calculation

Figure 4.7 shows the stationary pattern of density perturbation obtained by two dimensional calculations for $\beta = 0.01$, 2, and 100. It is clear that, with increasing magnetic field, the amplitude of the wave becomes small and the point where waves are excited goes further away from the planet. Figure 4.8 shows the torque calculated as a result of numerical calculation for various magnetic field strength, or different β. It is clear that the torque becomes weaker as the magnetic field is stronger.

We show in figure 4.9 the comparison between the results of numerical calculation and linear analysis, equation (4.95). It is clear that for modes that satisfy condition (4.80), which we expect that equation (4.95) gives a good approximation for the torque, numerical calculation and linear analysis indeed show reasonably good agreement, at least an order of magnitude, even though equation (4.95) estimates the torque by the value of density perturbation only at the position of effective Lindblad resonance. Therefore, equation (4.95) is useful for estimating two-dimensional torque when poloidal magnetic field is exerted on the disk.
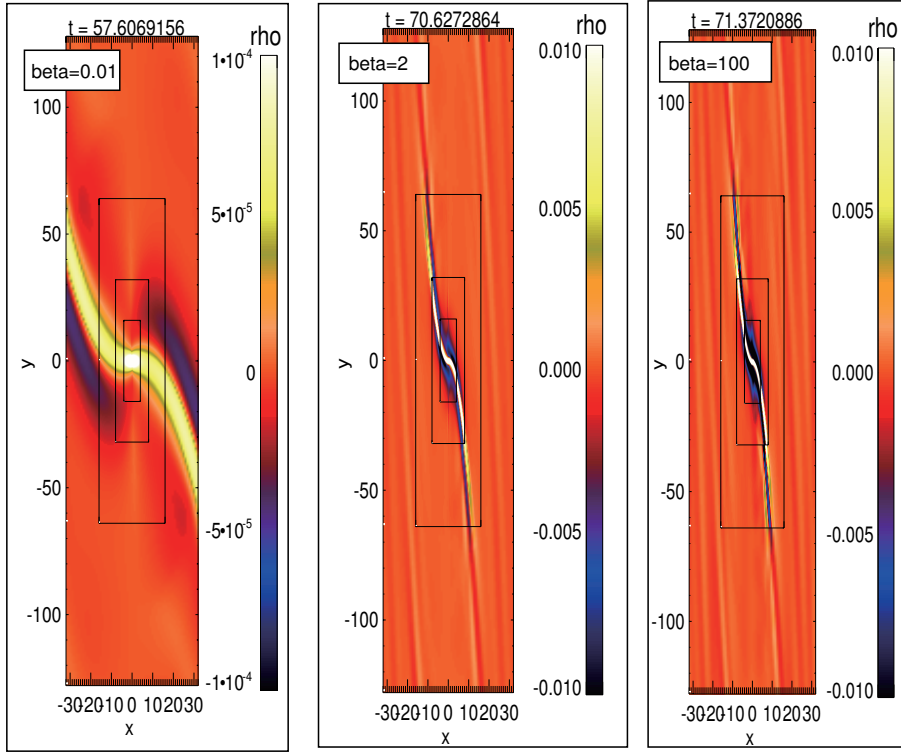
Figure 4.7: Density profile obtained by the two-dimensional numerical calculation. The pattern of density perturbation $\delta\rho/\rho_0$ is indicated by false color. It is clear that the stronger the magnetic field, the further the point where waves are excited and the smaller the amplitude. Note that color scales are different for different values of β. The x- and y-axes correspond to the axes of shearing-sheet, normalized by the scale height c/Ω_p. The elapsed time t is normalized by the planet's Kepler time Ω_p^{-1}. Four different levels of nested grid are super-imposed.
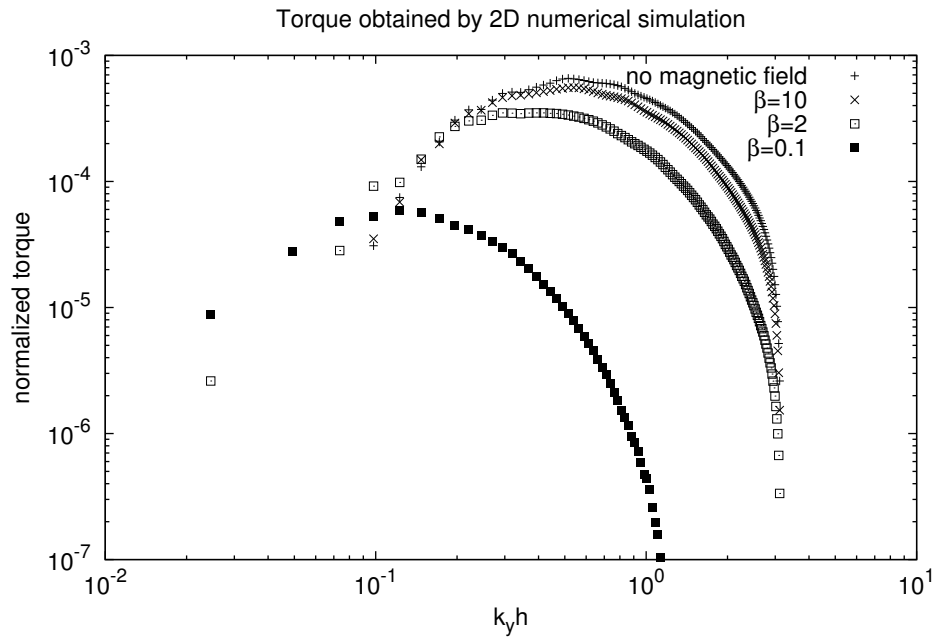
Figure 4.8: The dependence of two-dimensional torque ($k_z = 0$ modes) on the strength of magnetic field obtained by numerical calculations. The models with $\beta = \infty$ (no magnetic field, plus), 10 (cross), 2 (open square), and 0.1 (filled square) are shown. The torque is cut off drastically for models with $\beta < 1$. The horizontal axis denotes $k_y h$ and the vertical axis denotes normalized torque.
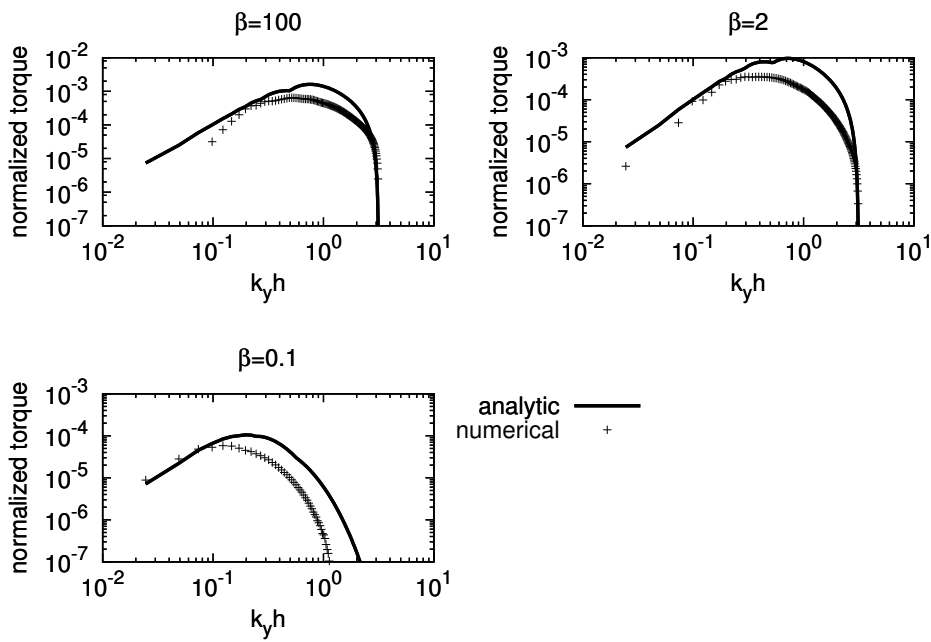
Figure 4.9: Comparison of the torque obtained by the two-dimensional numerical calculation (plus) and the linear analysis (line), the equation (4.95) for $\beta = 100$ (top left), $\beta = 2$ (top right), and $\beta = 0.1$ (bottom). The horizontal axis denotes the azimuthal mode number and the vertical axis denotes normalized torque.
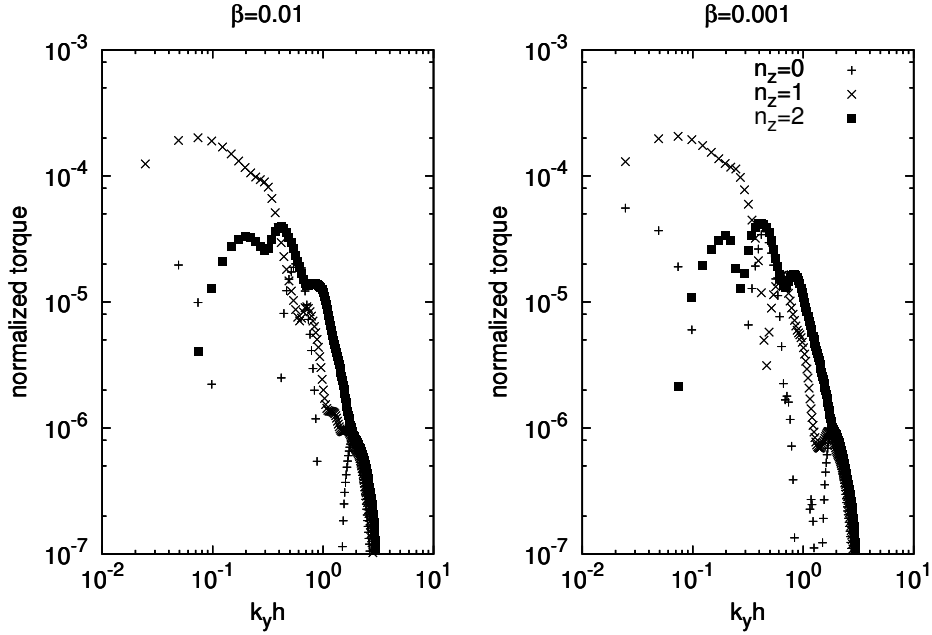
Figure 4.10: k_z-dependence of the torque obtained by three-dimensional numerical calculations. The left panel shows $\beta = 0.01$ and the right $\beta = 0.001$. The horizontal axis denotes the azimuthal mode number and the vertical axis denotes normalized torque. Two-dimensional modes are denoted by plus, three-dimensional modes with $n_z = 1$ by cross, and $n_z = 2$ by filled square. Three-dimensional modes with $n_z = 1$ dominate the two-dimensional modes when the magnetic field is sufficiently strong ($\beta \ll 1$).

We also checked that the numerical calculation and linear analysis are in good agreement for other values of β except for $\beta = 0.001$. For $\beta = 0.001$, since the amplitude of density perturbation is very small, numerical torque is dominated by small noise in the disk.

Three-dimensional Calculation

For $\beta = 0.01$ and $\beta = 0.001$ models of the three-dimensional calculations, we do not observe MRI and steady state is realized. For other parameters, we observe the instability. Since we investigate the stationary pattern, we focus on results in which we do not observe MRI. We show in figure 4.10 the torque that is derived from numerical calculation for $n_z = 0, 1,$ and 2, where n_z is the mode number of z-direction. It is clear that $n_z = 1$ modes overwhelm the two-dimensional modes in these models.
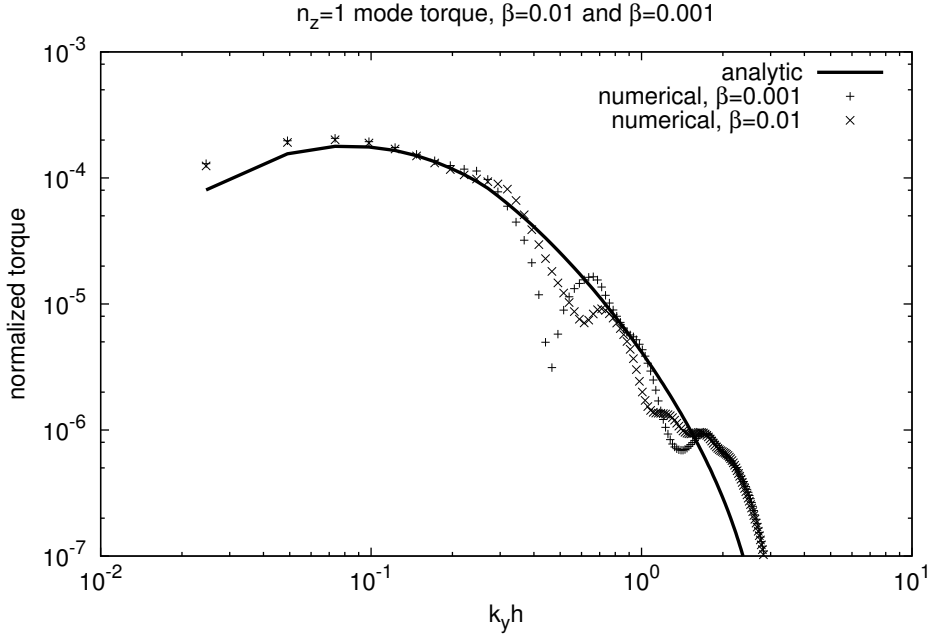
Figure 4.11: The comparison of $n_z = 1$ mode torque between the analytic formula (line), equation (4.95), and three-dimensional numerical calculation for $\beta = 0.001$ (plus) and $\beta = 0.01$ (cross). The horizontal axis shows the azimuthal mode number and the vertical axis shows the normalized torque.

Figure 4.11 compares the torque calculated from the three-dimensional numerical calculations and that calculated from linear analysis of $n_z = 1$ modes, torque formula (4.125). From the derivation of formula (4.125), this expression of the torque is valid when WKB condition $k_y \ll k_z$ and strong magnetic field condition (4.123) are both satisfied. In the present parameter, the WKB condition is more restrictive. Since $k_z h = 2\pi/32 = 0.196$ for $n_z = 1$ mode, we expect that for $k_y h$ greater than this value, equation (4.125) does not give a good approximation for the torque. Nevertheless, the result of the numerical calculation indicates that the equation (4.125) shows a very good agreement even in the modes with $k_y h$ greater than this limit.

We also find that the imaginary part of the Fourier components of density perturbation diverges around MR, as expected from linear analysis. Figure 4.12 shows the profile of the imaginary part of the density perturbation of $\beta = 0.001$ calculation for $(k_y h, k_z h) = (0.498, 0.785)$. The position of magnetic resonance is indicated by an arrow. It is clear that density perturbation diverges at the resonance position and the contribution of the torque mostly comes from this divergence. The torque is localized at the magnetic reso-
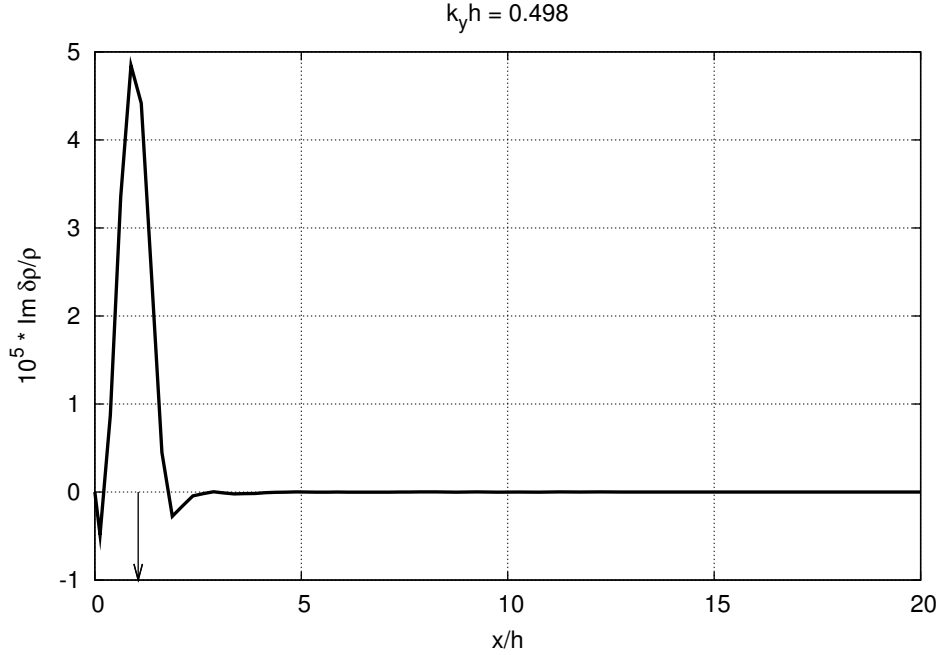
Figure 4.12: The radial profile of $\mathrm{Im}(\delta\rho/\rho_0)$ for the Fourier component $(k_y h, k_z h) = (0.498, 0.785)$ obtained by $\beta = 0.001$ numerical calculation. The profile of the torque on the disk depends on the imaginary part of the density perturbation [see equation (4.61)]. The horizontal axis shows the radial coordinate and the arrow indicate the position of the magnetic resonances calculated by the linear analysis.

nances since waves cannot propagate on the disk, and, therefore, the analytic torque formula (4.125) gives a good approximation of the total torque, even if we consider the regions only in the vicinity of the resonance.

4.2.4   Discussion

The Strength of Three-dimensional Modes in a Thin Disk

Tanaka et al. (2002) [83] has shown that in the unmagnetized disk, three-dimensional modes are subdominant. In contrast, when poloidal magnetic field is exerted on the disk, it is indicated that three-dimensional modes can dominate the torque when the magnetic field is sufficiently strong. In this section, we briefly discuss the critical value of β at which $k_z \neq 0$ modes dominate the total torque in a thin magnetized disk according to the results of linear analysis. By "thin disk", we refer to the disk with small aspect

ratio, smaller than that we have used in the numerical calculation, but not two-dimensional.

We calculate the torque for $n_z = 0$ modes by (4.95) and $n_z = 1$ modes by (4.125). The Fourier transformation of the planet's gravitational potential is done numerically with the box size $L_x = 32h, L_y = 128h, L_z/2 = 2h$ and the spatial resolution $0.125h$. We have checked that $n_z = 2$ modes are smaller than $n_z = 1$ modes. Figure 4.14 shows the torque for $\beta = 0.01$, 2, and 100. The vertical wavenumber of $n_z = 1$ modes is $k_z h = 1.57$, and WKB approximation is valid for $k_y h$ less than this value. For thin disk case, it is indicated, just as thick disk case, that two-dimensional modes are dominant for a weak magnetic field, while three-dimensional modes are important for a strong magnetic field case. We have investigated other values of β and it is indicated that for the disk with $\beta \lesssim 0.1$, three-dimensional modes are more important than two-dimensional modes.

Since three-dimensional torque formula (4.125) is valid only in the strong magnetic field limit, it is not possible to extrapolate this to the case with $\beta \sim 1$. However, since the torque formula for two-dimensional modes (4.95) does not have any restriction, we can safely conclude that $k_z = 0$ modes are always suppressed for strong magnetic field. Therefore, qualitatively, we expect that two-dimensional modes are suppressed for $\beta \lesssim 1$.

Differential Torque

For an unmagnetized disk, it is known that the outer torque that is exerted by the disk outside the planet wins over the inner torque exerted by the disk inside, when the disk gas density is larger in the inner disk than the outer [91]. This is the result of the competition of two effects. On one hand, since the inner density is larger than the outer, the inner torque becomes larger than the outer. On the other hand, the effect called pressure buffer enhances the outer torque. Considering the background disk structure, gas is slightly sub-Keplerian resulting from the outward pressure gradient. Since the planet is in Keplerian rotation, the corotation point locates slightly inside the planet, which makes the outer Lindblad resonance slightly closer to the planet. Calculating the difference of these two competing effects, the outer torque is larger than the inner torque.

Let us now qualitatively discuss the differential torque in the disk with poloidal magnetic field. First, we consider the two-dimensional mode when magnetic field exerted on the disk inside the planet's orbit is larger than the outside. In the case without variation in density and temperature, the mild cutoff of the torque by magnetic field makes the outer torque stronger. If the disk has radially decreasing magnetic pressure distribution, the planet

locates slightly outside the corotation point since outward magnetic pressure is exerted on the gas. This also enhances the outer torque, since the outer effective Lindblad resonance locates closer to the planet. The outer torque is, therefore, expected to be stronger because of these two effects, in contrast to the toroidal magnetic field case of Terquem (2003) [86] where the inner torque is stronger. This might indicate that the differential torque may be very sensitive to the configuration of magnetic field near the planet.

We now turn to the magnetic resonances of $k_z \neq 0$ modes, effective for low β. Since the formula (4.125) is for the limiting case of $\beta \to 0$, the torque does not depend on the magnetic field strength. We shall propose a simple torque formula for MR which generalizes equation (4.125) and discuss the effect of magnetic field. Firstly, we note that the relation between f and $\delta\rho/\rho_0$ is given by

$$\frac{\delta\rho}{\rho_0} = \frac{1}{(c^2 + v_A^2)\sigma^2 - c^2 v_A^2 k_z^2} \left[\sigma^2 f - (\sigma^2 - v_A^2 k_z^2)\psi_p\right]. \qquad (4.130)$$

Since f in the right hand side can be neglected when $\beta = 0$, we expect this term can be neglected even in $\beta \neq 0$, provided that β is sufficiently small. This equation also indicates that there is a δ-function-like divergence at MR. Neglecting the term with f, we obtain the following torque formula at MR for low β,

$$T_{\mathrm{MR,mod}} = \frac{2\pi}{3} L_y L_z \frac{\rho_0 r_p k_z}{\Omega_p c(1+\beta)^{3/2}} \psi_{p,\mathrm{MR}}^2, \qquad (4.131)$$

where the value of gravitational potential is evaluated at MR. The smaller the magnetic field strength is, the closer towards the planet the MR position locates, which makes the gravitational potential at MR, $\psi_{\mathrm{p,MR}}$, stronger. However, the coefficient, $(1+\beta)^{-3/2}$, becomes smaller, which makes the evaluation complicated. Using the parameters with three-dimensional torque calculation, we evaluate the Fourier transform of the gravitational potential and calculate the torque. Figure 4.13 shows the torque calculated from the modified formula (4.131) for $\beta = 0.001$, 0.01, and 0.1. It is indicated that MR torque becomes smaller for weaker magnetic field strength. Therefore, we expect that when the inner magnetic field is stronger than the outer magnetic field and the field strength is high enough for $k_z \neq 0$ modes to be dominant, the inner torque wins over outer torque, in analogous to the results of the analysis of toroidal field by Terquem (2003) [86].

When magnetic field is very strong, equation (4.131) indicates that the value of the torque is not sensitive to the strength of the field, and the differential torque can be very small. We consider, then, the effect of the gradient of sound speed, which changes the location of the resonance even in
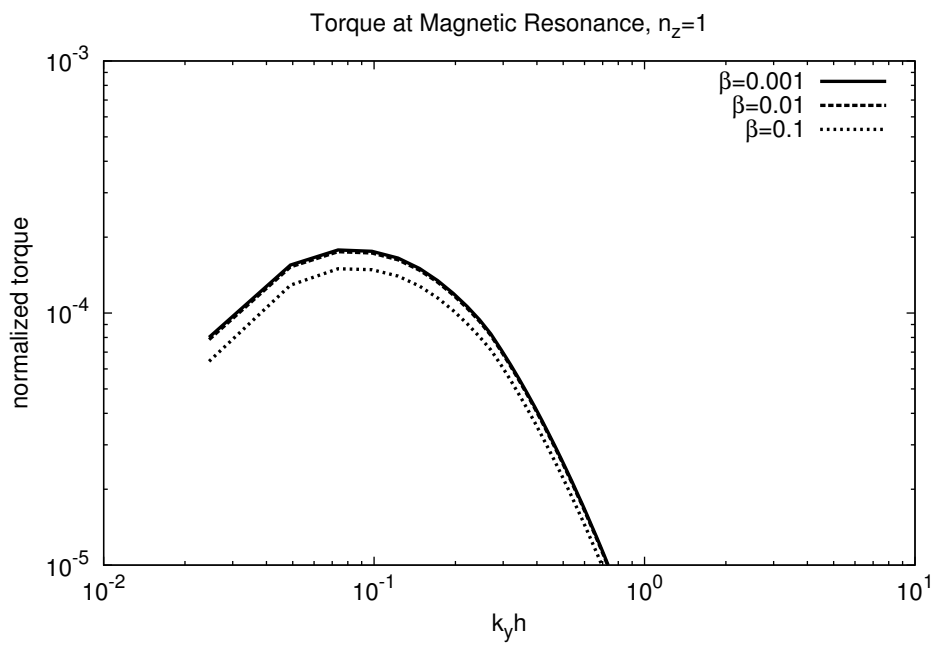
Figure 4.13: Torque at the magnetic resonance obtained by equation (4.131). Magnetic field strength corresponds to $\beta = 0.001$ (solid line), $\beta = 0.01$ (dashed line), and $\beta = 0.1$ (dotted line). The horizontal axis denotes azimuthal mode number and the vertical axis denotes normalized torque.

$\beta \to 0$ limit. Let us consider the disk with higher sound speed inside. The outer MR, which nearly degenerates with VR, is closer to the planet, giving a larger value of gravitational potential. The coefficient of the gravitational potential in equation (4.125) is inversely proportional to the sound speed because $L_z k_z$ is the mode number of the z-direction that is indifferent to the value of c. Therefore, the coefficient is smaller for the inner MR than the outer MR. The outer torque is expected to be stronger than the inner torque when magnetic field is very strong and when there is a negative gradient of the sound speed.

The qualitative dependence on magnetic field of the differential torque for laminar modes may be summarized as follows. Consider the case where inner magnetic field is stronger than the outer. When magnetic field strength is weak and two-dimensional modes are dominant, the outer torque is more enhanced and the migration is inward. When magnetic field is strong enough for three-dimensional modes to be dominant, the migration can be outward. Note, however, that the rate and directions of migration may depend sensitively on the gradient of the sound speed c. Negative gradient of the sound speed may cause the inward migration for very low β.

It seems difficult to halt the inward migration in a disk with strong poloidal magnetic field, since outward migration may require positive gradient of sound speed. Note, however, that the typical magnitude of one-sided torque is always smaller than the unmagnetized case, as shown in figure 4.14. In the disk with $\beta = 100$, the torque is dominated by two-dimensional modes and its magnitude is approximately 10^{-3} in our normalization, while in $\beta = 0.01$ case, the magnitude is smaller by about two orders of magnitude. Therefore, the strong magnetization of disk is expected to slow down the migration. Actually this outcome is analogous to the effect of increasing gas temperature, and hence, thermal pressure and sound speed in the disk without magnetic field.

4.3   Comparison between Toroidal and Poloidal

In this chapter, we have shown the analyses of disk-planet interaction when the disk is threaded by toroidal or poloidal magnetic field. We now make a qualitative discussion by comparing the effect of magnetic resonances of purely toroidal and that of purely poloidal case.

In the case of toroidal magnetic field, there is a magnetic resonance in two-dimensional modes too. In the strong field limit, the position of the

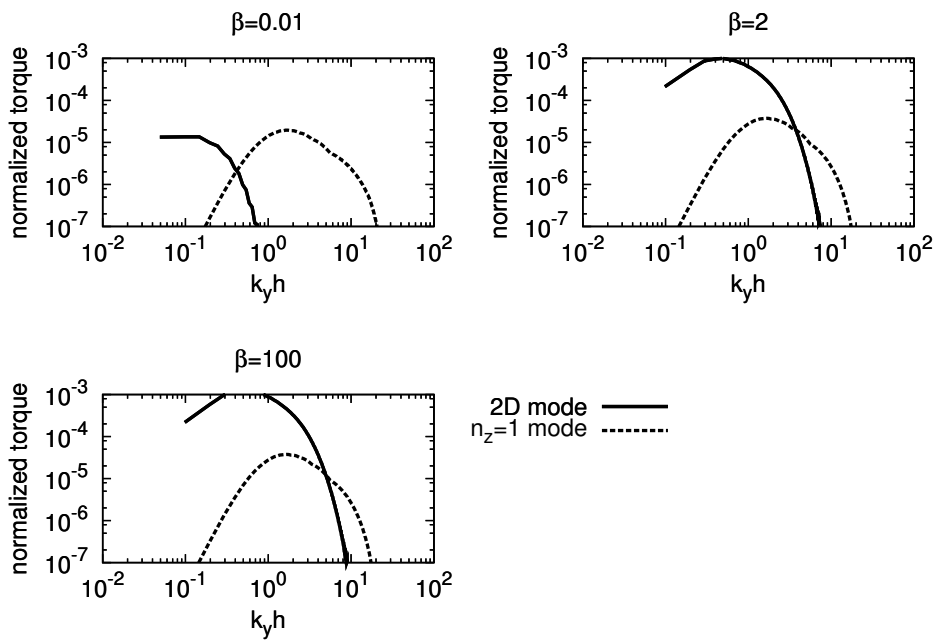Figure 4.14: Comparison between two-dimensional torque formula (4.95) and three-dimensional formula (4.125) for thin disk with $\beta = 0.01$ (top left), $\beta = 2$ (top right), and $\beta = 100$ (bottom). Two-dimensional torque is denoted by the solid line and three-dimensional torque is denoted by the dashed line. The horizontal axis denotes azimuthal mode number and the vertical axis denotes normalized torque.

magnetic resonance is given by

$$x_{\text{MR,toroidal}} = \frac{2}{3}H.$$

$$\text{(4.132)}$$

Since the magnetic resonance in poloidal case is located at

$$x_{\text{MR,poloidal}} = \frac{2}{3}\frac{k_z}{k_y}H,$$

$$\text{(4.133)}$$

and in a thin disk, modes $k_z \gg k_y$ are important, the magnetic resonance of a toroidal field is closer to the planet than the toroidal case. We also note that the Fourier components of three-dimensional modes of gravitational potential are much smaller than the two-dimensional modes, as shown by Tanaka et al (2002) [83]. Therefore, in a standard case of a planet on a circular orbit embedded in a disk midplane, we expect that when the net magnetic field is dominated by toroidal components, the effect of poloidal magnetic field is small compared to that of a toroidal field. A possible exception is provided by a large inclination of planet's orbit. In this case, the gravitational potential of planet has a large z-component (three-dimensional modes), and thus, the poloidal field would be important. Note, however, that we need a new set of analyses for the case of a planet with inclined orbit (for unmagnetized disks, see Tanaka & Ward 2004 [84]).

Chapter 5

Effects of Viscosity

In the previous chapter, we have shown that the properties of disk-planet interaction is qualitatively different from standard, non-magnetized case if MHD effects are considered . In this chapter, we investigate how the characteristics of disk-planet interaction is altered by the effects of viscosity. Although there has been a number of investigations on the disk-planet interaction in a viscous disk (for example, Masset 2001, 2002 [57] [58] or Paardekooper and Papaloizou 2009 [69] for corotation torque, D'Angelo et al. 2002, 2003 [18] [19] for high resolution numerical study), there has not yet been a study of wide range in the viscous coefficient that requires an analysis on the detailed density structure in the vicinity of the planet. In this chapter, as a first step for the complete investigation, we show results of linear calculation in a local, shearing-sheet analysis.

We find that as we increase the values of viscous coefficient α, one-sided torque stays unchanged until $\alpha \lesssim 0.01$, then increases until $\alpha \sim 1$, and finally decreases. The torque can be factor of two larger than inviscid case when $\alpha = 0.1$, and more importantly, the enhancement of the torque is a result of the modified density structure in the vicinity of the planet, which has not yet been investigated in detail. Our results indicate that the physical mechanisms of the disk-planet interaction in a viscous disk may depend on the detailed density structure around the planet.

We use time-dependent methods to calculate the disk response against the planet potential. Although this method has not been widely used so far, this is useful in investigating the effects of various physical processes on disk-planet interaction. We calculate the non-axisymmetric density structure around the planet and investigate how the resulting torque is altered by the effect of shear viscosity. We have studied wide range of the parameters of viscous coefficient and calculate the density structure with high resolution. We find that the density structure in the vicinity of the planet is altered

in a viscous disk, with viscous coefficient of ~ 0.1 in terms of α (standard α parameter, see equation (5.27) for definition), which may be realized as a result of the turbulence induced by magneto-rotational instability (MRI, Balbus and Hawley 1991 [6], Sano et al. 2004 [74]).

5.1   Methods of Calculation

We consider isothermal Navier-Stokes equations with one planet using shearing-sheet approximation.

$$\frac{\partial \rho}{\partial t} + \nabla \cdot (\rho \boldsymbol{v}) = 0 \tag{5.1}$$

$$\begin{aligned}
\frac{\partial \boldsymbol{v}}{\partial t} &+ \boldsymbol{v} \cdot \nabla \boldsymbol{v} + 2\Omega_{\mathrm{p}} \boldsymbol{e}_z \times \boldsymbol{v} \\
&= -\frac{c^2}{\rho} \nabla \rho + 3\Omega_{\mathrm{p}}^2 x \boldsymbol{e}_x + \nu \nabla^2 \boldsymbol{v} + \frac{1}{3}\nu \nabla (\nabla \cdot \boldsymbol{v}) - \nabla \psi_{\mathrm{p}}
\end{aligned} \tag{5.2}$$

where ρ is density, $\boldsymbol{v}$ is velocity, Ω_{p} is the Kepler angular velocity of the planet, ψ_{p} is the gravitational potential of the planet, ν is shear viscosity. We assume the planet is located at the origin and stationary with respect to this coordinate system, i.e.,

$$\psi_{\mathrm{p}} = \psi_{\mathrm{p}}(x, y, z), \tag{5.3}$$

where ψ_{p} does not depend on time. In this chapter, we neglect bulk viscosity for simplicity. We also neglect vertical stratification and assume that the background density without a planet is homogeneous. This gives an uncertainty in the box size in the z-direction, which will be discussed later in this section. We also neglect the effect of global gas pressure gradient exerted on the background disk and assume that the background gas is rotating at Kepler velocity.

The unperturbed state without a planet is given by

$$\rho = \rho_0 = \mathrm{const} \tag{5.4}$$

$$\boldsymbol{v}_0 = -\frac{3}{2}\Omega_{\mathrm{p}} x \boldsymbol{e}_y. \tag{5.5}$$

In the presence of viscosity, if we perform a global analysis, there is a mass accretion onto the central star in general. However, in the shearing-sheet approximation, where linear background shear is assumed, this effect is not taken into account. We expect that the density structure only in the vicinity

of the planet can be well approximated even if we neglect the global mass accretion.

We consider linear perturbation. All the perturbation quantities are denoted with δ, e.g., $\delta\rho$ for density perturbation. Perturbation equations are given by

$$\left(\frac{\partial}{\partial t} - \frac{3}{2}\Omega_{\mathrm{p}}x\frac{\partial}{\partial y}\right)\frac{\delta\rho}{\rho_0} + \nabla \cdot \delta\boldsymbol{v} = 0 \tag{5.6}$$

$$\left(\frac{\partial}{\partial t} - \frac{3}{2}\Omega_{\mathrm{p}}x\frac{\partial}{\partial y}\right)\delta\boldsymbol{v} - 2\Omega_{\mathrm{p}}\delta v_y\boldsymbol{e}_x + \frac{1}{2}\Omega_{\mathrm{p}}\delta v_x\boldsymbol{e}_y$$

$$= -c^2\nabla\frac{\delta\rho}{\rho_0} + \nu\nabla^2\delta\boldsymbol{v} + \frac{1}{3}\nu\nabla\left(\nabla \cdot \delta\boldsymbol{v}\right) - \nabla\psi_{\mathrm{p}} \tag{5.7}$$

We solve equations (5.6) and (5.7) to obtain a steady state solution and calculate torque exerted on one side (either $x > 0$ or $x < 0$) of the disk by the planet. The torque exerted on the planet is obtained as a backreaction of this torque. Since we use shearing-sheet approximation, torque exerted from each side of the planet is the same in magnitude and opposite in sign. Although we do not obtain a net torque, it is still possible to investigate how the disk structure is affected by the viscosity and qualitatively predict how the disk and planet interact.

In order to obtain a steady state solution, we solve linear perturbation equations (5.6) and (5.7) using Fourier transform methods given by Goodman and Rafikov (2001) [39]. We transform the equations into the shearing coordinate (t', x', y', z') defined by

$$t' = t \tag{5.8}$$

$$x' = x \tag{5.9}$$

$$y' = y + \frac{3}{2}\Omega_{\mathrm{p}}xt \tag{5.10}$$

$$z' = z. \tag{5.11}$$

In this coordinate system, temporal and spatial derivatives are given by

$$\frac{\partial}{\partial t} = \frac{\partial}{\partial t'} + \frac{3}{2}\Omega_{\mathrm{p}}x'\frac{\partial}{\partial y'}, \tag{5.12}$$

$$\frac{\partial}{\partial x} = \frac{\partial}{\partial x'} + \frac{3}{2}\Omega_{\mathrm{p}}t'\frac{\partial}{\partial y'}, \tag{5.13}$$

$$\frac{\partial}{\partial y} = \frac{\partial}{\partial y'}, \ \frac{\partial}{\partial z} = \frac{\partial}{\partial z'}. \tag{5.14}$$

Then, perturbation equations become

$$\frac{\partial}{\partial t'}\frac{\delta\rho}{\rho_0} + \nabla \cdot \delta\boldsymbol{v} = 0 \tag{5.15}$$

$$\frac{\partial}{\partial t'}\delta\boldsymbol{v} - 2\Omega_\mathrm{p}\delta v_y\boldsymbol{e}_x + \frac{1}{2}\Omega_\mathrm{p}\delta v_x\boldsymbol{e}_y$$
$$= -c^2\nabla\frac{\delta\rho}{\rho_0} + \nu\nabla^2\delta\boldsymbol{v} + \frac{1}{3}\nu\nabla\left(\nabla\cdot\delta\boldsymbol{v}\right) - \nabla\psi_\mathrm{p}, \tag{5.16}$$

where the spatial derivatives in ∇ are given by equations (5.13) and (5.14).

The coefficients of equation (5.15) and (5.16) are now independent of (x', y', z'). Therefore, if we Fourier transform in spatial directions, we obtain a set of ordinary differential equations decoupled for each (k'_x, k'_y, k'_z) mode (Goldreich and Lynden-Bell 1965 [37]),

$$\delta f(t', x', y', z') = \sum \delta f(t', k'_x, k'_y, k'_z) \exp\left[i(k'_x x' + k'_y y' + k'_z z')\right]. \tag{5.17}$$

The relationship of wavenumber in (x, y, z)-coordinate and (x', y', z')-coordinate is given by

$$k_x(t) = k'_x + \frac{3}{2}\Omega_\mathrm{p}k_y t. \tag{5.18}$$

$$k_y = k'_y, \ k_z = k'_z \tag{5.19}$$

Equation (5.18) indicates that the value of radial wavenumber in (x, y, z)-coordinate evolves with time owing to the background shear. The value of radial wavenumber in shearing coordinate k'_x gives the initial value of radial wavenumber in (x, y, z)-plane. Equations of continuity (5.6) and motion (5.7) are now

$$\frac{d}{dt}\frac{\delta\rho}{\rho_0} + ik_x(t)\delta v_x + ik_y\delta v_y + ik_z\delta v_z = 0, \tag{5.20}$$

$$\frac{d}{dt}\delta v_x - 2\Omega_\mathrm{p}\delta v_y = -c^2 ik_x(t)\frac{\delta\rho}{\rho_0} - \nu(k_x(t)^2 + k_y^2 + k_z^2)\delta v_x$$
$$-\frac{1}{3}\nu k_x(t)(k_x(t)\delta v_x + k_y\delta v_y + k_z\delta v_z) - ik_x(t)\psi_\mathrm{p}, \tag{5.21}$$

$$\frac{d}{dt}\delta v_y + \frac{1}{2}\Omega_\mathrm{p}\delta v_x = -c^2 ik_y\frac{\delta\rho}{\rho_0} - \nu(k_x(t)^2 + k_y^2 + k_z^2)\delta v_y$$
$$-\frac{1}{3}\nu k_y(k_x(t)\delta v_x + k_y\delta v_y + k_z\delta v_z) - ik_y\psi_\mathrm{p}, \tag{5.22}$$

and

$$\frac{d}{dt}\delta v_z = -c^2 i k_z \frac{\delta \rho}{\rho_0} - \nu(k_x(t)^2 + k_y^2 + k_z^2)\delta v_y$$
$$-\frac{1}{3}\nu k_y(k_x(t)\delta v_x + k_y \delta v_y + k_z \delta v_z) - i k_z \psi_{\rm p}. \qquad (5.23)$$

In equations (5.20)-(5.23), we write all the terms in (t, x, y, z)-coordinate. These equations describe the excitation and evolution of density wave by the source $\psi_{\rm p}$. The source of the density wave becomes zero when wavenumber (k_x', k_y', k_z') is large.

As an initial condition, we assume that there is no perturbation: $\delta\rho(t = 0) = \delta \boldsymbol{v}(t = 0) = 0$, and k_x' is taken to be sufficiently large in absolute magnitude and negative (positive) in sign for positive (negative) k_y. If we use spatial resolution of x-direction Δx, we should take $k_x' = \mp 2\pi/\Delta x$, where upper (lower) sign is used for positive (negative) k_y. As a result of time evolution, $k_x(t)$ increases (decreases) for each positive (negative) k_y mode. When $k_x(t)$ reaches $\pm 2\pi/\Delta x$, where upper (lower) sign is for positive (negative) k_y modes, we obtain a steady state profile of perturbation quantities in Fourier space for non-axisymmetric ($k_y \neq 0$) modes. [1] The Fourier amplitude of each k_x mode in steady state is given by the time evolution data through equation (5.18). The profile of physical quantities in Fourier space is then inverse Fourier transformed to obtain values in real space. Since we are interested in torque, we do not calculate axisymmetric modes ($k_y = 0$).

The standard procedure to obtain steady state solution is as follows. Firstly, stationary solution in the frame corotating with the planet is assumed: $\partial/\partial t = 0$. Then, Fourier transformation in the y- and z-directions is performed to obtain the ordinary differential equations in the x-direction. Finally, these ordinary differential equations are solved by imposing outgoing boundary condition, or equivalently the boundary condition that admits only trailing wave, see e.g., Goldreich and Tremaine (1979) [38], Korycansky and Pollack (1993) [48], or Tanaka et al. (2002) [83].

In the presence of viscosity, this method introduces higher order derivative with respect to x, since viscous terms include the second order derivative in

---

[1]The reason why we obtain a steady state as a result of time evolution is as follows. Let us assume that if $|k_x| > K_c$, the source $\psi_{\rm p}$ is so small that we can approximate it to be zero. The Fourier amplitude of the specific k_{x0} mode in (t, x, y, z)-coordinate at time $t = t_0$ is given by the solution at $t = t_0$ with $k_x' = k_{x0} - (3/2)\Omega_{\rm p} k_y t_0$ mode. Therefore, the absolute magnitude of k_x' that contributes to the Fourier amplitude of fixed k_{x0} becomes large as time t_0 increases. If the absolute magnitude of k_x' is larger than K_c, there is no wave excitation for this mode until $|k_x(t)|$ becomes smaller than K_c. Therefore, when $|k_x'| > K_c$, the contribution to the k_{x0} mode is always the same regardless of t_0.

the radial direction. The resulting ordinary differential equations are higher order in the x-derivative than in inviscid cases. The terms with the highest order derivative comes from viscous terms and their coefficients are viscous coefficient ν. In this case, it is difficult to take natural $\nu \to 0$ limit, since equations become singular in this limit.

Time-dependent approach overcomes this difficulty since the order of time derivative is not affected by viscous terms since they do not include any time derivative. It is also easy to take $\nu \to 0$ limit since viscous terms simply drop from equations (5.21)-(5.23) in this limit and they do not introduce any singularity.

In our formulation using the Fourier transform in sheared coordinate, the outgoing boundary condition in the radial direction that is assumed in the standard stationary formulation is not exactly satisfied, since Fourier transform introduces the periodic boundary condition in the sheared coordinate. However, we find that outgoing boundary condition is effectively satisfied if we vary the box size in the x-direction depending on the modes specified by k_y and k_z. Details of our methods are given below.

We also note that if we assume an initial condition with non-zero perturbation, additional homogeneous wave is introduced. This wave has both leading ($k_x k_y < 0$) and trailing ($k_x k_y > 0$) components and the resulting solution is simply the superposition of the specific solution of Equations (5.20)-(5.23) assuming zero initial condition and homogeneous ($\psi_{\mathrm{p}} = 0$) solution assuming the specified initial condition. The solution with non-zero initial condition is irrelevant in the present problem because we consider the perturbation that is induced by the gravitational perturbation by the planet.

We write the box size in (x, y, z)-directions by (L_x, L_y, L_z) and the coordinate system extends $-L_x/2 < x < L_x/2$ and so forth for other directions. Practically, our procedure to obtain the stationary, non-axisymmetric structure of the disk is summarized as follows.

1. We take $k_x' = \mp 2\pi/\Delta x$ for positive (negative) k_y modes.

2. Equations (5.20)-(5.23) are solved with initial condition $\delta\rho(t = 0) = \delta\boldsymbol{v}(t = 0) = 0$.

3. Resulting solutions in (k_x, k_y, k_z) space are inverse Fourier transformed to real space.

In steps 2 and 3, there are some points we need to take care. In calculating the Fourier modes, we have varied the mesh number in k_x directions, which corresponds to the step size of time, in such a way that all the oscillations are well resolved for each (k_y, k_z) mode. The mesh number in k_x direction

becomes as much as 10^6 for small k_y. We perform inverse Fourier transform in k_x direction using the increased number of mesh in k_x direction. This procedure effectively makes the box size of x-direction longer for a specific k_y mode, and the data corresponding to necessary x, which is $-L_x/2 < x < L_x/2$, is then interpolated from the resulting profile in (x, k_y, k_z) space. This data is then used to perform inverse Fourier transform in (k_y, k_z) directions. In this way, it is possible to avoid aliasing effect in x-direction and outgoing boundary condition in the steady state solution is effectively satisfied. We do not use any window function, which has been incorporated by Goodman and Rafikov (2001) [39], in Fourier transform. We have checked that the resulting torque is not affected by the window function in the absence of viscosity. Also, since window function introduces additional artificial dissipation, this affects our results with viscosity.

Once we have obtained the profiles of perturbation quantities in real space, we can calculate the one-sided torque exerted on $x > 0$ part of the disk by the planet by

$$T = -r_\mathrm{p} \int_0^{L_x} \int_{-L_y/2}^{L_y/2} \int_{-L_z/2}^{L_z/2} dx\,dy\,dz\, \delta\rho(x, y, z) \frac{\partial \psi_\mathrm{p}}{\partial y}, \qquad (5.24)$$

where r_p is the semi-major axis of the planet, and the torque exerted on the planet is obtained as backreaction. For later convenience, we define "torque distribution" $T(x, y, z)$ that is simply the torque exerted on the fluid element located at (x, y, z),

$$T(x, y, z) = -r_\mathrm{p} \delta\rho(x, y, z) \frac{\partial \psi_\mathrm{p}}{\partial y} \qquad (5.25)$$

and "torque density" that is the torque exerted on an annulus of the disk at x,

$$T(x) = -r_\mathrm{p} \int_{-L_y/2}^{L_y/2} \int_{-L_z/2}^{L_z/2} dz\,dy\, \delta\rho(x, y, z) \frac{\partial \psi_\mathrm{p}}{\partial y} \qquad (5.26)$$

We normalize equations using c, Ω_p, and ρ_0 so that the homogeneous equations ($\psi_\mathrm{p}{=}0$) contain only one dimensionless variable α that is defined by

$$\alpha = \frac{\nu}{cH}, \qquad (5.27)$$

where $H = c/\Omega_\mathrm{p}$ is the scale height of the disk. Since we consider the linear perturbation analysis, the amplitude of the perturbation is proportional to the normalized planet mass:

$$\mu = GM_\mathrm{p}/Hc^2. \qquad (5.28)$$

We show the results with $\mu = 1$ in subsequent sections.

We use the fifth order Runge-Kutta method to solve time evolution and FFT routine given by Press et al. (1996) [31] to perform Fourier transform. We use box size of $L_x = 10H$ and $L_y = 40H$, and the grid number in x- and y-directions $(N_x, N_y) = (512, 512)$.

We need to be careful about the treatment in the x-direction in three-dimensional calculations. We now discuss how 2D and 3D calculations differ from each other and determine the relevant box size in the z-direction with which the effect of vertical stratification is effectively taken into account.

We compare 2D calculation and 2D mode of 3D calculation. By "2D calculation", we mean the gravitational potential of the planet is given by

$$\psi_{\mathrm{p,2D}}(x, y) = -\frac{GM_{\mathrm{p}}}{\sqrt{x^2 + y^2 + \epsilon_{\mathrm{2D}}^2}}, \tag{5.29}$$

where ϵ_{2D} denotes the softening length of 2D calculation, which is usually incorporated in most of 2D work. By "2D mode of 3D calculation", we mean that the analysis is restricted to $k_z = 0$ mode of 3D calculation. Three-dimensional potential is given by

$$\psi_{\mathrm{p,3D}}(x, y, z) = -\frac{GM_{\mathrm{p}}}{\sqrt{x^2 + y^2 + z^2 + \epsilon_{\mathrm{3D}}^2}}. \tag{5.30}$$

Therefore, gravitational potential for "2D mode of 3D calculation" is given by

$$
\begin{aligned}
\psi_{\mathrm{p,3D}}(x, y) &= -\frac{1}{L_z} \int_{-L_z/2}^{L_z/2} dz \frac{GM_{\mathrm{p}}}{\sqrt{x^2 + y^2 + z^2 + \epsilon_{\mathrm{3D}}^2}} \\
&= -\frac{GM_{\mathrm{p}}}{L_z} \log \left| \frac{x^2 + y^2 + \epsilon_{\mathrm{3D}}^2 + L_z^2/2 + L_z\sqrt{L_z^2/4 + x^2 + y^2 + \epsilon_{\mathrm{3D}}^2}}{x^2 + y^2 + \epsilon_{\mathrm{3D}}^2} \right|,
\end{aligned}
\tag{5.31}
$$

where we denote softening length in 3D calculation by ϵ_{3D}. We note that $\psi_{\mathrm{p,2D}}$ and $\psi_{\mathrm{p,3D}}$ coincides if $x^2 + y^2 + \epsilon^2 \gg L_z$, but they differ if $x^2 + y^2 + \epsilon^2 \ll L_z$, since in this case, 3D potential behaves as $\psi_{\mathrm{p,3D}} \sim \log r$ while 2D potential behaves as $\psi_{\mathrm{p,2D}} \sim 1/r$, where $r^2 = x^2 + y^2 + \epsilon^2$. Vertical averaging makes the potential weaker in the vicinity of the planet, thereby producing small perturbation in 2D mode of 3D calculation. Figure 5.1 shows the torque obtained by 2D inviscid ($\nu = 0$) calculation using $\psi_{\mathrm{p,2D}}$ and $\psi_{\mathrm{p,3D}}$ with various L_z. We note that in producing Figure 5.1, one-sided torque is calculated according to equation (5.24) and the value is normalized by

$$\Gamma_{\mathrm{2D}} = \mu^2 \rho_0 L_z r_{\mathrm{p}} H c^2. \tag{5.32}$$
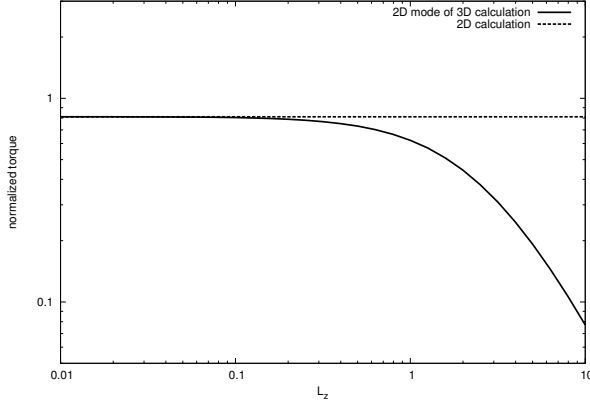
Figure 5.1: Comparison of the torque obtained in 2D calculation and the 2D mode of 3D calculation for various L_z. In 2D calculations (dashed line), we use the gravitational potential given by equation (5.29), while in 2D mode of 3D calculation (solid line), we use the gravitational potential given by equation (5.31). The value of the normalized torque, T/Γ_{2D} is plotted, where Γ_{2D} is defined by equation (5.32).

It is clear that 2D and 3D results coincide if L_z is small, but the 3D result becomes small when L_z is large.

The reasonable value of L_z may be obtained by comparing the results of 2D mode of 3D calculation with calculation in which vertical stratification is taken into account. Tanaka et al. (2002) [83] performed such calculations for an inviscid disk. Their method is to decompose vertical modes in terms of Hermite polynomials, and they have found that the vertically averaged 2D mode gives most of the contribution to the resulting torque. Their 2D mode of the potential, $\psi_{p,TTW}$, is given by

$$
\begin{aligned}
\psi_{p,TTW} \quad &= -\frac{1}{\sqrt{2\pi}H} \int_{-\infty}^{\infty} dz \frac{GM_p}{\sqrt{x^2 + y^2 + z^2 + \epsilon_{3D}^2}} e^{-z^2/2H^2} \qquad (5.33)\\
&= -\frac{GM_p}{\sqrt{2\pi}H} \exp\left[(x^2 + y^2 + \epsilon_{3D}^2)/4\right] K_0\left[\left(x^2 + y^2 + \epsilon_{3D}^2\right)/4\right],
\end{aligned}
$$

where $K_0(x)$ is the modified Bessel function of the zeroth order. Fitting equation (5.31) with equation (5.34), we find $L_z = 2.7H$ gives a reasonable agreement, see Figure 5.2. Zeroth order of modified local approximation incorporated by Tanaka et al. (2002) [83] coincides with the shearing-sheet approximation, and we have exactly the same homogeneous equations with them for 2D ($k_z = 0$) mode if we assume $\partial/\partial t = 0$. As is clear from Figure 5.1, 2D mode in 3D calculation gives smaller amount of torque than the
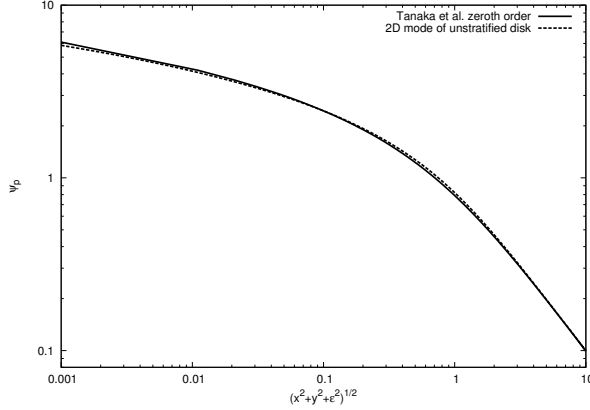
Figure 5.2: Comparison of the 2D mode of the potential used by Tanaka et al. (2002) [83] given by equation (5.34) (solid line) and the $k_z = 0$ mode of the potential given by (5.31) with $L_z = 2.7H$ (dashed line).

calculation using 2D potential given by equation (5.29). This explains why Tanaka et al. (2002) [83] has obtained slightly smaller amount of torque compared to 2D results. We have also checked that setting $L_z = 2.7H$, our results of one-sided torque agree with those determined by using Tanaka et al. (2002) [83] methods within an error of 3%. [2]

We use $L_z = 2.5H$ and the mesh number in z-direction is taken to be 128. In total, we have performed calculation with $(L_x, L_y, L_z) = (10H, 40H, 2.5H)$ with mesh number $(512, 512, 128)$, and the resulting mesh size is $(\Delta x, \Delta y, \Delta z) = (0.02H, 0.08H, 0.02H)$. However, the radial box size is variably extended according to modes in calculation. Effective box size in x-direction is as much as $10^4 H$. We use $\epsilon_{3D} = 10^{-3} H$ for the softening parameter. Our results vary upto 30% for large values of viscosity when smoothing length is varied upto twice the grid resolution. Therefore, our results give at least a qualitative view of how disk-planet interaction is altered by the effects of viscosity. The variation of one-sided torque as a function of smoothing parameter is further discussed in Section 5.2.2.

---

[2]There is another complication regarding the normalization of the torque when comparing the value of the torque obtained by our calculation and that given by Tanaka et al. (2002) [83]. They use surface density to normalize the torque they have obtained. We use normalization given by equation (5.32). Correspondence between the two results is given by reading our $\rho_0 L_z$ to σ_p of Tanaka et al. (2002) [83], and this is how we have obtained the agreement with their calculation.

5.2 Results

In this section, we show our results of density structure and one-sided torque obtained by linear analysis. In this section, the normalization of the torque is given by

$$\Gamma_{3D} = \mu^2 \rho_0 r_{\mathrm{p}} H^2 c^2. \tag{5.34}$$

Note the difference in the normalization from that used in Section 5.1. The results of 2D mode torque given in Section 5.2.1 are different by a factor of $L_z/H = 2.5$ from those given in Figure 5.1. The normalization of torque distribution defined by equation (5.25) is taken to be

$$\frac{T(x, y, z)}{\mu^2 \rho_0 r_{\mathrm{p}} c^2 H^{-1}}, \tag{5.35}$$

and torque density $T(x)$ defined by equation (5.26) is given by

$$\frac{T(x)}{\mu^2 \rho_0 r_{\mathrm{p}} c^2}. \tag{5.36}$$

5.2.1 Calculations Restricted to 2D Mode

We first show the results of calculations restricted to 2D modes ($k_z = 0$). Although this is only an approximation, physics involved is made clear. Figure 5.3 shows the torque obtained for various viscosity parameter α. For small viscous coefficients ($\alpha \lesssim 10^{-2}$), torque is not affected by the viscosity, as discussed by Meyer-Vernet and Sicardy (1987). However, when viscous coefficient is large, it is shown that one-sided torque increases and peaks around $\alpha \sim 1$.

Since viscosity, or any form of dissipation, damps density contrast in general, one may think that Lindblad torque is a decreasing function of viscosity. [3] However, our result shows that one-sided torque peaks at $\alpha \sim 1$. This result originates from two different effects of viscosity. First, viscosity damps spiral density wave, as discussed by Papaloizou and Lin (1984) [71] or Takeuchi et al. (1996) [82]. The second effect of viscosity may be observed by looking at the density structure in the vicinity of the planet. Figure 5.4 shows the contour of density profile of the xy-plane for $\alpha = 10^{-4}$ and $\alpha = 10^{-1}$. It is clear that the oval density profile in the vicinity of the planet is slightly

---

[3]The effect of viscosity on the fluid elements trapped in the horseshoe regions enhances the resulting torque since viscosity keeps the asymmetry of the potential vorticity. This applies corotation torque, see Masset (2001) [57] for detail. In shearing-sheet calculations presented here, however, there is no corotation torque since background values are assumed to be constant.
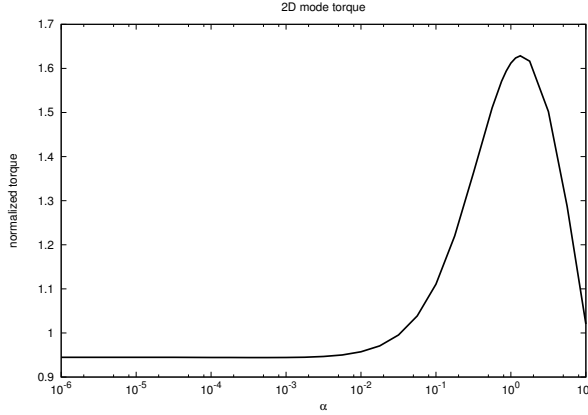
Figure 5.3: Variation of torque as a function of viscous coefficient α as a result of 3D calculation restricted to 2D modes.

tilted for large viscous coefficient, while the spiral density wave is damped. This tilt produces asymmetry of density structure in the y-direction, thereby exerting one-sided torque on the planet.

Figure 5.5 shows the torque density for $\alpha = 10^{-1}$ and $\alpha = 10^{-4}$, respectively. It is clear that the peak of torque density locates slightly closer to the planet for $\alpha = 10^{-1}$ than $\alpha = 10^{-4}$. The main contribution to the torque comes from the flow structure in the vicinity of the planet, which is evident when we consider the asymmetry of the density perturbation between $y > 0$ and $y < 0$ regions. In Figure 5.6, we plot the contour for the sum of torque at $y > 0$ and $y < 0$ region,

$$T(x, y) + T(x, -y), \tag{5.37}$$

as a function of x and $y(> 0)$. This shows the asymmetry of torque distribution in the y-directions. In Figure 5.6, we compare the results for two different values of viscosity, $\alpha = 10^{-4}$ and $\alpha = 10^{-1}$. In the case of $\alpha = 10^{-4}$, the forward-back difference of the torque in the vicinity of the planet almost vanishes since the density perturbation around the planet is symmetric in the y-direction. In the case of $\alpha = 10^{-1}$, however, the most of the contribution to the torque comes from the region very close to the planet since the oval density perturbation structure is tilted in $y < 0$ direction (see also Figure 5.4).

5.2.2   3D Calculation and the Effects of Smoothing Length

In this section, we present the results of 3D calculation. Figure 5.7 shows the one-sided torque as a function of viscosity. The qualitative behavior of
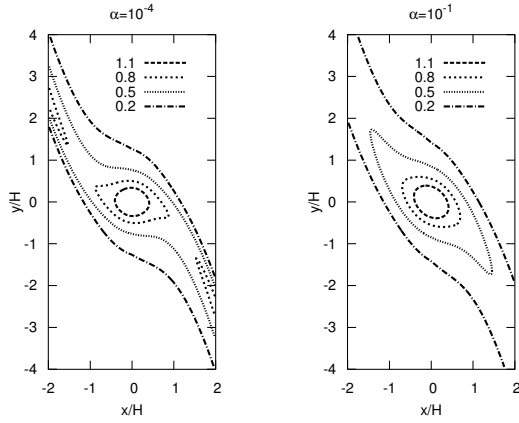
Figure 5.4: Contour plot of the density fluctuation $\delta\rho/\rho_0$ around the planet (located at the origin) for 2D mode of 3D calculation with $L_z = 2.5H$ with $\alpha = 10^{-4}$ (left) and $\alpha = 10^{-1}$ (right). Axisymmetric mode is not included.
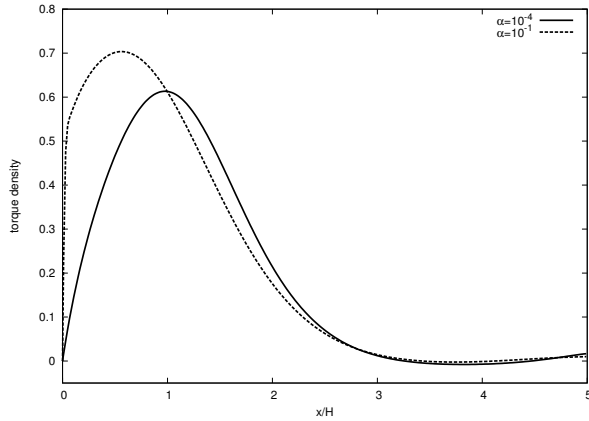

Figure 5.5: Torque density given by equation (5.26) for $\alpha = 10^{-4}$ (solid line) and $\alpha = 10^{-1}$ (dashed line). Values are normalized according to equation (5.36).
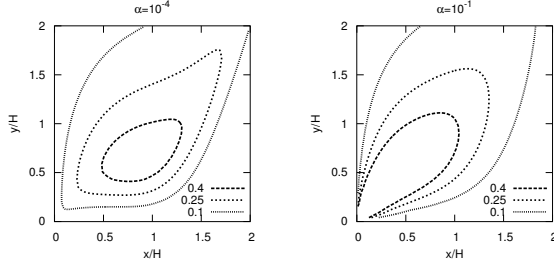
Figure 5.6: Forward-back asymmetry of the torque distribution given by equation (5.37) for $\alpha = 10^{-4}$ and $\alpha = 10^{-1}$.

torque increasing with viscosity is unchanged, but the enhancement of torque becomes large compared to 2D calculation. We fit the data and obtain the following empirical relation

$$\frac{T}{\rho_0 r_{\mathrm{p}} H^2 c^2} = (0.94 + 10\alpha)e^{-1.5\alpha} \tag{5.38}$$

for $\alpha < 0.3$ and $L_z = 2.5H$. We have chosen a form of fitting function in such a way that torque converges to a non-zero value for $\alpha \ll 1$, peaks at $\alpha \sim 1$, and decreases to zero for $\alpha \gg 1$. This fitting formula is in reasonably good agreement with our calculation in this range of viscosity coefficient.

Just as in the calculations restricted to 2D modes, the density structure mainly in the vicinity of the planet contributes to the one-sided torque if large values of viscosity is assumed. Figure 5.8 shows the torque density profile obtained for different viscosity coefficients. The more viscous is the disk, the closer to the planet is the location of the dominant contribution to the torque. Figure 5.9 compares the density structure in the yz-plane at $x = 0.068H$ for calculations with $\alpha = 10^{-4}$ and $\alpha = 10^{-1}$. The asymmetry in the y-direction in strongly perturbed region is present in calculations with large viscosity.

In 3D calculations, gravitational potential in the vicinity of the planet is not as strongly softened as in 2D modes. In the vicinity of the planet, gas feels the gravitational potential that decreases as $-1/r$, where r is the distance from the planet, in full 3D calculations. However, the gravitational potential varies only logarithmically when $r \lesssim H$ (see equation (5.31)) in calculations restricted to 2D modes. Since the density fluctuation around the planet is
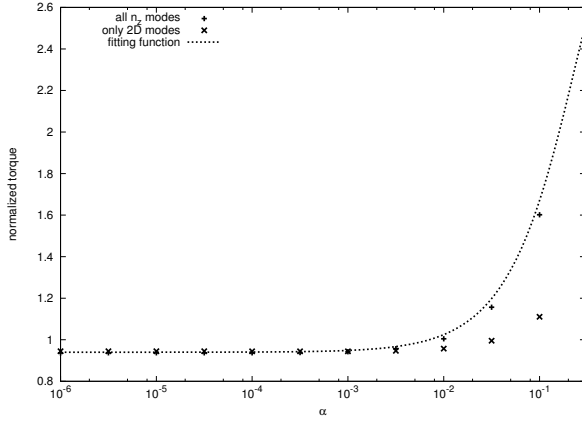
Figure 5.7: Variation of the torque as a function of viscosity parameter α obtained for 3D calculations (plus). For comparison, we plot the results restricted to 2D modes by cross. Dashed line shows the fitting function given by equation (5.38).

Figure 5.8: Torque density profile obtained by 3D calculation with various α. Solid line shows the results of $\alpha = 10^{-4}$, thick dashed line $\alpha = 10^{-2}$, and thick dotted line $\alpha = 10^{-1}$.

Figure 5.9: The contour plot of 3D mode density structure in yz-plane at $x = 0.068H$ with $\alpha = 10^{-4}$ (solid line) and $\alpha = 10^{-1}$ (dashed line). The lines show the contours of $\delta\rho/\rho_0 = 10$.

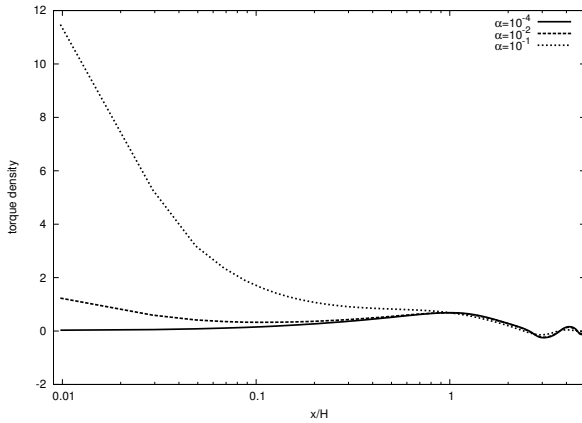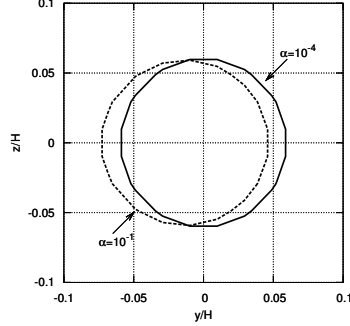given by $\delta\rho/\rho_0 \sim \psi_{\rm p}/c^2$, the deeper gravitational potential gives the higher value of the torque exerted on the planet if there is a substantial asymmetry in the density structure.

Calculations restricted to two-dimensional modes predict one-sided torque very well if viscosity parameter is small, since regions close to the planet ($r \lesssim H$) is not very important. However, if large values of viscosity is used, it is necessary to perform full three-dimensional calculations since the density structure close to the planet is important.

At the end of Section 5.1, we addressed that varying smoothing length changes one-sided torque upto 30%. Below, we discuss the effects of smoothing length in our calculation and argue that the values of one-sided torque obtained for large viscosity, $\alpha \gtrsim 0.01$, seems to be the lower limit of the one-sided torque.

Figure 5.10 shows how one-sided torque of three-dimensional calculation varies with smoothing length $\epsilon_{\rm 3D}$. Results with $\alpha = 10^{-4}$ and $\alpha = 10^{-1}$ are shown. In this calculation, we used the box size with $(L_x, L_y, L_z) = (10H, 10H, 2.5H)$ and the grid number with $(N_x, N_y, N_z) = (512, 512, 128)$. Note that resolution in the y-direction is better by a factor of four compared to the parameters used in Figure 5.7. Grid resolution is $\sim 0.02H$ in all directions in Figure 5.10.

It is shown that one-sided torque converges well for small values of viscosity parameter. If α is as large as 0.1, the calculation converges for sub-grid smoothing lengths, and results vary approximately 30% if smoothing length with twice the grid scale ($\sim 0.04H$) is assumed. The qualitative behavior
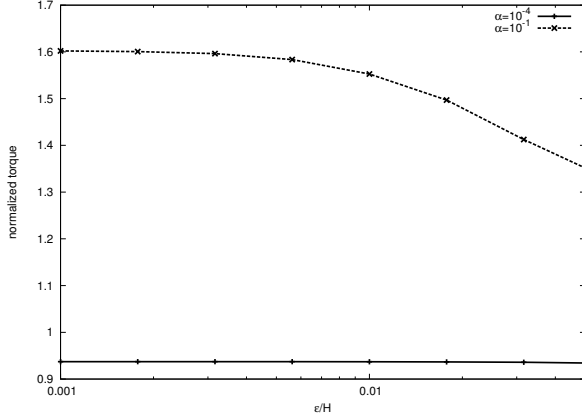
Figure 5.10: One-sided torque obtained by 3D calculation for different smoothing length. Horizontal axis shows the values of smoothing length ϵ_{3D} and vertical axis shows the one-sided torque. Calculations with $\alpha = 10^{-4}$ (solid line) and 10^{-1} (dashed line) are shown.

of one-sided torque can be understood if we notice that smaller smoothing length gives a deeper potential in the vicinity of the planet, and if large values of viscosity is assumed, density structure in the vicinity of the planet is important for one-sided torque.

Since contribution to one-sided torque in case of large viscosity mainly comes from the density structure close to the planet, it may depend on the grid resolution used in the calculation. Figure 5.11 shows the one-sided torque obtained for different resolutions. Calculations with $(N_x, N_y, N_z) = (512, 512, 128)$, $(256, 256, 64)$, and $(128, 128, 32)$ are shown while keeping $(L_x, L_y, L_z) = (10H, 10H, 2.5H)$. These values corresponds to grid resolutions with $\Delta x = \Delta y = \Delta z = 0.02H$, $0.04H$, and $0.08H$, respectively. The value of softening parameter is kept $\epsilon_{3D} = 10^{-3}H$ for all the calculations. It is shown that the value of one-sided torque for $\alpha = 10^{-4}$ is well converged while the value of the torque for $\alpha = 10^{-1}$ varies approximately 30% when grid resolution is varied by a factor of four. We note that in case of small viscosity, we have obtained well-converged values of one-sided torque since the effective Lindblad resonances, which are located at $|x| \gtrsim (2/3)H$, are all well resolved.

We note that the vertical averaging, large softening length, and coarser grid all introduce more softened potential in the vicinity of the planet and therefore one-sided torque becomes smaller in case of large viscosity. Equations (5.30) and (5.31) show that the vertically averaged potential diverges at the location of the planet more mildly. Gravitational force becomes weaker in the vicinity of the planet if we use larger values of softening length. The
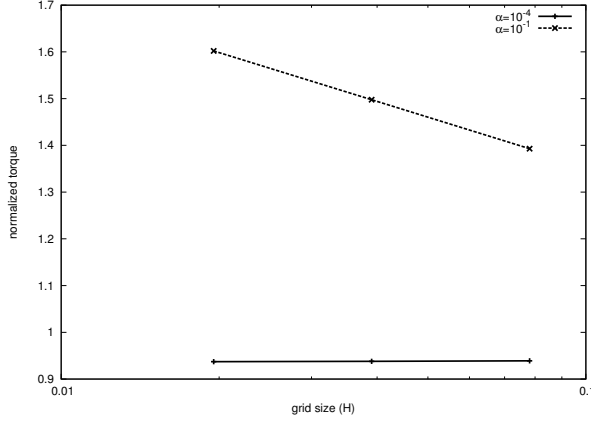
Figure 5.11: One-sided torque obtained by 3D calculation for different grid resolutions. Horizontal axis shows the values of grid size (the same for all three dimensions) and vertical axis shows the one-sided torque. Softening parameter $\epsilon_{3D} = 10^{-3}H$ is used. Calculations with $\alpha = 10^{-4}$ (solid line) and 10^{-1} (dashed line) are shown.

larger grid scale cuts off gravitational potential at larger distance.

From the behaviors when we vary the softening parameter and the grid scale, we conclude that the values of the one-sided torque obtained in our calculation for large viscosity is the lower limit. We also argue that the numerical treatment in the vicinity of the planet may cause a quantitative difference in the one-sided torque since it may change the density structure in the vicinity of the planet. If high values of viscosity is assumed, the density structure close to the planet is important and therefore, three-dimensional calculation with high resolution and small softening parameter is essential. The resolution and the softening parameter should be determined, in principle, by considering the realistic size of the planet.

5.3   Analytic Treatment of Density Structure

We have seen that the viscosity exerted on the disk can change the density structure in the vicinity of the planet and in a viscous disk, the planet experiences one-sided torque from the gas well inside the effective Lindblad resonance. In this section, we show that a dissipative force distorts the density structure close to the planet by using a simple analytic model.

We consider a two-dimensional model with a friction force exerted only in the y-direction. We consider equations (5.20)-(5.22) with viscosity terms replaced by friction. We assume $k_x(t) \sim 0$ since significant excitation of

perturbation occurs when radial wavenumber becomes zero. We also set $k_z = 0$ and consider 2D perturbation for simplicity. The set of equations we solve is

$$\frac{d\sigma}{dt} + ik_y\delta v_y = 0, \tag{5.39}$$

$$\frac{d}{dt}\delta v_x - 2\Omega_\mathrm{p}\delta v_y = 0, \tag{5.40}$$

and

$$\frac{d}{dt}\delta v_y + \frac{1}{2}\Omega_\mathrm{p}\delta v_x = -c^2 ik_y\left(\frac{\psi_\mathrm{p}}{c^2} + \sigma\right) - \gamma\delta v_y, \tag{5.41}$$

where $\sigma = \delta\rho/\rho_0$ and γ is a drag coefficient.

Using equations (5.39) and (5.40) to eliminate δv_y and integrating once the resulting equation, we obtain

$$\delta v_x = -\frac{2\Omega_\mathrm{p}}{ik_y}\sigma + V, \tag{5.42}$$

where V is a constant of integration. Physically, V is the perturbation of vortensity, which is actually conserved in this model since we neglect terms with $k_x(t)$ and we assume friction force is exerted only in the y-direction. Therefore, V is zero if we assume there is no vortensity perturbation initially. Since we are interested in the perturbation that arises from the planet potential, we assume $V = 0$ hereafter.

Using equations (5.39) and (5.42) to eliminate δv_x and δv_y from equation (5.41), we obtain a single telegraph equation with a source terms,

$$\frac{d^2\sigma}{dt^2} + \gamma\frac{d\sigma}{dt} + s_0^2\sigma = -k_y^2\psi_\mathrm{p}, \tag{5.43}$$

where

$$s_0^2 = c^2 k_y^2 + \Omega_\mathrm{p}^2. \tag{5.44}$$

The right hand side of equation (5.43) is the source of perturbation that is induced by the planet's gravity. The source potential $\psi(k_x(t), k_y)$ depends on time through the time-dependence of $k_x(t)$.

Let us now derive the steady state profile of density perturbation in (t, x, y)-coordinate space. In order to solve equation (5.43), we Fourier transform perturbation in t-direction

$$f(t, k_y) = \int_{-\infty}^{\infty} ds f(s, k_y)e^{ist}, \tag{5.45}$$

where f denotes any of perturbation quantities. We note that the Fourier transformation in t-direction is equivalent to the inverse Fourier transformation of k_x modes into x-coordinate space. The "frequency", s, in equation

(5.45) is the frequency of perturbation experienced by a single mode specified by k_y.

The real space quantity $f(x, y)$ is obtained by

$$f(x, y) = \int_{-\infty}^{\infty} dk_y \int_{-\infty}^{\infty} dk_x f(k_x, k_y) e^{i(k_x x + k_y y)}. \tag{5.46}$$

In a steady state, the value of k_x' can be taken arbitrary. Therefore, we can take $k_x' = 0$ without loss of generality. Time-dependence of k_x is given by

$$k_x(t) = \frac{3}{2} \Omega_{\mathrm{p}} k_y t, \tag{5.47}$$

and therefore, we obtain

$$dk_x = \frac{3}{2} \Omega_{\mathrm{p}} k_y dt. \tag{5.48}$$

Changing the integration variable from k_x to t in equation (5.46), we obtain

$$\begin{aligned} f(x, y) = {} & \int_0^{\infty} dk_y \int_{-\infty}^{\infty} dt \frac{3}{2} \Omega_{\mathrm{p}} k_y f(t, k_y) \exp\left[\frac{3}{2} k_y x \Omega_{\mathrm{p}} t + k_y y\right] \\ & - \int_{-\infty}^{0} dk_y \int_{-\infty}^{\infty} dt \frac{3}{2} \Omega_{\mathrm{p}} k_y f(t, k_y) \exp\left[\frac{3}{2} k_y x \Omega_{\mathrm{p}} t + k_y y\right]. \end{aligned} \tag{5.49}$$

The value $f(t, k_y)$ appeared in this equation is Fourier transformed in the t-direction according to equation (5.45). Substituting equation (5.49) into (5.45), performing integral in t and s, we obtain the relationship between $f(s, k_y)$ and $f(x, y)$,

$$\begin{aligned} f(x, y) = {} & 2\pi \int_0^{\infty} dk_y \frac{3}{2} \Omega_{\mathrm{p}} k_y \\ & \times \left[e^{ik_y y} f(s = -(3/2)\Omega_{\mathrm{p}} k_y x, k_y) + e^{-ik_y y} f(s = (3/2)\Omega_{\mathrm{p}} k_y x, -k_y)\right]. \end{aligned} \tag{5.50}$$

One-sided torque is calculated by equation (5.24) (but there is no integral in the z-direction in two-dimensional problem considered in this section). We choose the phase of the potential such that $\psi_{\mathrm{p}}(s, k_y)$ is real. It is possible because the potential of the planet is spherically symmetric and the planet is fixed at the origin of the coordinate system. Thus, we obtain

$$T \propto \int_0^{\infty} dk_y k_y^2 \int_0^{\infty} ds \mathrm{Im}\left[\sigma(s, -k_y)\right] \psi_{\mathrm{p}}(s, -k_y), \tag{5.51}$$

where constant of proportionality does not depend on k_y, γ, and x and "Im" denotes the imaginary part. From this equation, torque is exerted on the planet only when $\sigma(s, k_y)$ and $\psi_{\mathrm{p}}(s, k_y)$ are out of phase. In other words, the amount of torque can be estimated by looking at the imaginary part of $\sigma(s, k_y)$, provided that the phase of Fourier transform is taken in such a way that $\psi_{\mathrm{p}}(s, k_y)$ is real. If density perturbation and the potential are in phase, the y-component of the force exerted on the planet is symmetric in the y-direction and there is no net one-sided torque when integrated over y.

Now we consider the solution of equation (5.43). By Fourier transform in t-direction, we obtain

$$\sigma(s, k_y) = -\frac{(s_0^2 - s^2) - is\gamma}{(s_0^2 - s^2)^2 + s^2\gamma^2} k_y^2 \psi_{\mathrm{p}}(s, k_y), \qquad (5.52)$$

and as equation (5.50) indicates, it is sufficient to consider $s = (3/2)\Omega_{\mathrm{p}} k_y x$ mode.

In the limit of small friction, $\gamma \to 0$, σ and ψ_{p} are out of phase only at the resonance, which is located at

$$s^2 = \frac{9}{4}\Omega_{\mathrm{p}}^2 k_y^2 x^2 = s_0^2. \qquad (5.53)$$

From equation (5.44), we see that this corresponds to the location of effective Lindblad resonance (Artymowicz 1993 [4]). There is a phase shift of π only in the vicinity of the resonance and torque is localized at the resonance location. This localization of the torque comes from our assumption of zero radial pressure term in equation (5.40). We note that in this case, the resulting torque is independent of the amount of friction if integrated over the resonance width (Meyer-Vernet and Sicardy 1987 [60]). This can be seen by considering the imaginary part of the density fluctuation σ limits to, for sufficiently small γ,

$$\lim_{\gamma \to 0} \mathrm{Im}[\sigma(s, k_y)] = \lim_{\gamma \to 0} \frac{s\gamma}{(s_0^2 - s^2)^2 + s^2\gamma^2} k_y^2 \psi_{\mathrm{p}} = \pi \delta_D(s_0^2 - s^2) k_y^2 \psi_{\mathrm{p}}, \quad (5.54)$$

where $\delta_D(x)$ is Dirac's delta function. The last expression is independent of the amount of friction, and the torque exerted by the mode k_y is determined by the strength of the source ψ_{p} at the resonance. Using equations (5.44) and (5.53), we see that there is no resonance close to the planet, or region $|x| < x_c$, where

$$x_c = \frac{2}{3}\frac{c}{\Omega_{\mathrm{p}}}. \qquad (5.55)$$

In this region, density perturbation and source term are in phase. In terms of real space coordinate (x, y), this corresponds to $\psi_{\mathrm{p}}(x, y) \propto \sigma(x, y)$.

In the case of finite friction, the situation is different. From equation (5.52), we see that resonance width is given by $|s - s_0| \sim \gamma$. Therefore, when $\gamma \sim \Omega_\mathrm{p}$, the region in which density perturbation and source term are out of phase can overlap the location of the planet. Note that s_0 is a function of k_y and x [see equation (5.53)], so "the width of the resonance" refers to the width in the x-direction, and this width varies with the mode in the y-direction (k_y) we consider. The finite width of the resonance causes the asymmetry in density perturbation in $y > 0$ and $y < 0$ regions even at the location of the planet, $x \sim 0$. Since gravitational force exerted by the planet on the disk is large in the vicinity of the planet, the significant amount of one-sided torque can be exerted on the planet.

The amplitude of perturbation is suppressed when significant friction is exerted. From equation (5.52), we see that, in the vicinity of the planet

$$|\sigma| \sim \frac{1}{\sqrt{s_0^4 + s^2 \gamma^2}} k_y^2 \psi_\mathrm{p}(s, k_y). \tag{5.56}$$

The suppression is significant only when γ exceeds Ω_p.

One-sided torque is calculated by equation (5.24) (but there is no integral in the z-direction in two-dimensional problem considered in this section). Using equations (5.51) and (5.52), it is possible to obtain

$$T \propto \int_0^\infty dk_y k_y^4 \int_0^\infty ds \frac{s\gamma}{(s_0^2 - s^2)^2 + s^2 \gamma^2} \psi_\mathrm{p}^2(s, -k_y), \tag{5.57}$$

where constant of proportionality does not depend on k_y, γ, and x. The value of the torque is determined by the competition between the suppression of the amount of the density perturbation and the amplification of the amount of the torque as the resonance width becomes wider. Therefore, it is expected that the torque peaks at $\gamma \sim \Omega_\mathrm{p}$. This explains the peak of the torque for $\alpha \sim 1$ in the calculation of viscous disk presented in the previous section.

The qualitative behavior of one-sided torque can be captured more clearly if we consider a further simplified case. We consider the case when the forcing potential $\psi_\mathrm{p}(s, k_y)$ does not depend on s,

$$\psi_\mathrm{p}(s, k_y) = \Psi. \tag{5.58}$$

This corresponds to the case where forcing potential is constant in the x-direction. In this case, it is possible to perform s integral analytically,

$$T \propto \int_0^\infty dk_y k_y^4 \times \begin{cases} \dfrac{1}{2\sqrt{4s_0^2 - \gamma^2}} \left(\pi + 2\tan^{-1}\left[\dfrac{2s_0^2 - \gamma^2}{\gamma \sqrt{4s_0^2 - \gamma^2}} \right] \right) & \gamma^2 < 4s_0^2 \\[4mm] \dfrac{1}{2\sqrt{\gamma^2 - 4s_0^2}} \log\left[\dfrac{\gamma^2 - 2s_0^2 + \gamma\sqrt{\gamma^2 - 4s_0^2}}{\gamma^2 - 2s_0^2 - \gamma\sqrt{\gamma^2 - 4s_0^2}} \right] & \gamma^2 > 4s_0^2 \end{cases} \tag{5.59}$$

If there is only one k_y mode in the potential, this gives the exact amount of torque. Otherwise, this gives the amount of torque exerted by each mode of k_y. Limiting values of equation (5.59) are

$$
\begin{aligned}
T &\to \frac{\pi k_y^4}{2s_0} & \gamma &\to 0 \\[2mm]
T &\propto \frac{1}{|\gamma - 2s_0|} & \gamma &\sim s_0 \\[2mm]
T &\to 0 & \gamma &\to \infty.
\end{aligned}
\tag{5.60}
$$

Therefore, the amount of torque is independent of the amount of dissipation in the limit of $\gamma \to 0$, it increases as γ increases and peaks at $\gamma \sim s_0$, and then it decreases to zero as γ becomes very large. In case of small γ, the integrand of (5.57) is localized at $s \sim s_0$. When γ is large, however, it is necessary to consider contribution from all the region of s. In general, since the amplitude of forcing term $\psi_\mathrm{p}(s, k_y)$ increases as $s \to 0$, it is expected that the value of torque peaks at $\gamma \sim s_0$. If the amplitude of forcing term cuts off at $\Omega_\mathrm{p}^2 \sim c^2 k_y^2$, the peak of the torque is expected at $\gamma \sim \Omega_\mathrm{p}$.

5.4 Discussion

5.4.1 Prospects of Modified Local Analysis and Global Calculation

Validity of Linear Analysis on One-sided Torque

In this subsection, we discuss whether or not linear approximation well describes the real density structure around the planet. In the linear approximation, the magnitude of perturbed quantities such as $\delta\rho/\rho_0$ or $\delta\boldsymbol{v}/c$ must be smaller than the order of unity. In our calculation, all the non-dimensional perturbed quantity is proportional to the value of GM_p/Hc^2, which is about $10^{-1} - 10^{-2}$ for typical values of protoplanetary nebula. Therefore, when $\delta\rho/\rho$ becomes the order of ten in the normalized calculations given in this paper, linear approximation becomes less accurate. Since the contribution of the torque in a viscous disk mainly comes from such strongly perturbed regions, it may be necessary to perform high resolution numerical calculation in order to fully obtain the structure of the density fluctuation. This is one of the future prospects of this study. However, we expect that the basic physics and the order of magnitude of one-sided torque is similar to the linear calculation.

Differential Lindblad Torque

The total torque that is exerted on the planet is the differential torque, which is the difference of the torque exerted by the inner disk ($x < 0$) and outer disk ($x > 0$). In the shearing-sheet calculations, the inner and outer disks are symmetric and therefore torque exerted on the two regions cancel each other. We have seen that the one-sided torque is mainly exerted by the tilted spheroidal density profile around the planet if strong viscosity is exerted on the disk. Therefore, we expect that the asymmetry between the inner and outer disk comes from the asymmetry of the density structure around the planet, probably within, or around, the distance of the order of Bondi radius, $r_{\rm B} = GM_{\rm p}/c^2$. Assuming that the differential torque $T_{\rm diff}$ mainly comes from the effects of curvature, the order of the magnitude is

$$T_{\rm diff} \sim T_{\rm one-side} \times \frac{\delta x}{r_{\rm p}}, \tag{5.61}$$

where $T_{\rm one-side}$ is one-sided torque obtained in this paper, and δx is the length scale where most contribution to the torque comes from. In the inviscid case, $\delta x \sim H$ and therefore

$$T_{\rm diff,inviscid} \sim T_{\rm one-side,inviscid} \times \frac{H}{r_{\rm p}}. \tag{5.62}$$

In the viscous case presented in this paper, δx may be as small as Bondi radius $r_{\rm B}$. Therefore, the lower limit of the differential torque in viscous disk may be estimated as

$$T_{\rm diff,viscous} \sim T_{\rm one-side,viscous} \times \frac{r_{\rm B}}{r_{\rm p}}, \tag{5.63}$$

and the ratio of differential torque in viscous disk and that in inviscid disk may be given by

$$\frac{T_{\rm diff,viscous}}{T_{\rm diff,inviscid}} \sim \frac{T_{\rm one-side,viscous}}{T_{\rm one-side,inviscid}} \times \frac{r_{\rm B}}{H}. \tag{5.64}$$

Since

$$\frac{r_{\rm B}}{H} \sim \frac{M_{\rm p}}{M_{\rm c}} \left(\frac{r_{\rm p}}{H}\right)^3 = 8 \times 10^{-3} \left(\frac{10^{-6}}{M_{\rm p}/M_{\rm c}}\right) \left(\frac{0.05}{H/r_{\rm p}}\right)^{-3}, \tag{5.65}$$

and $T_{\rm one-side,viscous}/T_{\rm one-side,inviscid} \sim 2$ from our calculation, differential torque in a viscous disk can be much smaller than that in an inviscid disk, although one-sided torque becomes larger when the value of viscosity is $\alpha \sim 1$.

In order to include the effect of asymmetry, which comes from curvature effect, it is necessary to proceed to modified local approximation (Tanaka et

al. 2002 [83]) or to perform a global calculation. In order to find the precise value of the torque exerted on the disk and find how various physical processes change the nature of type I migration, the time-dependent formulation of modified local approximation is necessary.

Corotation Torque

In the shearing-sheet formalism, we cannot calculate corotation torque. For two-dimensional modes, this is because all the background quantities (and therefore vortensity) are assumed to be constant. For three-dimensional modes, we note that, in Tanaka et al. (2002) [83], there is a singularity at corotation modes (see equation (A5) of their paper). However, this singularity does not account for the torque in itself. Results of shearing-sheet calculations must be combined with the higher order solutions of modified local approximation in order to find the torque exerted at corotation resonance, see equation (57) of Tanaka et al. (2002) [83].

If we assume that time derivatives of equations (3.3) and (5.7) are zero in order to obtain a stationary solution, we also find a similar singularity at $x = 0$ for three-dimensional waves ($k_z \neq 0$), even we have assumed the constant background density in the z-direction. However, within the shearing-sheet formalism, it does not give a torque at the corotation. Also, this singularity does not seem to play a major role in our time-dependent calculations, since there is no singularity in our formulation.

If we proceed to the modified local approximation, we expect that it is possible to calculate the corotation torque in the linear regime. Recently, Paardekooper and Papaloizou (2009a) [69] has shown that large viscosity will push the corotation torque into a linear regime. Therefore, not only from the point of view of differential torque but also from the view of the corotation torque, extension of our time-dependent methods to modified local approximation is an interesting future work.

In summary, in order to predict the precise value of the torque, it is necessary to use a modified local approximation or perform global calculations, which can take into account the curvature effect. Non-linear analysis may be important since the main contribution comes from the region in the vicinity of the planet where density is strongly perturbed. However, we believe that the basic physics that exerts torque onto the planet can be captured by this linear analysis and therefore, high-resolution study is necessary. In global calculations, we also note that it is also possible to investigate the effects of gas accretion onto the central star on type I migration, which is always present in a viscous disk but is not captured in our local calculations.
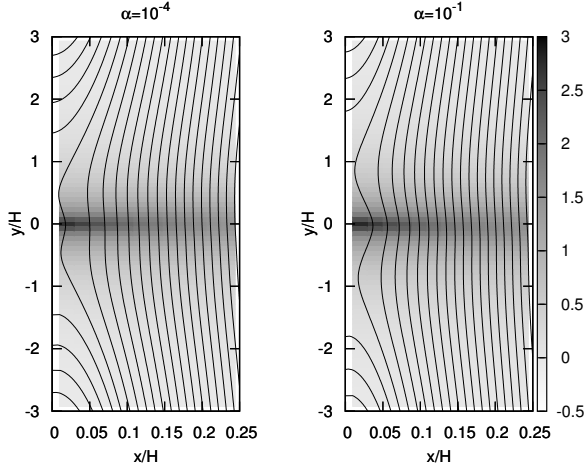
Figure 5.12: Density and streamline for calculations restricted to 2D mode in 3D calculation with $\alpha = 10^{-4}$ (left) and $\alpha = 10^{-1}$ (right). This corresponds to the calculations presented in Figure 5.4. Mass ratio between the central star $q = M_{\mathrm{p}}/M_{\mathrm{c}}$ and disk aspect ratio $h = H/r_p$ are assumed in such a way that $q/h^3 = 0.0252$, which is the same as Paardekooper and Papaloizou (2009b). Gray scale shows the density perturbation $\delta\rho/\rho_0$ divided by q/h^3 and solid lines are streamlines.

5.4.2   Flow Structure in the Vicinity of the Planet

Recently, Paardekooper and Papaloizou (2009) [70] has shown an interesting results regarding the flow structure close to the planet. In this section, we observe streamline of the flow in the vicinity of the planet and compare our results with those previously studied. We note that since we have not calculated axisymmetric ($k_y = 0$) modes, the flow structure we have obtained is incomplete. However, we can still find some qualitative difference between inviscid and viscous calculations.

Figure 5.12 shows the streamlines plotted over the density fluctuations for calculations corresponding to Figure 5.4. Results with $\alpha = 10^{-4}$ and $\alpha = 10^{-1}$ are shown. Calculations are restricted to 2D modes of 3D calculation. Mass ratio between the planet and the central star $q = M_{\mathrm{p}}/M_{\mathrm{c}}$ and disk aspect ratio $h = H/r_{\mathrm{p}}$ are assumed in such a way that $q/h^3 = 0.0252$, just as Paardekooper and Papaloizou (2009) [70].

We find that the width of horseshoe orbit is $\sim 0.1H$ for $\alpha = 10^{-4}$, while the width becomes slightly narrower in calculations with $\alpha = 10^{-1}$. We have obtained about a factor of two smaller horseshoe width compared to Paardekooper and Papaloizou (2009) [70] in calculations with small viscosity

(see Figure 3 of their paper.) We think that this is probably because we have weaker potential in the vicinity of the planet because of the effective softening introduced by vertical averaging, see equation (5.31). In Paardekooper and Papaloizou (2009) [70], they also obtained narrower horseshoe width in calculations with larger softening parameters. However, since we have neglected axisymmetric modes and non-linear effects, which may be potentially important in determining the streamline, this issue needs further investigation.

5.4.3 Axisymmetric Modes

Although we have neglected the axisymmetric modes in our calculations, a viscous overstability in axisymmetric modes has been discussed, especially in the context of Saturn's rings. In this subsection, we discuss whether this overstability affects our results.

Local linear analysis of viscous overstability using a simple hydrodynamic model is performed by Schmidt et al. (2001) [77]. Stability criterion for isothermal case depends on the derivative of viscous coefficient ν with respect to surface density perturbation. We note that the system of equations we have solved, equations (5.20)-(5.23), are actually stable against viscous overstability, since our assumption of viscosity corresponds to $\beta = -1$ of Schmidt et al. (2001) [77]. [4] In this case, we do not expect viscous overstability to occur and therefore, we can safely neglect the axisymmetric modes.

However, disk may be prone to viscous overstability if different prescription of viscosity is taken into account. If the non-linear consequence of viscous overstability produces non-axisymmetric structure in the vicinity of the planet, this may exert additional torque onto the planet. However, observation of the particle simulation performed by Schmidt et al. (2001) [77] (their Figure 1 for example) indicates that non-axisymmetric modes are not strongly driven by the viscous overstability and therefore this may not play an important role in planetary migration. Nonetheless, the effects of viscous overstability seems to be an interesting extension of the analysis presented here.

5.4.4 Turbulent Disk

In this subsection, we briefly discuss that our analysis may indicate that the stochastic torque is important in a turbulent disk dominated by magneto-rotational instability (see e.g., Nelson and Papaloizou 2004 [65]). The effec-

---

[4]Compare our equations (5.6) and (5.7) and their equation (8). Note there is no self-gravity and bulk viscosity in our calculations and we assumed isothermal equation of state.

tive turbulent viscosity originated in MRI may become as much as $\alpha \sim 0.1$ (e.g., Sano et al. 2004 [74]). Therefore, our calculation indicates that the density structure around the planet is more important than the tidal wave launched at the effective Lindblad resonances. Since the density structure around the planet is turbulent in the vicinity of the planet, stochastic force may be exerted on the planet embedded in such a turbulent disk.

In order for the α-viscosity prescription [see equation (5.27)] to be a good approximation of the turbulent flow, the length scale in consideration must be larger than the eddy size. In the present problem, the scale in consideration is smaller than disk thickness. In a turbulent flow driven by MRI, eddies of sizes on the order of several tenths of the disk scale lengths exist. This can be understood if we notice that the wavelength of the most unstable mode is much smaller than the scale height of the disk with weak magnetic field. If weak poloidal magnetic field, B_{z0}, is exerted on the unperturbed disk, there always exists a net magnetic flux,

$$\langle B_z \rangle = B_{z0}, \tag{5.66}$$

where $\langle B_z \rangle$ is the horizontally averaged z-component of magnetic field. Therefore, there always exists eddies with scales of the order of the most unstable mode of magneto-rotational instability with net flux B_{z0},

$$\lambda \sim \frac{v_{A,0}}{\Omega}, \tag{5.67}$$

where λ is the eddy scale, $v_{A,0} = B_{z0}/\sqrt{4\pi\rho}$ is Alfvén velocity constructed from the average poloidal field, and Ω is Keplerian angular frequency. In most cases, Alfvén velocity is smaller than sound speed by more than an order of a magnitude,

$$v_{A,0} \lesssim 10^{-1} c. \tag{5.68}$$

This indicates

$$\lambda \lesssim 10^{-1} H. \tag{5.69}$$

Thus, we can possibly use the effective turbulent viscosity in order to study the qualitative effects of the interaction between a turbulent disk and a planet.

However, the effective values of α may be obtained by averaging turbulent stress over several scale heights, since it includes all sizes of eddy that is important in turbulent flow driven by MRI. Thus, the use of α prescription may not be valid in discussing very small scale structure, and full MHD calculation is necessary. More detailed, quantitative analyses require high-resolution numerical study of the magnetized turbulent disk.

We have found that the effects of viscosity becomes apparent if α exceeds the value of $\sim 0.01 - 0.1$. Actual values of α in the disk is largely uncertain, but estimated values are around this value. Numerical simulations by Sano et al. (2004) [74] indicates that the values of α varies from $10^{-4} - 10^{-1}$ depending on the setup. From the observational constraints of dwarf novae, which seem to be better studied than protoplanetary disks, it is indicated that the values of α can vary from 0.01 to 0.1 (e.g., Cannizzo et al. 1988 [12]). The values of α seems to be an open issue for both theoretically and observationally.

Chapter 6

Weakly Non-linear Analyses

So far, we have mainly focused on the linear perturbation of disk-planet interaction. Linear analyses help us to understand some properties of disk-planet interactions. For example, it is possible to derive the torque exerted at Lindblad resonances by low-mass planets, and therefore, it is possible to calculate the timescale of planetary migration.

However, it is also noted that the applicability of linear perturbation theory is restrictive. Obviously, it cannot be applied for high-mass planet. Since the amplitude of perturbation scales with GM_p/Hc^2, we expect that if the planet mass exceeds Neptune or Saturn mass, linear perturbation theory fails.

It is also pointed out recently that linear perturbation theory fails for low-mass planets. Paardekooper and Papaloizou (2008) [69] have shown that the interaction at the corotation resonances are not described by linear theory. It is also known that it is not possible to derive mass flux by linear perturbation theory (Balbus and Hawley 1998 [7], Lubow 1990 [54]).

In this chapter, we investigate the disk-planet interaction in a weakly non-linear regime. Our goal is to derive the mass flux excited by the planet embedded in a disk, which results in the gap formation around the planet. Gap formation is important because if a gap is formed in the vicinity of the planet, the surface density of the gas decreases. Since type I migration timescale is proportional to the disk surface density at effective Lindblad resonances, the type I migration timescale becomes longer if gap is formed.

We first give some analytic framework of non-linear disk-planet interaction. We then perform numerical simulations to verify the analytic results. Finally, we discuss the gap formation criterion based on the results. We consider a very simple case: two-dimensional local shearing-sheet analysis with isothermal gas. This may be a great simplification, but the analyses are also simplified and high-resolution calculations are possible. We expect

that essential physical mechanisms of gap formation can be captured by this analysis.

6.1   Basic Equations

As usual, we take the origin of the coordinate system at the planet's location, and the x- and y-axes are the radial and the azimuthal direction, respectively. We use iso-thermal ideal hydrodynamic equations

$$\frac{\partial \rho}{\partial t} + \nabla \cdot (\rho \mathbf{v}) = 0 \tag{6.1}$$

$$\frac{\partial \mathbf{v}}{\partial t} + \mathbf{v} \cdot \nabla \mathbf{v} = -\frac{c^2}{\rho} \nabla \rho - 2\Omega_p \mathbf{e}_z \times \mathbf{v} + 3\Omega_p^2 x - \nabla \psi_{\mathrm{p}} \tag{6.2}$$

where we have assumed that the gas is rotating at the Kepler velocity. Notations are as follows: ρ is density, $\mathbf{v}$ is velocity field, c is sound speed, Ω_{p} is the angular velocity of the planet, and ψ_{p} is the gravitational potential of the planet. For ψ_{p}, we assume the form

$$\psi_{\mathrm{p}} = \frac{GM_{\mathrm{p}}}{\left(x^2 + y^2 + \epsilon^2\right)^{1/2}}, \tag{6.3}$$

where G, M_{p}, and ϵ are gravitational constant, mass of the planet, and the softening parameter, respectively.

6.2   Second-Order Perturbation Theory

In this section, we consider second-order linear perturbation in order to derive the mass flux in the vicinity of the planet. Although angular momentum flux can be calculated using the results of linear perturbation only, it is necessary to perform second-order analysis to derive the mass flux, since axisymmetric ($k_y = 0$) mode of the second-order perturbation contributes to the mass flux. Lubow (1990) [54] performed the time-dependent analysis using Fourier and Laplace transformation. In this section, we revisit the second-order perturbation theory using a slightly different method from the previous calculations. We use Fourier-transform in the y-direction only and analyze in the real space in time and the x-direction.

The equations for second-order perturbation are given by

$$\left(\frac{\partial}{\partial t} - \frac{3}{2}\Omega_{\mathrm{p}}x\frac{\partial}{\partial y}\right)\frac{\delta\rho^{(2)}}{\rho_0} \quad + \frac{\partial}{\partial x}\delta v_x^{(2)} + \frac{\partial}{\partial y}\delta v_y^{(2)} =$$
$$-\frac{\partial}{\partial x}\left(\frac{\delta\rho^{(1)}}{\rho_0}\delta v_x^{(1)}\right) - \frac{\partial}{\partial y}\left(\frac{\delta\rho^{(1)}}{\rho_0}\delta v_y^{(1)}\right) \tag{6.4}$$

$$\left(\frac{\partial}{\partial t} - \frac{3}{2}\Omega_{\mathrm{p}}x\frac{\partial}{\partial y}\right)\delta v_x^{(2)} \quad +c^2\frac{\partial}{\partial x}\frac{\delta\rho^{(2)}}{\rho_0} - 2\Omega_{\mathrm{p}}\delta v_y^{(2)} =$$

$$-\delta v_x^{(1)}\frac{\partial}{\partial x}\delta v_x^{(1)} - \delta v_y^{(1)}\frac{\partial}{\partial y}\delta v_x^{(1)} + c^2\frac{\delta\rho^{(1)}}{\rho_0}\frac{\partial}{\partial x}\frac{\delta\rho^{(1)}}{\rho_0}$$

$$\tag{6.5}$$

$$\left(\frac{\partial}{\partial t} - \frac{3}{2}\Omega_{\mathrm{p}}x\frac{\partial}{\partial y}\right)\delta v_y^{(2)} \quad +c^2\frac{\partial}{\partial y}\frac{\delta\rho^{(2)}}{\rho_0} + \frac{1}{2}\Omega_{\mathrm{p}}\delta v_x^{(2)} =$$

$$-\delta v_x^{(1)}\frac{\partial}{\partial x}\delta v_y^{(1)} - \delta v_y^{(1)}\frac{\partial}{\partial y}\delta v_y^{(1)} + c^2\frac{\delta\rho^{(1)}}{\rho_0}\frac{\partial}{\partial x}\frac{\delta\rho^{(1)}}{\rho_0}.$$

$$\tag{6.6}$$

The superscripts "(1)" and "(2)" denote the first- and second-order perturbation, respectively. We assume that the first-order results are already known.

The mass flux is given by

$$\dot{M}(t,x) = \rho_0\overline{\delta v_x^{(2)}} + \overline{\delta\rho^{(1)}\delta v_x^{(1)}}, \tag{6.7}$$

where bars denote the integral over y. Assuming the periodic boundary condition in the y-direction, it is possible to derive the equation for $\dot{M}$ which reads

$$\frac{\partial^2\dot{M}}{\partial t^2} - c^2\frac{\partial^2\dot{M}}{\partial x^2} + \Omega_{\mathrm{p}}^2\dot{M} = S(t,x), \tag{6.8}$$

where S is the source term consisting of two parts,

$$S(t,x) = S_v(t,x) + \frac{\partial}{\partial t}S_t(t,x), \tag{6.9}$$

and

$$S_v(t,x) = 2\Omega_{\mathrm{p}}\left[\frac{\Omega_{\mathrm{p}}}{2}\overline{\delta\rho^{(1)}\delta v_x^{(1)}} - c^2\overline{\delta v_x^{(1)}\partial_x\delta v_y^{(1)}}\right] \tag{6.10}$$

$$S_t(t,x) = \partial_t\left(\overline{\delta\rho^{(1)}\delta v_x^{(1)}}\right) - \left[\overline{\delta v_x^{(1)}\partial_x\delta v_x^{(1)}} + \overline{\delta v_y^{(1)}\partial_y\delta v_x^{(1)}} - \frac{c^2}{\rho_0}\overline{\delta\rho^{(1)}\partial_x\delta\rho^{(1)}}\right] \tag{6.11}$$

The term S_v is related to the formation of specific vorticity. In two-dimensional ideal flow in a rotating frame, the specific vorticity conserves along the streamline

$$\frac{d}{dt}\frac{(\nabla\times\mathbf{v})_z + 2\Omega_{\mathrm{p}}}{\rho} = 0, \tag{6.12}$$

where d/dt is the Lagrangian derivative. The background value of the specific vorticity is $\Omega_{\mathrm{p}}/2$, and the linear perturbation is

$$\left(\frac{\partial}{\partial t} - \frac{3}{2}\Omega_{\mathrm{p}}\frac{\partial}{\partial y}\right)\left[\frac{\partial}{\partial y}\delta v_x^{(1)} - \frac{\partial}{\partial x}\delta v_y^{(1)} + \frac{1}{2}\Omega_{\mathrm{p}}\frac{\delta\rho^{(1)}}{\rho_0}\right] = 0. \qquad (6.13)$$

If there is no formation of specific vorticity,

$$\frac{\partial}{\partial y}\delta v_x^{(1)} - \frac{\partial}{\partial x}\delta v_y^{(1)} + \frac{1}{2}\Omega_{\mathrm{p}}\frac{\delta\rho^{(1)}}{\rho_0} = 0 \qquad (6.14)$$

and from equation (6.10), $S_v(t, x) = 0$. However, if there is a formation of vorticity by, for example, shock damping of the spiral density wave, this term can not be neglected. We also note that if stationary state is assumed a priori, and if there is no formation of specific vorticity, the source term $S(t, x)$ is zero, leading to the zero mass flux (Lubow 1990, Muto and Inutsuka 2009).

However, if time-evolution effects are taken into account, we derive non-zero mass flux. The solution for equation (6.8) is given by

$$\dot{M}(t, x) = \frac{1}{c}\int\int dt_0 dx_0 G(t, t_0; x, x_0)S(t_0, x_0), \qquad (6.15)$$

where $G(t, t_0; x, x_0)$ is the Green's function

$$G(t, t_0; x, x_0) = \begin{cases} \frac{1}{2}J_0\left(\frac{1}{H}\sqrt{(t-t_0)^2 - (x-x_0)^2/c^2}\right) & |x - x_0| < c(t - t_0) \\ \\ 0 & \text{otherwise} \end{cases} \qquad (6.16)$$

where J_0 is the Bessel function of zeroth order. From linear perturbation, it is possible to predict that the mass flux scales with M_{p}^2, since the source term is the second order of perturbation.

6.3   Non-Linear Evolution of Density Wave

We have seen that mass flux appears when source term is time-dependent or when there is a formation of specific vorticity. Since we consider the phase when the planet mass does not change very much, the mass flux, if there is, should appear as a result of the formation of specific vorticity.

Specific vorticity is formed when dissipation mechanisms act. Goodman and Rafikov (2001) [39] investigated the propagation of density wave and showed that the spiral density wave shocks as it propagates in the disk. They have derived that the location of shock formation is proportional to

$M_{\mathrm{p}}^{-2/5}$. In this section, we derive this relationship using a slightly different consideration.

Shock is formed when two characteristics cross. For two-dimensional supersonic steady flow, the gradient of characteristic curves is given by (Landau and Lifshitz 1959 [51])

$$\left(\frac{dy}{dx}\right)_{\pm} = \frac{v_x v_y \pm c\sqrt{v^2 - c^2}}{v_x^2 - c^2}. \tag{6.17}$$

In the background state of the shearing-sheet, this gives

$$\left(\frac{dy}{dx}\right)_{\pm} = \pm\frac{1}{c}\left(\frac{9}{4}\Omega_{\mathrm{p}}^2 x^2 - c^2\right)^{\frac{1}{2}}. \tag{6.18}$$

For $x > 0$, $(dy/dx)_-$ is the perturbation propagating away from the origin. At $x \gg (2/3)H$, the characteristic curve is given by

$$y \sim -\frac{2}{3}\frac{x^2}{H} + y_0. \tag{6.19}$$

It is to be noted that the outgoing characteristics coincide the curve of the same phase of the perturbation of the density wave. This is not a coincidence, since the density wave is essentially the sound wave propagating on the disk.

For linear perturbation, the gradient of the characteristics is given by

$$\left(\frac{dy}{dx}\right)_{\pm} \sim \frac{1}{c^2}\left[\mp c\left(\frac{9}{4}\Omega_{\mathrm{p}}^2 x^2 - c^2\right)^{\frac{1}{2}} + \frac{3}{2}\Omega_{\mathrm{p}} x\left\{\delta v_x \pm \frac{c\delta v_y}{\left((9/4)\Omega_{\mathrm{p}}^2 x^2 - c^2\right)^{1/2}}\right\}\right] \tag{6.20}$$

Since the amplitude of δv_y decreases with $x^{-1/2}$, δv_y in the second term of the right hand side can be neglected. Assuming the perturbed characteristic curve of the form

$$y(x) = -\frac{3}{2}\frac{x^2}{H} + y_0 + \delta y(x), \tag{6.21}$$

$\delta y(x)$ may be given by

$$\frac{d}{dx}\delta y = \frac{3}{2}\frac{\Omega_{\mathrm{p}}}{c^2}x\delta v_x(x, y(x)). \tag{6.22}$$

Approximating $y(x) \sim -(3/2)x^2/H + y_0$ in the argument of δv_x, we have

$$\delta y(x) \propto M_{\mathrm{p}} x^{5/2} g(y_0). \tag{6.23}$$

In the vicinity of $g(y_0) = 0$, $g(y)$ is negative for $y > y_0$ and $g(y)$ is positive for $y < y_0$. This indicates that the characteristic curves shrinks compared to

the unperturbed case. Assuming that when δy exceeds a critical value, the shock forms, we obtain, for the location of the shock formation,

$$x \propto M_{\rm p}^{-2/5}, \tag{6.24}$$

which is the same condition as derived by Goodman and Rafikov (2001). Since the flow is supersonic only $x > (2/3)H$, condition

$$\left| x - \frac{2}{3}H \right| \propto M_{\rm p}^{-2/5} \tag{6.25}$$

may be more appropriate.

The distance over which the spiral density wave can propagate without shock formation may be of the order of the scale height. If it is the case, spiral shock will create the specific vorticity, and as a result, mass flux is excited to form a gap around the disk. In the subsequent section, we investigate whether gap formation is possible using numerical calculations.

6.4   Numerical Calculation

In order to investigate the gap opening process more quantitatively, we perform numerical calculations of disk-planet interaction.

6.4.1   Numerical Setup

We solve Euler equations (6.1) and (6.2) with isothermal equation of state using second-order Godunov scheme (e.g., Colella and Woodward 1984 [16]). In order to investigate the density wave propagation while resolving all the length scale (Hill radius, Bondi radius, and radial wavelength of the density wave), we need to use rather large box size with relatively high resolution. We choose the box size $(L_x, L_y) = (16H, 32H)$ with mesh number $(N_x, N_y) = (512, 1024)$, which results in the resolution $\Delta x = \Delta y = H/32$.

Using linear perturbation theory in WKB limit, the radial wavelength of the wave with mode k_y may be approximated by

$$\lambda \sim H \frac{8\pi}{3} \frac{1}{k_y H} \frac{H}{x}. \tag{6.26}$$

The most important modes are $k_y H \sim \mathcal{O}(1)$. For mode with $k_y H = 10$ at $x/H \sim 4$, $\lambda \sim 1/4$, and this wave is resolved by eight meshes in the radial direction if we use $\Delta x = H/32$. Higher-order modes or the wave outside this regions are damped numerically. Therefore, we mainly use data within

Model Number	GM_p/Hc^2	Planet Mass	r_H/H
1	0.05	$1.875 M_\oplus$	0.26
2	0.1	$3.75 M_\oplus$	0.32
3	0.2	$7.5 M_\oplus$	0.41
4	0.4	$15 M_\oplus$	0.51
5	0.6	$22.5 M_\oplus$	0.58

Table 6.1: Mass parameters used in numerical calculations. For the calculation of planetary mass, we assume 1AU of MMSN Model

$|x| < 4H$ in the analyses of the results. We set the numerical boundary well-outside this region.

If we normalize the length by $H = c/\Omega_p$ and the time by Ω_p, the only dimensionless parameters in this calculation is the planet mass, or Bondi radius $r_B/H = GM_p/Hc^2$ and the softening parameter ϵ/H. We use the softening length used in previous local shearing-sheet calculations $\epsilon = r_H/4$, where r_H is the Hill's radius

$$r_H = \left(\frac{M_p}{3M_c} \right)^{1/3} r_p \qquad (6.27)$$

(Miyoshi et al. 1999 [61]). We have performed calculations with five different planetary mass M_p shown in Table 6.1. Note that Bondi radius, Hill radius, and the softening parameter are resolved (at least marginally) for the smallest mass model. We have increased the planetary mass linearly from $t\Omega_p = 0$ to 12. The result does not depend on significantly on this timescale if the timescale is longer than this.

In the x-direction, we use the non-reflecting boundary used by FARGO (Baruteau 2008 [9]), modified for the shearing-sheet. For the y-direction, we adopt the periodic boundary condition. Shearing-sheet calculations given by Miyoshi et al. (1999) [61] or Tanigawa and Watanabe (2002) [85] used the different boundary conditions in the y-direction, which is the combination of Keplerian inflow and supersonic outflow. This boundary condition may be appropriate to study the flow structure only in the vicinity of the planet, but for the study of gap formation, this boundary condition is inappropriate because this forces the unperturbed gas flowing into the computational domain. We also note that the periodic boundary condition in the y-direction is useful for the purpose of comparison with the linear analyses, which assume the periodicity in the y-direction.

We have checked that our code reproduces the results of Miyoshi et al. (1999) [61] well when the same parameter and the boundary conditions are used.
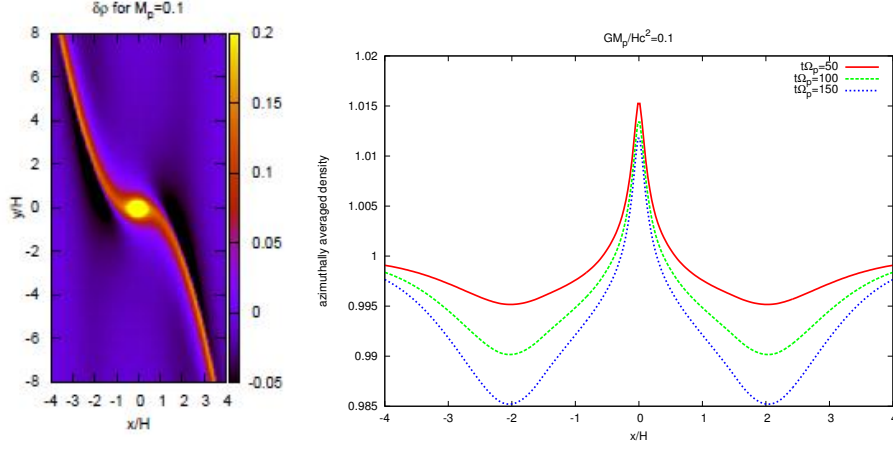
Figure 6.1: Left: Density profile for the calculation with $GM_{\mathrm{p}}/Hc^2 = 0.1$ at $t\Omega_{\mathrm{p}} = 200$. Right: Evolution of azimuthally averaged density for $GM_{\mathrm{p}}/Hc^2 = 0.1$.

6.4.2   Results

Figures 6.1 and 6.2 show the snapshot of density perturbation $\delta\rho$ $t\Omega_{\mathrm{p}} = 200$ and the evolution of the azimuthally averaged density profile for $GM_{\mathrm{p}}/Hc^2 = 0.1$ and 0.4 respectively. For the calculation with $GM_{\mathrm{p}}/Hc^2 = 0.4$, a clear gap is already formed, but it is possible to see that even for low-mass calculations, density gap is gradually formed.

We now investigate the gap formation in detail. We first investigate the shock formation. Figure 6.3 shows the density profiles at various x at $t\Omega_{\mathrm{p}} = 200$. It is possible to see the shock-like structure for the calculation with $GM_{\mathrm{p}}/Hc^2 = 0.4$, while for the run with $GM_{\mathrm{p}}/Hc^2 = 0.1$, the structure is not very obvious.

However, we argue that the spiral shock already forms for the low mass calculations as well. It is possible to see whether dissipation acts or not by looking at the perturbation of specific vorticity. In the absence of dissipation, the specific vorticity conserves along the streamline, and since the background specific vorticity is constant in the calculation box, we expect that it is also constant in the presence of the planet. Note that any potential force, whether it is time-dependent or not, does not produce specific vorticity. Therefore, specific vorticity arises only if dissipative mechanisms come into play. In our calculation, the dissipation is implemented in the shock-capturing scheme. If the formation of specific vorticity is driven by the formation of shock, relation given by equation (6.25) should be observed a least for the weak shock cases.

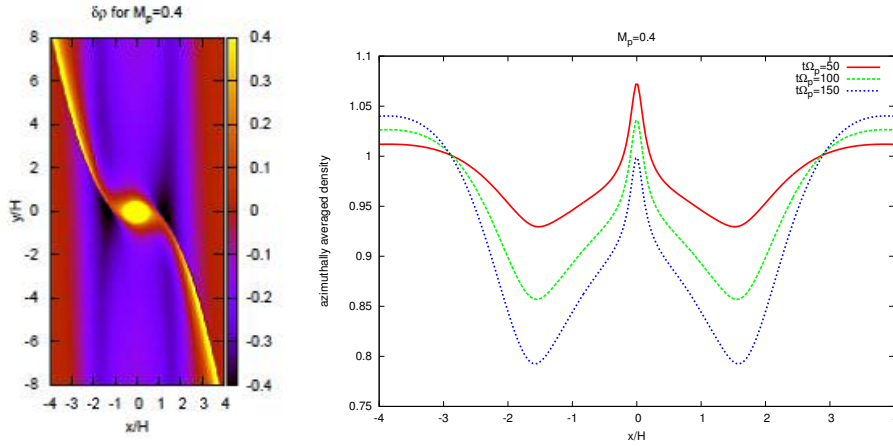Figure 6.4 shows the azimuthally-integrated specific vorticity perturba-

Figure 6.2: Left: Density profile for the calculation with $GM_{\mathrm{p}}/Hc^2 = 0.4$ at $t\Omega_{\mathrm{p}} = 200$. Right: Evolution of azimuthally averaged density for $GM_{\mathrm{p}}/Hc^2 = 0.4$.
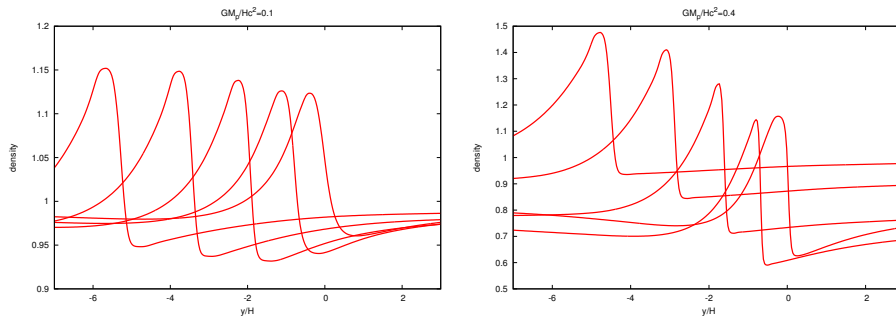

Figure 6.3: Left: Density profile for the calculation with $GM_{\mathrm{p}}/Hc^2 = 0.1$ at $t\Omega_{\mathrm{p}} = 200$. Profiles at $x/H = 1$, 1.5, 2, 2.5, and 3 are shown from right to left. Right: Same as left panel but for $GM_{\mathrm{p}}/Hc^2 = 0.4$.
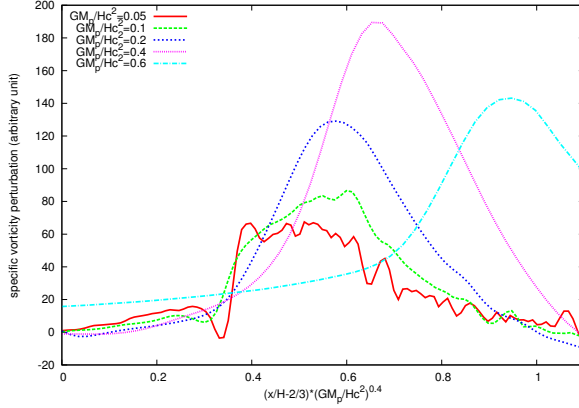
Figure 6.4: Perturbation of specific vorticity (in arbitrary unit) as a function of $(x - (2/3)H)M_{\mathrm{p}}^{2/5}$

tion as a function of $(x-(2/3)H)M_{\mathrm{p}}^{2/5}$. If shock dissipation occurs as equation (6.25) describes, the peak of the specific vorticity perturbation comes at the same location of the horizontal axis. It is possible to observe that the for calculations with $GM_{\mathrm{p}}/Hc^2 < 0.2$, equation (6.25) is marginally satisfied. For calculations with larger planet mass, it is not the case. This is because the shock formation occurs immediately after the wave is excited at $x \sim (2/3)H$, and therefore in the unit of $x - (2/3)H$, the shock occurs relatively further away.

We now look at the radial mass flux $\overline{\rho v_x}$ excited by the planet. In Figure 6.5, we show the azimuthally averaged mass flux at $t\Omega_{\mathrm{p}} = 100$. It is possible to see that the mass flux is roughly proportional to M_{p}^2 except for the highest-mass calculation. This motivates us to compare the results with second-order perturbation theory given by equation (6.15).

Figure 6.6 compares the mass flux derived by numerical calculation and by equation (6.15). Since it is not possible to predict the amount of specific vorticity only from linear perturbation theory, we have used the results of numerical calculation in obtaining the source term $S(t,x)$. It is possible to observe that the second-order perturbation theory is valid for calculations with low-mass planet, $GM_{\mathrm{p}}/Hc^2 = 0.1$. We find that perturbation theory fails to describe the amount of mass flux for calculations with $GM_{\mathrm{p}}/Hc^2 \gtrsim 0.4$. However, we note that it is still possible to say that the mass flux is roughly proportional to M_{p}^2 even if second-order perturbation theory fails.
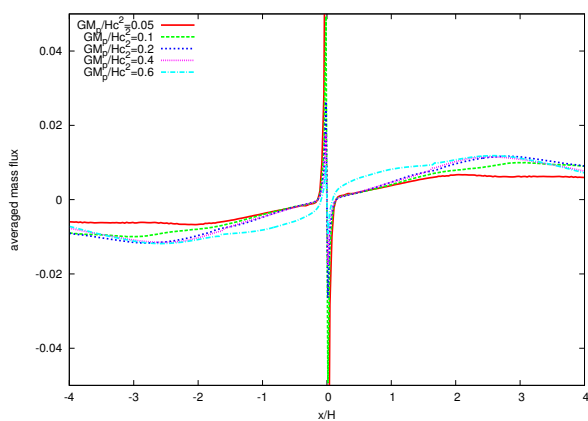
Figure 6.5: Azimuthally averaged mass flux at $t\Omega_\mathrm{p} = 100$ normalized by $(GM_\mathrm{p}/Hc^2)^2$.
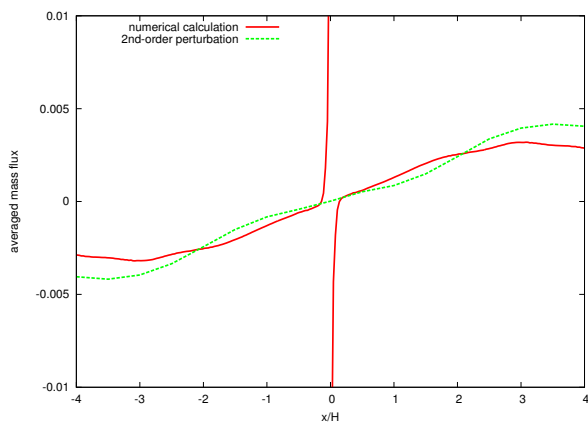

Figure 6.6: Comparison of the mass flux obtained by numerical calculation and second-order perturbation theory for $GM_\mathrm{p}/Hc^2 = 0.1$.

6.5   Gap Opening Timescale and Criterion

We have seen that low-mass planets can potentially open a gap in an inviscid disk, it is interesting to investigate the minimum mass of the planet that can open up the gap. Low-mass planets are prone to type I migration and therefore, if the planet migrates before it opens up a gap, gap formation is impossible. Since the width of the gap is the order of scale height H, we compare the timescale of the planet migration with length H and the gap formation timescale. The planet migration timescale in an isothermal disk is estimated by Tanaka et al. (2001) as

$$\tau_{\rm mig}^{-1} \sim 3\Omega_{\rm p} \frac{M_{\rm p}}{M_*} \frac{\Sigma r_{\rm p}^2}{M_*} \left(\frac{r_{\rm p}}{H}\right)^3. \tag{6.28}$$

Note that the power of $H/r_{\rm p}$ is 3 because we consider the migration over the radial length H. For gap formation timescale, we use the mass flux obtained from the simulation

$$\frac{1}{L_y} \int dy \Sigma v_x \sim 4 \times 10^{-2} \Sigma c \frac{x}{H} \left(\frac{GM_{\rm p}}{Hc^2}\right)^2 \tag{6.29}$$

within the range of $|x/H| \lesssim 3$. Therefore, the gap formation timescale may be estimated as

$$\tau_{\rm gap}^{-1} = \frac{\partial_x (1/L_y) \int dy \Sigma v_x}{(1/L_y) \int dy \Sigma} \sim 4 \times 10^2 \Omega_{\rm p} \left(\frac{r_{\rm p}}{H}\right)^6 \frac{M_{\rm p}}{M_*}. \tag{6.30}$$

Comparing $\tau_{\rm mig}$ and $\tau_{\rm gap}$, we obtain the gap formation condition

$$\frac{M_{\rm p}}{M_*} \gtrsim 3 \times 10^{-6} \left(\frac{H/r_{\rm p}}{0.05}\right)^3 \frac{\Sigma}{2 \times 10^3 {\rm gcm}^{-3}} \left(\frac{r_{\rm p}}{1{\rm AU}}\right)^2 \left(\frac{M_*}{M_\odot}\right)^{-1}. \tag{6.31}$$

We used typical values of Protoplanetary disk at 1AU to estimate the number. This condition derives that even Earth mass planet can form a gap in a protoplanetary disk at 1AU.

If the disk is in turbulent state, the effective viscosity can fill the gap. If we use standard α-prescription for turbulent viscosity $\nu = \alpha c H$, the timescale of viscous diffusion over length scale $\sim H$ is

$$\tau_{\rm vis}^{-1} \sim \alpha \Omega_{\rm p}. \tag{6.32}$$

If $\tau_{\rm vis}$ is shorter than $\tau_{\rm gap}$, we do not expect that the gap forms. This leads to another condition,

$$\alpha \lesssim 2.5 \times 10^{-6} \left(\frac{H/r_{\rm p}}{0.05}\right)^{-6} \left(\frac{M_{\rm p}/M_*}{10^{-6}}\right)^2. \tag{6.33}$$
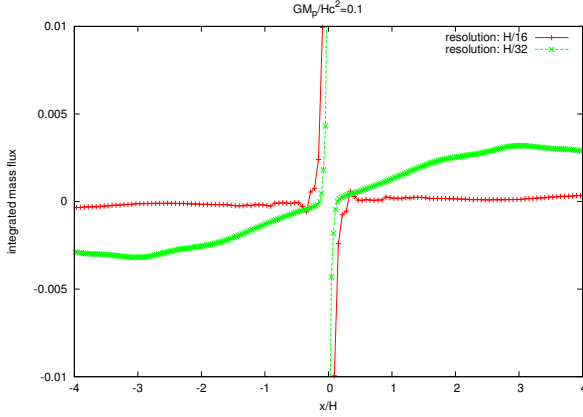
Figure 6.7: Mass flux obtained by the calculation with $GM_{\mathrm{p}}/Hc^2 = 0.1$ at $t\Omega_{\mathrm{p}} = 100$ for $\Delta x = \Delta y = H/16$ and $\Delta x = \Delta y = H/32$.

The disk must be very quiet in order for low-mass planets to open up the gap. We comment that this condition may not be simply extrapolated to higher mass case, since this is based on local calculations.

Equation (6.31) shows that gap can be opened even for low-mass planets. The gap opening criterion previously known for an inviscid disk is (Crida et al. 2006 [17])

$$\frac{r_{\mathrm{H}}}{H} \gtrsim \frac{3}{4}. \tag{6.34}$$

We note that the gap formation for low-mass planets can be observed only for high-resolution calculations. Figure 6.7 compares the mass flux obtained for calculations with $GM/Hc^2 = 0.1$ between resolution with $H/16$ and $H/32$. For calculations with low resolution, mass flux nearly vanishes. We have checked that for runs with GM_{p}/Hc^2 greater than 0.2, the result does not depend on the grid resolution. It is reasonable because length scales necessary to be resolved is smaller for smaller mass planets.

6.6 Gap Depth

We have seen that the gap may be opened around a low-mass planet. We now question when this gap opening ends. Li et al. (2005, 2008 [27] [53]) showed that there is a secondary instability after gap formation, which prevents the further opening of the gap. We have also seen that such an instability occurs for the high-mass run. Figure 6.8 shows the evolution of density profile and mass flux for the later stage of the run with $GM_{\mathrm{p}}/Hc^2 = 0.6$. The gap
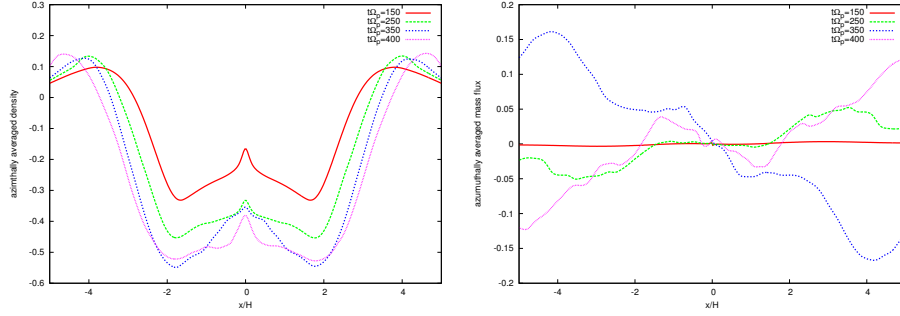
Figure 6.8: Left: Evolution of azimuthally averaged density perturbation for $GM_{\rm p}/Hc^2 = 0.6$. Right: Evolution of mass flux.

opening is saturated when approximately half of the mass is depleted due to the highly time-dependent mass flux.

The appearance of secondary instability may be understood by a simple linear analysis (see also de Val-Borro et al. 2007 [20]). We derive the condition for instability by performing stationary perturbation without a planet. Let us consider, for simplicity, a gapped disk without a planet. The equations we consider is therefore the equations (6.1) and (6.2) without $\psi_{\rm p}$. We assume that the background disk is axisymmetric with density profile $\rho_0(x)$. We denote the background values with subscript "0". In the background state, the pressure gradient must be balanced by Coriolis force and therefore,

$$v_{y,0}(x) = -\frac{3}{2}\Omega_{\rm p}x + \frac{c^2}{2\Omega_{\rm p}}\frac{1}{\rho_0}\frac{d\rho_0}{dx} \equiv U(x), \qquad (6.35)$$

and

$$v_{x,0} = 0. \qquad (6.36)$$

We now consider linear perturbation. Perturbed values are denoted by δ and consider the solution proportional to $\exp[-i\omega t + ik_y y]$ Linear perturbation is then

$$(-i\omega + U(x)ik_y)\frac{\delta\rho}{\rho_0} + \frac{d}{dx}\delta v_x + ik_y\delta v_y = 0, \qquad (6.37)$$

$$(-i\omega + U(x)ik_y)\delta v_x + c^2\frac{d}{dx}\frac{\delta\rho}{\rho_0} - 2\Omega_{\rm p}\delta v_y = 0, \qquad (6.38)$$

$$(-i\omega + U(x)ik_y)\delta v_y + c^2 ik_y\frac{\delta\rho}{\rho_0} + \left(2\Omega_{\rm p} + \frac{dU}{dx}\right)\delta v_x = 0. \qquad (6.39)$$

From these equations, we can derive a single second-order ordinary differential equation for δv_x,

$$\frac{d^2}{dx^2}\delta v_x + (4\Omega_{\rm p} + 2U')\,ik_y\frac{d}{dx}\delta v_x + ik_y\left(\frac{U''}{-i\omega U ik_y} + ik_y\right)\delta v_x = 0, \quad (6.40)$$

where $\prime$ denotes the derivative with x. If there exists a non-trivial solution for $\omega = 0$, the system is marginally stable. The boundary condition to be imposed is that the solution does not diverge at $|x| \to 0$. We also assume that the gap is weak and approximate $U \sim -(3/2)\Omega_{\mathrm{p}}x$ in the second term of equation (6.40). However, the term U'' cannot be neglected. For $\omega = 0$, using this approximation, we can further simplify the equation to the form of Schroedinger-type equation,

$$\frac{d^2g}{dx^2} + (-k_y^2 - V(x))g(x) = 0, \tag{6.41}$$

where

$$g(x) = x^{-1/3}\delta v_x \tag{6.42}$$

and

$$V(x) = \frac{U''}{(3/2)\Omega_{\mathrm{p}}x} + \frac{4}{9x^2}. \tag{6.43}$$

From equation (6.41), the condition for marginal stability is that there exists a "bound state" with energy $-k_y^2$. Since $-k_y^2 < 0$, it is possible when there exists a point where $U'' < 0$, which corresponds to the pressure bump from equation (6.35). This instability criterion is analogous to the condition of Kelvin-Helmholtz instability with smooth velocity shear background (e.g., Chandrasekhar 1981 [14]).

Li et al. (2005) [27] shows that the secondary instability can cause the vortices with low-m. To understand the saturation, it may be necessary to perform global calculations. We also note that since the conservation of specific vorticity is restricted to two-dimensional calculations, three-dimensional effects can well affect the final state. High-resolution three-dimensional calculations are interesting future work.

The gap formation around low-mass planets and the appearance of secondary instability may provide some new insights in the planetary migration. If a clear gap opens up around a planet, the interaction between the planet and the disk becomes weak, and therefore, migration timescale becomes longer. If secondary instability prohibits the formation of gap but causes the disk to be in a turbulent state, the migration can become random. Both of these effects can cause migration timescale longer, and the planet may be formed without falling onto the central star.

Chapter 7

Summary

Disk-planet interaction and planetary migration are important because they can provide the new ingredients of planetary formation theory. Classical (or standard) core accretion scenario assumes in-situ formation, that is, planets are formed from dust particles that have been there, and they have not migrated. However, it seems very probable that the planets migrate, and planetary migration can greatly alter the picture of planet formation theory.

The serious problem of planetary migration is that we do not know whether migration occurs inward or outward, and the direction of migration can be very sensitive to the disk state. In this thesis, we have explored extensively how the characteristics of disk-planet interaction are affected by magnetic field, viscosity, and non-linear effects, compared with non-magnetized, inviscid, linear theory first analyzed by Goldreich and Tremaine [38]. We have used local shearing-sheet approximations in order to simplify the problem, and to reveal the essential physical mechanisms of the disk-planet interaction in various disk states.

The effects of magnetic field are explored in Chapter 4. We have shown that very strong poloidal magnetic field (typically, magnetic energy needs to be much larger than thermal energy) can reduce the timescale of planetary migration drastically. We have derived analytic formulae for one-sided torque that agrees very well with numerical simulations. However, it may be quite likely that poloidal magnetic field is not so much strong that affects the planetary migration. Toroidal magnetic field can also affect the planetary migration, and the direction of migration can be reversed compared to the non-magnetized disk. Toroidal magnetic field at the equipartition level can affect the planetary migration. Our calculations in Chapter 4 are restricted to stable configuration of magnetic field. The effects of magneto-rotational instability are also a very interesting topic regarding the planetary migration.

The effects of viscosity on disk-planet interaction are investigated in

Chapter 5. We use a time-dependent formulation of linear analysis, which can be very easily extended to include many other effects. We have explored a wide range of viscous parameter, and found that the viscosity can tilt the density structure in the vicinity of the planet, which increases the one-sided torque exerted on the planet. When viscosity is very strong, one-sided torque becomes smaller due to strong damping. We have provided a fitting formula for one-sided torque as a function of viscous parameter. Our results suggest that the properties of planetary migration can be different if turbulent viscosity is considered, and future high-resolution numerical calculations are necessary.

Finally in Chapter 6, we have explored in detail the non-linearity of the interaction between the low-mass planet and the isothermal, inviscid disk using both analytic and numerical calculations. We have shown that mass flux appears in the vicinity of the planet as a result of shock formation of density wave. We have shown that the low-mass planets are potentially possible to form a gap in the vicinity of them, which may reduce the migration rate of the planet or causes instability. The message of this chapter is that non-linearity is important even if we consider low-mass planets. We have also shown that high-resolution calculations are necessary to see the effects, providing that future three-dimensional calculations are essential to understand more quantitatively the secular evolution of the gas disk in the vicinity of the planet.

Bibliography

[1] Abramowitz and Stegun. *Handbook of Mathematical Functions*. Dover, 1965.

[2] Adachi, Hayashi, and Nakazawa. The gas drag effect on the elliptic motion of a solid body in the primordial solar nebula. *Prog Theo Phys*, 56:1756, 1976.

[3] Andrews and Williams. Circumstellar dust disks in taurus-auriga: The submillimeter perspective. *ApJ*, 631:1134, 2005.

[4] Artymowicz. On the wave excitation and a generalized torque formula for Lindblad resonances excited by external potential. *ApJ*, 419:155, 1993.

[5] Bailes, Lyne, and Shemer. A planet orbiting the neutron star PSR1829-10. *Nature*, 352:311, 1991.

[6] Balbus and Hawley. A powerful local shear instability in weakly magnetized disks. I. linear analysis. *ApJ*, 376:214, 1991.

[7] Balbus and Hawly. Instability, turbulence, and enhanced transport on accretion disks. *Rev Mod Phys*, 70:1, 1998.

[8] Balbus and Papaloizou. On the dynamical foundations of alpha disks. *ApJ*, 521:650, 1999.

[9] Baruteau. Toward predictive scenarios of planetary migration. Ph. D. Thesis, 2008.

[10] Baruteau and Masset. On the corotation torque in a radiatively inefficient disk. *ApJ*, 672:1054, 2008.

[11] Cameron. Physics of the primitive solar accretion disk. *The Moon and Planets*, 18:5, 1978.

[12] Cannizzo, Shafer, and Wheeler. On the outburst recurrence time for the accretion disk limit cycle mechanism in dwarf novae. *ApJ*, 333:227, 1988.

[13] Chandrasekhar. *Principles of Stellar Dynamics.* Dover, 1960.

[14] Chandrasekhar. *Hydrodynamic and Hydromagnetic Stability.* Dover, 1981.

[15] Chiang and Goldreich. Spectral energy distributions of T Tauri stars with passive circumstellar disks. *ApJ*, 490:368, 1997.

[16] Colella and Woodward. The piecewise parabolic method (PPM) for gas-dynamical simulation. *J. Comp. Phys.*, 54:174, 1984.

[17] Crida, Morbidelli, and Masset. On the width and shape of gaps in protoplanetary disks. *Icarus*, 181:587, 2006.

[18] D'Angelo, Henning, and Kley. Nested-grid calculations of disk-planet interaction. *A&A*, 385:647, 2002.

[19] D'Angelo, Kley, and Henning. Orbital migration and mass accretion of protoplanets in three-dimentional global computations with nested grids. *ApJ*, 586:540, 2003.

[20] de Val-Borro, Artymowicz, D'Angelo, and Peplinski. Vortex generation in protoplanetary disks with an embedded giant planet. *A&A*, 471:1043, 2007.

[21] Desch. Mass distribution and planet formation in the solar nebula. *ApJ*, 671:878, 2007.

[22] The extrasolar encyclopedia. http://exoplanet.eu/index.php.

[23] Epstein. On the resistance experienced by spheres in their motion through gases. *Phys Rev*, 23:710, 1924.

[24] Fujiwara et al. The asymmetric thermal emission of the protoplanetary disk surrounding HD 142527 seen by SUBARU/COMICS. *ApJ*, 644:L133, 2006.

[25] Fukagawa et al. Spiral structure in the circumplanetary disk around AB Aurigae. *ApJ*, 605:L53, 2004.

[26] Johansen et al. Rapid planetesimal formation in turbulent circumstellar disks. *Nature*, 448:1022, 2007.

[27] Li et al. Potential vorticity evolution of a protoplanetary disk with an embedded protoplanet. *ApJ*, 624:1003, 2005.

[28] Machida et al. Collapse and fragmentation of rotating magnetized clouds - II. binary formation and fragmentation of first cores. *MNRAS*, 362:382, 2005.

[29] Marois et al. Direct imaging of multiple planets orbiting the star HR 8799. *Science*, 322:1348, 2008.

[30] Marois et al. Optical images of an exosolar planet 25 light-years from earth. *Science*, 322:1345, 2008.

[31] Press et al. *Numerical Recipes in Fortran 90*. Cambbridge University Press, 1996.

[32] Thalmann et al. Discovery of the coldest imaged companion of a sun-like star. *ApJ*, 707:L123, 2009.

[33] Fromang, Terquem, and Balbus. The ionization fraction in α models of protoplanetary discs. *MNRAS*, 329:18, 2002.

[34] Fromang, Terquem, and Nelson. Numerical simulations of type i planetary migration in non-turbulent magnetized discs. *MNRAS*, 363:943, 2005.

[35] Gammie. Layered accretion in T Tauri disks. *ApJ*, 457:355, 1996.

[36] Glassgold, Najita, and Igea. X-ray ionization of protoplanetary disks. *ApJ*, 480:344, 1997.

[37] Goldreich and Lynden-Bell. Spiral arms as sheared gravitational instabilities. *MNRAS*, 130:125, 1965.

[38] Goldreich and Tremaine. The excitation of density waves at the Lindblad and corotation resonances by an external potential. *ApJ*, 233:857, 1979.

[39] Goodman and Rafikov. Planetary torques as the viscosity of protoplanetary disks. *ApJ*, 552:793, 2001.

[40] Greenberg, Hartmann, Chapman, and Wacker. Planetesimals to planets - numerical simulation of collisional evolution. *Icarus*, 35:1, 1978.

[41] Haisch, Lada, and Lada. Disk frequencies and lifetimes in young clusters. *ApJ*, 553:L153, 2001.

[42] Hartmann, Calvet, Gullbring, and D'Alessio. Accretion and the evolution of T Tauri disks. *ApJ*, 495:385, 1998.

[43] Hayashi. Structure of the solar nebula, growth and decay of magnetic fields and effects on magnetic and turbulent viscosities on the nebula. *Prog Theo Phys Supple*, 70:35, 1981.

[44] Hayashi, Nakazawa, and Nakagawa. Formation of the solar system. In Black and Matthews, editors, *Protostars and Planets II*, page 1100. The University of Arizona Press, 1985.

[45] Inutsuka and Sano. Self-sustained ionization and vanishing of dead zones in protoplanetary disks. *ApJ*, 628:L155, 2005.

[46] Klahr and Bodenheimer. Formation of gas giant planets by concurrent accretion of solids and gas inside an anticyclonic vortex. *ApJ*, 639:432, 2006.

[47] Kokubo and Ida. Oligarchic growth of protoplanets. *Icarus*, 131:171, 1998.

[48] Korycansky and Pollack. Numerical calculations of the linear response of a gaseous disk to a protoplanet. *Icarus*, 102:150, 1993.

[49] Kusaka, Nakano, and Hayashi. Growth of solid particles in the primordial solar nebula. *Prog Theo Phys*, 44:1580, 1970.

[50] Lada. Star formation - from ob associations to protostars. In Dordrecht, editor, *Star Forming Regions*, page 1. D. Reidel Publishing Co., 1987.

[51] Landau and Lifshitz. *Fluid Mechanics*. Oxford: Pergamon, 1959.

[52] Laughlin, Steinecker, and Adams. Type I planetary migration with mhd turbulence. *ApJ*, 608:489, 2004.

[53] Li, Lubow, and Lin. Type I planet migration in nearly laminar disks. *ApJ*, 690:L52, 2009.

[54] Lubow. On mass transport in nonviscouw, non-self-gravitating fluid disks. *ApJ*, 362:395, 1990.

[55] Lyra, Johansen, Klahr, and Piskunov. Standing on the sholders of giants: Trojan Earths and vortex trapping in low mass self-gravitating protoplanetary disks of gas and solids. *A&A*, 493:1125, 2009.

[56] Homepage of Frederic Masset. http://www.maths.qmul.ac.uk/~masset/index.html.

[57] Masset. On the co-orbital corotation torque in a viscous disk and its impact on planetary migration. *ApJ*, 558:453, 2001.

[58] Masset. The co-orbital corotation torque in a viscous disk: Numerical simulations. *A&A*, 387:605, 2002.

[59] Mayor and Queloz. A jupiter-mass companion to a solar-type star. *Nature*, 378:355, 1995.

[60] Meyer-Vernet and Sicardy. On the physics of resonant disk-satellite interaction. *Icarus*, 69:157, 1987.

[61] Miyoshi, Takeuchi, Tanaka, and Ida. Gravitational interaction between a protoplanet and a protoplanetary disk I. local three-dimensional calculations. *ApJ*, 516:451, 1999.

[62] Mizuno, Nakazawa, and Hayashi. Instability of a gaseous envelope surrounding a planetary core and formation of a giant planets. *Prog Theo Phys*, 60:699, 1978.

[63] Muto and Inutsuka. Orbital evolution of a particle interacting with a single planet in a protoplanetary disk. *ApJ*, 695:1132, 2009.

[64] Narayan, Goldreich, and Goodman. Physics of modes in a differentially rotating system - Analysis of the shearing sheet. *MNRAS*, 228:1, 1987.

[65] Nelson and Papaloizou. The interaction of giant planets with a disc with MHD turbulence IV. Migration rates of embedded protoplanets. *MNRAS*, 350:849, 2004.

[66] Okuzumi. Electric charging of dust aggregates and its effect on dust coagulation in protoplanetary disks. *ApJ*, 698:1122, 2009.

[67] Paadekooper and Mellema. Halting type I planet migration in non-isothermal disks. *A&A*, 459:L17, 2006.

[68] Paardekooper, Baruteau, Crida, and Kley. A torque formula for non-isothermal type I planetary migration - I. unsaturated horseshoe drag. arXiv:0909.4552, MNRAS accepted, 2009.

[69] Paardekooper and Papaloizou. On corotation torques, horseshoe drag and the possibility of sustained stalled or outward protoplanetary migration. *MNRAS*, 394:2283, 2009.

[70] Paardekooper and Papaloizou. On the width and shape of the corotation region for low-mass planets. *MNRAS*, 394:2297, 2009.

[71] Papaloizou and Lin. On the tidal interaction between protoplanets and the primordial solar nebula. I - linear calculation of the role of angular momentum exchange. *ApJ*, 285:818, 1984.

[72] Pollack, McKay, and Christofferson. A calculation of thr rosseland mean opacity of dust grains in primordial solar system nabulae. *Icarus*, 64:471, 1985.

[73] Safronov. *Evolution of Protoplanetary Cloud and Formation of Earth and Planets.* Nauka, Moscow, 1969.

[74] Sano, Inutsuka, Turner, and Stone. Angular momontum transport by magnetohydrodynamic turbulence in accretion disks: Gas pressure dependence of the saturation lavel of the magnrtorotational instability. *ApJ*, 605:321, 2004.

[75] Sano and Miyama. Magnetorotational instability in protoplanetary disks. I. on the global stability of weakly ionized disks with ohmic dissipation. *ApJ*, 515:776, 1999.

[76] Sano, Miyama, Umebayashi, and Nakano. Magnetorotational instability in protoplanetary disks II. Ionization state and unstable regions. *ApJ*, 543:486, 2000.

[77] Schmidt, Salo, Spahn, and Petzschmann. Viscous overstability in saturn's b-ring. II. hydrodynamic theory and comparison to simulations. *Icarus*, 153:316, 2001.

[78] Sekiya. Quasi-equilibrium density distributions of small dust aggregations in the solar nebula. *Icarus*, 133:298, 1998.

[79] Shakura and Sunyaev. Black holes in binary systems. Observational appearance. *A&A*, 24:337, 1973.

[80] Stix. *Waves in Plasmas.* AIP, New York, 1992.

[81] Takeuchi and Miyama. Wave excitation in isothermal disks by external gravity. *PASJ*, 50:141, 1998.

[82] Takeuchi, Miyama, and Lin. Gap formation in protoplanetary disks. *ApJ*, 460:832, 1996.

[83] Tanaka, Takeuchi, and Ward. Three-dimensional interaction between a planet and isothermal gaseous disk I. corotation an lindblad torques and planet migration. *ApJ*, 565:1257, 2002.

[84] Tanaka and Ward. Three dimensional interaction between an planet and an isothermal gaseous disk II. Eccentricity waves and bending waves. *ApJ*, 602:388, 2004.

[85] Tanigawa and Watanabe. Gas accretion flows onto giant protoplanets: High-resolution two-dimensional simulations. *ApJ*, 580:506, 2002.

[86] Terquem. Stopping inward planetary migration by a toroidal magnetic field. *MNRAS*, 341:1157, 2003.

[87] Terquem. New composite models of partially ionized protoplanetary disks. *ApJ*, 689:532, 2008.

[88] Umebayashi. The densities of charged particles in very dense interstellar clouds. *Prog Theo Phys*, 69:480, 1983.

[89] Umebayashi and Nakano. Fluxes of energetic particles and the ionization rate in very dense interstellar clouds. *PASJ*, 33:617, 1981.

[90] Ward. Density waves in the solar nebula: Differential Lindblad torque. *Icarus*, 67:164, 1986.

[91] Ward. Protoplanet migration by nebula tides. *Icarus*, 126:261, 1997.

[92] Weidenschilling. Aerodynamics of solid bodies in the solar nebula. *MNRAS*, 180:57, 1977.

[93] Wetherhill and Stewart. Accumulationof a swarm of small planetecimals. *Icarus*, 77:330, 1989.

[94] Zhang and Lai. Wave excitation in three-dimensional discs by external gravity. *MNRAS*, 368:917, 2006.